Droplet Microfluidics: Tools for Screening and Sorting Applications

A dissertation presented
by

Donald Michael Aubrecht

to
The School of Engineering and Applied Sciences

in partial fulfillment of the requirements
for the degree of
Doctor of Philosophy
in the subject of
Applied Physics

Harvard University
Cambridge, Massachusetts

June 2013

Dissertation Advisor: David A. Weitz Donald Michael Aubrecht

Droplet Microfluidics: Tools for Screening and Sorting Applications

Abstract

Microfluidic droplets are a powerful tool for screening large populations of cells, molecules, and biochemical reactions. Droplet systems are able to encapsulate, incubate, screen, and sort millions of samples, providing access to large number statistics that make searching for rare events feasible. Initial development of the microfluidic devices and methods has attracted applications in biology, biochemistry, and material science, but the set of tools remains incomplete. Efforts are required to develop micro-scale droplet analogs for all bulk-scale bench top procedures and instruments. The droplet analogs must be versatile, robust, and process samples rapidly.

In this thesis, I discuss new microfluidic tools for screening analysis using aqueous droplets. I have reconfigured, optimized, and improved the instrument used for droplet generation and screening. I also develop and characterize microfluidic channels that coalesce pairs of droplets and sort droplets with increased efficiency. I delve into the chemical and physical phenomena are exploited and tailored to optimize device operation.

Contents

List of Figures

Acknowledgments

I am enormously grateful for everyone that has contributed to my PhD and time in SEAS at Harvard.

First and foremost, I would like to thank my advisor, Dave Weitz. Without Dave and the wonderful community of researchers he has assembled, none of this work would have been possible. I hope his physical intuition, appreciation of clarity, and knack for asking great questions continue to shape my experience in science and engineering.

I also benefited greatly from interactions and discussions with Ian Morrison, Seth Fraden, Jacy Bird, and Howard Stone. Thank you for always reminding me of the quick calculations and parameter estimations that can be made to tease out relevant physics. These discussions helped point me toward new ideas and drew me out of circular arguments.

Thank you to Stan Cotreau for managing a remarkable instructional machine shop. Without your guidance, trust, and wisdom, many of the techniques and instruments I developed would never have been created.

To all Weitzlab members, past and present: thank you for sharing your time, knowledge, and humor. You have provided a strong and engaging community, and I cherish my membership in this group.

Finally, to my family, close friends, and the Mountaineers: I am indebted to you for your support, compassion, technical discussions, and persistent quiet encouragement. Thank you.

For DAA, DEA, & SAA

Chapter 1

Introduction

Microfluidics has evolved as a standalone branch of microelectromechanical systems (MEMS) technology. The interdisciplinary nature of science and engineering continues to push focus toward microfluidic systems. This has brought engineers, physicists, chemists, and biologists together to develop the microfluidic tools necessary to study interesting questions. As the size of the microfluidic toolbox grows, the number of tractable problems in biology and chemistry also grows. Though simple questions have begun to be studied, we still lack microfluidic tools to investigate large number statistics on cellular expression or to search for rare and interesting mutations. Microfluidic emulsions are suited particularly well for studies of such questions. The emulsion droplets act as independent picoliter-scale reaction volumes. This brings the containment volume down to the cellular level, minimizing reagents, incubation times, and cost, while maximizing throughput and sensitivity.

In this chapter, we overview microfluidics, emulsions, and the general devices and methods used to produce microfluidic droplets. We also detail applications of droplet-based systems and highlight the advantages of using these approaches to investigate biochemical questions.

1.1 Microfluidics

Microfluidics uses tubing, capillaries, and channels to control the flow of fluids at micron to millimeter length scales. Typical characteristic volumes range from picoliters to microliters. Fluids are driven through these volumes with a pressure gradient generated by a pressure regulator maintaining a pressure set point at inlets or exits, or a syringe pump setting a volumetric flow rate. Flow within the microfluidic device is almost always laminar, with $\mathrm{Re} < 10$.

A specific subclass of microfluidics focuses on multi-phase flow: bringing immiscible fluids together in a controlled manner to generate an emulsion. In the simplest case, there are two immiscible fluids: a dispersed phase that forms droplets in the continuous phase, as shown in Figure 1.1(A). This process is typically not spontaneous and requires the application of shear to break the dispersed phase into droplets. Shear inputs energy to the system, enabling the creation of new surface area between the two fluid phases.

The most rudimentary process for forming an emulsion relies on simply shaking a vial containing the two fluids. This is exactly what occurs when you shake a bottle of vinaigrette salad dressing. While successful at creating an emulsion, the process is uncontrolled. Droplets are created with a broad distribution of sizes and no control over the contents of a particular droplet, as shown in Figure 1.1(B).

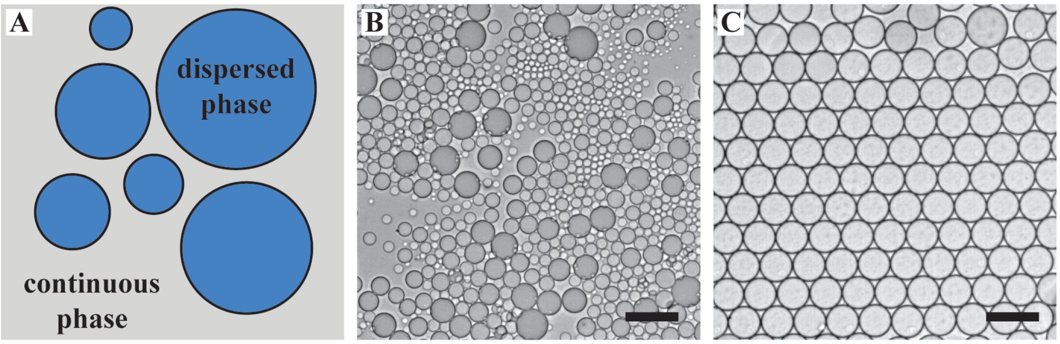

Figure 1.1: **(A)** Schematic showing the two phases of an emulsion. **(B)** Water-in-oil emulsion generated by vortexing two fluids in a vial. **(C)** Water-in-oil emulsion of the same fluids from (B), but generated in a microfluidic device. Scale bars represent 50 μm.

Microfluidic channels give us the tools to control droplet creation. By defining channels that bring the dispersed and continuous phases together in a controlled fashion and apply shear in a repeatable manner, droplet generation becomes defined by the surface chemistry of the constraining channels, the channel geometry, and the fluid flows [1, 2, 3, 4]. Simply producing the emulsion in a microfluidic device yields a monodisperse population of droplets, as seen in Figure 1.1(C). The design, operation, and application of such devices is detailed in the following sections.

1.2 Applications of Microfluidic Emulsions

The principles central to microfluidic droplet systems were first introduced using simple scaling analysis to show the impact of miniaturization on driving forces, physical parameters, and chemical parameters [5]. By shrinking the physical dimensions of containers for chemical analyses such as liquid chromatography or capillary electrophoresis, the analysis becomes faster, requires less reagents, and has the potential to be parallelized. The goal of performing all sample handling and preparation within close proximity of a small measurement sensor is referred to as a miniaturized total chemical analysis system, or μ-TAS.

Droplet microfluidic systems satisfy the definition of a μ-TAS and benefit from advantages in speed, volume, and parallelization over bulk techniques. We generate microfluidic droplets and ensure they remain separate and stable, so that each droplet is a unique reaction volume of 10-1000 picoliters. The droplets can store samples and carry out chemical and biological reactions.

Droplet microfluidic devices have seen rapid adoption in the fields of particle synthesis, biochemistry, and molecular biology. Questions in these fields benefit strongly from core attributes of microfabricated devices: small volume, high surface area/volume ratio, batch processing, and high throughput [6]. Microfluidic devices have enabled nanoparticle synthesis, on-chip PCR, molecular separations, measurements of single-cell dynamics, and cell screening [7, 6, 8, 9, 10].

1.2.1 Material Synthesis

Material synthesis in droplets benefits from precise control of droplet contents, spherical shape, monodispersity, and immiscibility of fluid phases. Droplet microfluidic devices have enabled controlled nanoparticle production [7], synthesis of irregular microparticles [9], generation of molecular imaging probes [11], and controlled fluorination of organic substrates [11]. Microfluidic devices constructed from glass capillaries are particularly well-suited for formation of polymer particles and lipid vesicles, as the capillaries are impervious to the required solvents [3, 12, 13]. Devices cast in polymers can be used for a range of limited solvents [14] or made impervious to most organics [15, 16], while offering the advantages of repeatable and scalable fabrication, easy parallelization [17], and extension to a wide range of length scales.

1.2.2 Biological Screening

Within the broad realm of molecular and cellular biology, droplet microfluidics is particularly well-suited for screening applications. Typical screens require preparation of hundreds of thousands or millions of samples to find a rare event. Performed with standard bench-top procedures using microwells, robots, and plate readers, a single screen can require months to acquire one round of data. This time frame is usually impossible to reach with live cells and sensitive biological molecules. By contrast, microfluidic droplet production and screening rates of kHz reduce the time frame to several hours [18]. This time frame is well within the timescales typical for keeping cells and biological molecules viable.

Recent work with droplet microfluidics has leveraged the ability to encapsulate single cells within the droplets. By diluting the cell solution or employing inertial focusing mechanisms, cells arrive at the droplet-forming nozzle well-spaced [19, 20, 21, 22, 23, 24, 25]. As droplets are formed, cells are simultaneously encapsulated with growth media and assay reagents. These cell-containing droplets are flowed through a stream of processing modules to add additional assay components [26, 27, 28], incubate the cells at elevated temperature [29, 30, 31], be stored in defined locations for long-term observation [32], or be sorted based upon assay results [33]. Such experiments have resulted in finding rare genetic mutations [33], expressed antibodies [34], and unique protein crystals [35].

1.3 Microfluidic Device Fabrication

Fabrication of microfluidic channels requires tools that create fluid pathways on the order of 10-100 μm. As with any manufacturing process, there are several options for production and the choice of an optimized process depends on the material being used. In the case of microfluidics, most solid materials can be used to form fluidic channels, but transparent materials yield a key advantage over opaque materials: the fluid flows can be imaged directly. Imaging the flows enables correlation of macro-scale bulk properties to micro-scale phenomena, and provides direct feedback on device operation. The best transparent material options are glass and silicones.

Glass is an obvious choice of material for working with a variety of fluids at small length scales. Glass capillaries are readily available in a range of sizes and cross sections, can be heated and pulled to very small dimensions, and are compatible with most fluids used for chemical syntheses and biological assays. By aligning a series of glass capillaries co-axially, a droplet producing nozzle is created where the capillaries meet [3, 12]. However, the manual alignment of capillaries means these devices are more works of art than scientific tools. No two devices will be exactly identical, as each is painstakingly crafted and aligned by hand. To overcome this drawback, we turn to the world of microelectronics.

The personal computer and integrated circuit have pushed advances in the development of tools for microscale fabrication. There exist a plethora of tools for creating 3D structures ranging from sub-micron to 100's of microns. Soft lithography takes advantage of these tools and repurposes them to fabricate relief structures for molding microfluidic channels in polydimethylsiloxane (PDMS) [36, 37, 38, 39]. The PDMS casts are exact replicas of the master and are thus reproducible scientific tools. PDMS cures translucent, is easily bonded to itself or glass to form closed channels, can have its surface chemistry modified in manners similar to glass, and is biocompatible [36, 38, 40, 41]. For these reasons, PDMS is ideally suited for use in microfluidic systems, particularly those used for biological experiments. See Section A.1 for details on soft lithography and device fabrication.

1.4 Microfluidic Droplet Formation

To use PDMS microfluidic channels for droplet experiments, we must generate micro-scale droplets robustly. This is accomplished by bringing two fluid phases together at a defined junction and shearing the dispersed phase into droplets. The junction must be carefully designed and have appropriate wetting properties.

Before discussing junction design, we address surface chemistry and wetting. When an emulsion is confined, the dispersed phase must remain as droplets and the continuous phase must surround the droplets. The continuous phase must preferentially wet the channel walls, and ideally, the dispersed phase should have a high energy interaction with the walls. Since we already have two immiscible fluids for the two phases, they are likely to have opposite wetting properties on a given surface. We must simply tailor the properties of the confining surfaces so that the continuous phase wets them.

Our choice of PDMS for the microfluidic device prevents us from using most hydrocarbon oils as one of the phases. Though hydrocarbons will readily wet the PDMS surfaces, they also swell the PDMS and affect device operation by changing channel dimensions. To avoid this, we use fluorocarbon oils, which are immiscible with hydrocarbons. Many of our experiments have a biological focus, which necessitates an aqueous-based dispersed phase. Water is immiscible with fluorocarbons, and so we will be able to use fluorocarbon oil continuous phases to form droplets of water in PDMS devices. To ensure proper wetting properties of the PDMS channels, we coat the microfluidic channels with Aquapel, a commercially-available fluorosilane glass treatment, making the channel walls fluorophillic. The contact angle of DI water on Aquapel-treated PDMS is 98.5°, while fluorocarbon oils readily wet the surface. This ensures the fluorocarbon oil will selectively wet the channel surfaces, leading to good break-off of aqueous droplets at the nozzle.

Two well-established channel geometries are used to combine fluids and create emulsion droplets: the T-junction and the flow focusing junction. In the T-junction geometry, the dispersed phase is flowed up the leg of the T toward the junction, while the continuous phase is flowed along the top arm of the T. At the junction, drops of dispersed phase are pinched off and flow downstream, as seen in Figure 1.2(A).

A flow focusing junction bring the fluids together at the intersection of two channels. The dispersed phase is flowed in the horizontal channel from the left, while the continuous phase enters the junction from above and below. Droplets are pinched off and flow downstream to the right, as seen in Figure 1.2(B)-(C). Droplet formation occurs at remarkably high production rates, often exceeding 1 kHz. We chose flow focusing junctions due to their greater control over encapsulation and droplet production.

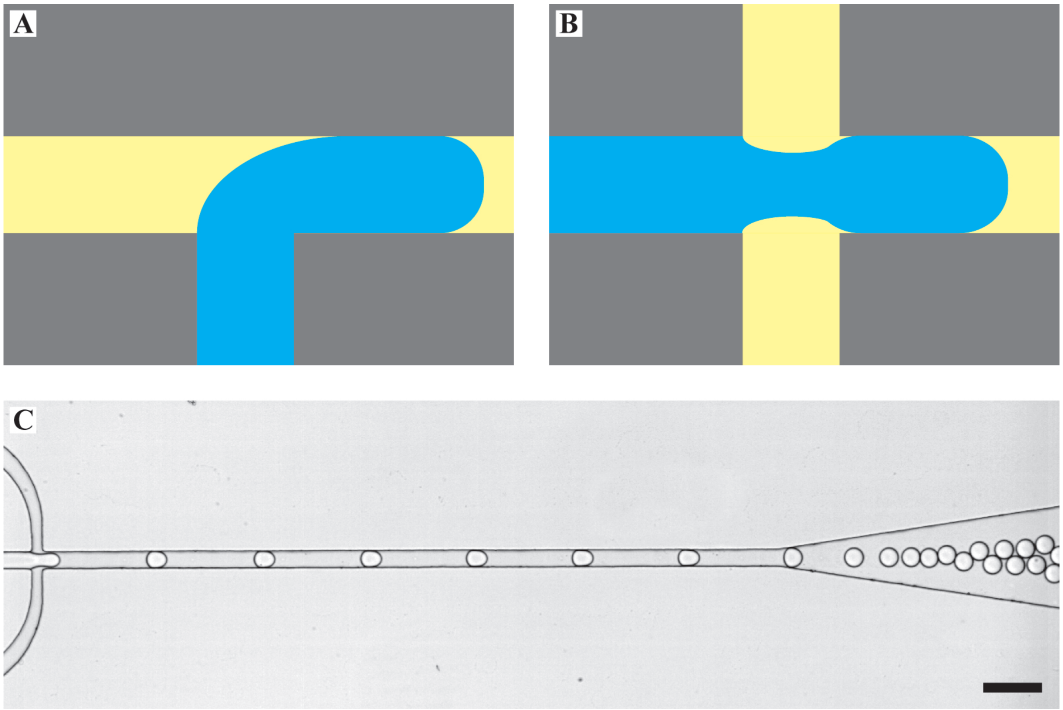

Figure 1.2: **(A)** Microfluidic droplet formation in a t-junction geometry. Oil (yellow) flows from left to right, breaking off pieces of the water stream (blue) as it flows up into the junction. **(B)** Microfluidic droplet formation in a flow focusing geometry. Oil (yellow) flows from top and bottom, pinching off water droplets (blue) from the thread flowing left to right. **(C)** Image of a flow focusing junction in operation. Scale bar represents 100 μm.

In PDMS microfluidic flow focusing devices, the mechanism of droplet formation is different from that of a freely-flowing column of water breaking up into droplets. Instead of a Rayleigh-Plateau instability generating deformations in the interface that grow and eventually pinch off [42], deformations are introduced by a controlled pressure oscillation. Syringe pumps supply fluids to the junction at constant volumetric flow rate. To begin the droplet formation process, the dispersed phase thread enters the junction orifice and restricts flow of the continuous phase. This in turn causes a momentary buildup of pressure in the continuous phase, causing the dispersed phase interface to deform. As this deformation grows, the interface detaches from the channel walls, the neck becomes unstable and eventually breaks, forming a droplet. The continuous phase flows freely, relieving the built-up pressure. The dispersed phase is now restricted and begins to build pressure. When this pressure become sufficient, the dispersed phase again enters the junction and begins the process of making the next droplet, as shown in the image sequence in Figure 1.3 [43, 44, 45, 46].

In this so-called "squeezing" regime of droplet formation where the capillary number, $Ca = \mu V/\gamma$, is less than 10^{-2}, a simple relationship exists for predicting droplet size. We expect the length of the droplet, L, to scale as

$$L = w\left(1 + \alpha \frac{Q_D}{Q_C}\right) \tag{1.1}$$

where w is the width of the exit channel from the junction, Q_D is the volumetric flow rate of the dispersed phase, Q_C is volumetric flow rate of the continuous phase, and α is a constant of order 1, whose value depends on the exact geometry of the channels [45]. In addition, the radius of the smallest droplet that can be formed by a junction is of the order, $R = (\frac{1}{4}whl)^{1/3}$, where h is the channel thickness and l is the length of the junction region.

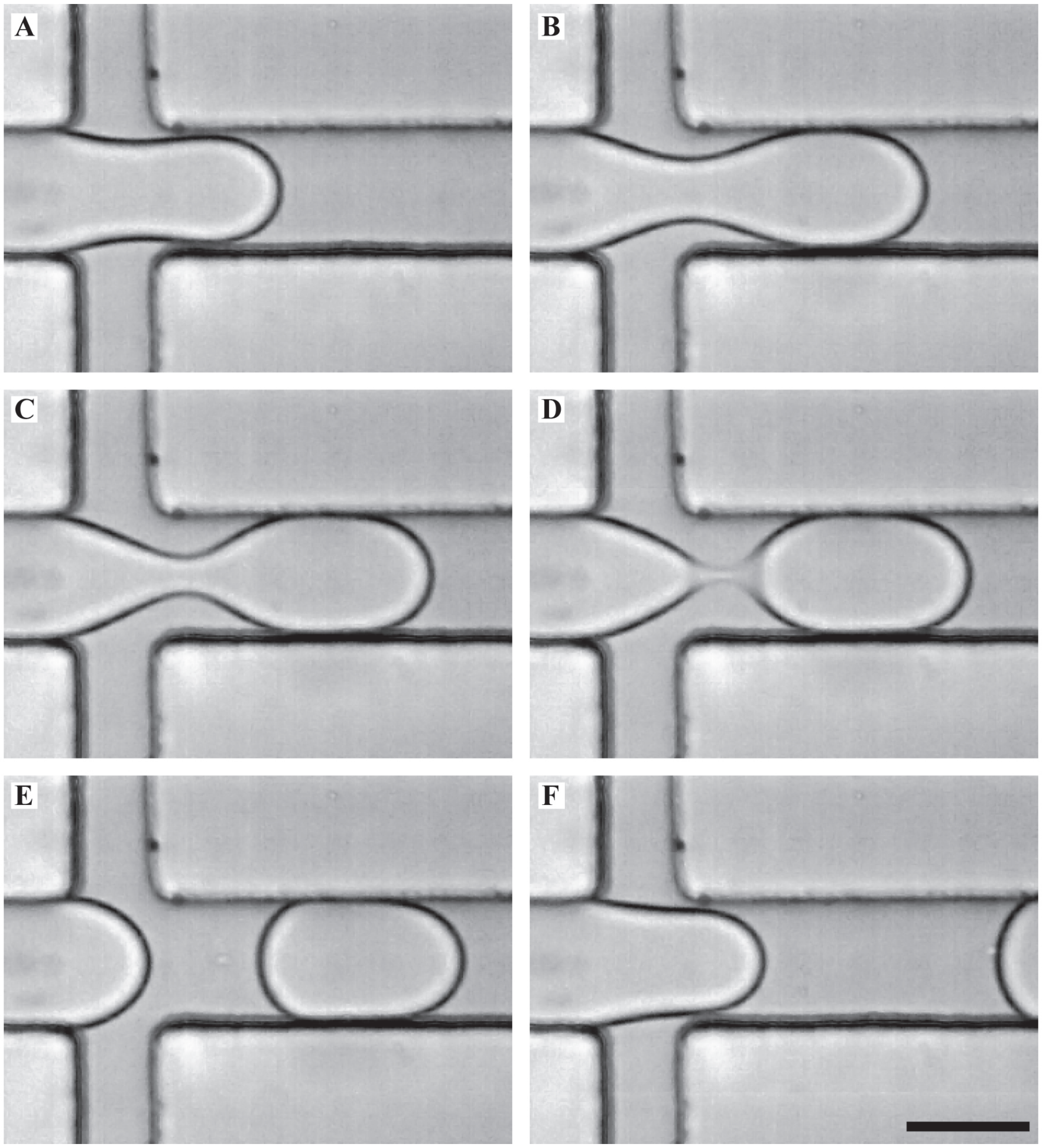

Figure 1.3: Formation of droplets at a microfluidic flow focusing junction. **(A)** Dispersed phase enters the junction and blocks the continuous phase. **(B)**-**(C)** The continuous phase builds pressure, causing deformation of the dispersed phase thread. **(D)** The thread becomes unstable and breaks, forming a droplet. **(E)** The thread retracts, allowing continuous phase to push the droplet downstream. **(F)** Pressure in the dispersed phase begins to build, starting the process again. Scale bar represents 30 μm.

1.5 Emulsion Stability

In general, emulsions are thermodynamically unstable dispersions [47, 48]. The interfacial tension between the fluid phases drives coalescence of droplets and eventual phase separation of the fluids. Phase separation minimizes surface area for a given volume, thus minimizing the total energy cost of interface between phases. To prevent this uncontrolled coalescence of the dispersed phase, surfactant molecules are added to one or all phases of the emulsion. The surfactants partition to the interface between phases, giving stability.

The presence of different chemical groups on a surfactant molecule disturbs the solvent liquid structure and increases the overall energy of the system. To combat this increase in energy, the solvent pushes the surfactant to concentrate at an interface or aggregate into micelles. Highly effective surfactants have a strong interaction with both phases at an interface. Loading of surfactant on the interface lowers the energy required to create or maintain interfacial area, as the dual chemical nature of the surfactant mediates the energetic cost of contact between the liquid phases. This results in a decrease in interfacial tension between the two phases [49].

Surfactant molecules stabilize emulsions by affecting one or more of the processes necessary for droplet coalescence. To coalesce with one another, dispersed phase droplets undergo a sequence of three processes: 1) the droplets are forced into contact with one another; 2) the film of continuous phase separating the droplets drains; and 3) thermal fluctuations of the interface between droplets nucleate a pore between the droplets, leading to coalescence [50]. Surfactants stabilize the interface sterically, minimize thermal fluctuations of the interface, and lower interfacial tension to decreases the energy cost associated with total interfacial area. With a good surfactant, only extreme stress will cause the emulsion to destabilize.

1.6 Advantages of Droplets and PDMS-based Microfluidic Devices

PDMS is an ideal material for exploratory experiments. It is biocompatible [40], reliably reproduces features to 10 nm [51], and can be processed rapidly [52]. Using standard soft lithography procedures [36, 38], an experimental microfluidic channel design can be taken from drawing to working device in approximately 36 hours.

PDMS devices containing aqueous droplets suspended in fluorocarbon oil provide suitable growth environments for cells and small organisms. Both PDMS and fluorocarbon oils have high gas permeability and the liquid interface allows for necessary gas exchange of CO_2 and O_2. PDMS and fluorocarbon oils are also free of toxic chemical species.

Aqueous droplet production in PDMS microfluidic devices is very fast, capable of generating greater than 1000 droplets per second. The picolitre-scale volume for each droplet means that large populations ($> 10^6$) can be generated from small total volumes (~ 1 mL). Precise control of droplet production results in monodisperse droplets with identical starting conditions in each droplet [10].

1.7 Challenges for Droplets and PDMS-based Microfluidic Devices

Though droplet microfluidics offers robustness, speed, and precision, there are concerns and challenges that must be addressed before leveraging these advantages. Unlike bulk-scale experiments performed in tubes or microwells, droplet-based experiments present challenges for handling and selection of individual reaction volumes. Whereas a person or robot can pick up and move a tube or microtiter plate, emulsion droplets cannot be handled directly. The size and liquid nature of the droplet microreactors make it exceptionally difficult to select and remove a single droplet from the bulk. Microfluidic devices can achieve this [53], but no bench top method exists to accomplish this. Thus, care must be taken when developing the order of operations on the droplet contents. Ideally, droplets are coalesced into a bulk aqueous phase after processing in microfluidic channels. Coalescing the droplets into a bulk sample allows the sample to be handled and processed with standard bench top instruments.

Maintaining the necessary microenvironment within droplets is also challenging. Many biological assays require elevated temperature for cell growth and expression of cellular products. An entire microfluidic device can be incubated at the necessary temperature, thus bringing the droplets to the correct temperature. However, due to the high gas permeability of the PDMS and relative volatility of the fluorocarbon phase, elevated temperatures risk destroying the droplet environment. Evaporation of the fluorocarbon oil leads to droplet coalescence, while evaporation of water increases the concentration of species within a droplet. These effects can be minimized by embedding low permeability layers in the PDMS [32] or creating a locally saturated environment when incubating droplets.

Liquid compatibility is an extremely important consideration when working with PDMS microfluidics. Many hydrocarbons partition into the PDMS, swelling it. This has two important impacts on microfluidic devices: first, as the PDMS swells, channel dimensions will decrease, altering droplet production and flow; and second, hydrocarbon phases and hydrophobic molecules will preferentially leave the emulsion for the PDMS. Without special treatment, this precludes the use of PDMS microfluidic devices for organic reactions or particle synthesis [15].

Finally, care must be taken when designing microfluidic channels. Fabricating channel molds with features thicker than 150 μm in SU-8 is time-consuming and imprecise. Casts of high aspect ratio channels are difficult to remove from the mold without damaging the PDMS. Silanization of the mold prior to casting helps release the cured PDMS, but does not completely eliminate the risk of tearing. PDMS casts of very low aspect ratio channels risk sagging and adhering the midpoint of their cantilevered span to the substrate. This is mitigated by including support columns within the channel and increasing the PDMS stiffness. There must also be sufficient space between adjacent fluidic channels to form a strong seal with the device substrate. With insufficient contact area between the PDMS and substrate, the high pressure gradients supported by microfluidic channels will cause delamination of the PDMS from the substrate, leading to device failure.

1.8 Outline of the Thesis

This thesis contains four Chapters which describe design, development, and use of droplet microfluidic systems. We focus on development of microfluidic modules as well as instruments for operation and support of the microfluidic devices.

Chapter 2 “Use of Microfluidic Systems” provides an introduction to microfluidic experiments with PDMS devices. We present an overview of the fluidic devices as well as the instrument used to control them.

Chapter 3 “Droplet Microfluidic Instruments” discusses improvements to the instrument systems. In particular, optimization of the excitation optics for fluorescence measurements and development of a temperature-controlled stage are detailed.

Chapter 4 “Manipulating Droplet Microreactors” focuses on new microfluidic channel designs that improve the preparation of droplet assay samples. We exploit unique chemical properties to selectively destabilize droplets and alter their contents.

Chapter 5 “Microfluidics as an Analytical Screening Tool” presents an optimized microfluidic channel design for screening and sorting microfluidic droplets. Droplet sorting tests and finite element simulations are used to evaluate electrode geometries for dielectrophoretic actuation of aqueous droplets.

Chapter 2

Use of Microfluidic Systems

As briefly mentioned in Section 1.2, microfluidic devices, particularly those fabricated in PDMS, offer several important advantages for performing experiments requiring large numbers of samples, precise control of reactions, and robust fluid flow. Compartmentalizing these samples into microfluidic droplets confers four distinct advantages over bulk methods. First, diffusive mixing times are decreased due to small distances and enhanced advection [54, 55, 56, 57, 58]. Second, small sample volumes decrease detection thresholds, as detectable concentrations are reached more quickly and with less total material [59]. Third, the choice of fluorocarbon oil as the continuous phases maximizes the likelihood of hydrophilic reaction products remaining within droplets. Finally, the droplet environment maintains a physical connection between the measurable product and its source, without relying on an aggregation or binding process that could change selectivity or reduce activity.

Producing droplets within microfluidic devices provides control over droplet size and composition. Tailoring the geometry of the fluidic channels and driving flow with precision syringe pumps or pressure regulators results in monodisperse production of droplets over a wide range of flow rates, viscosities, and sizes [1, 60, 61, 62, 63]. Control of channel geometry and fluid flow also provide control of droplet contents. Co-flowing laminar streams allow aqueous reagents to remain unmixed until the point of encapsulation in a droplet, as seen in Figure 2.1(A). The controlled pinch off of the aqueous stream into droplets enables encapsulation of cells, beads, and other particulate actives with 100% encapsulation efficiency, as seen in Figure 2.1(B)-(C). Droplets can be merged together or have additional fluid added [26, 27], as seen in Figure 2.2(A)-(F). These devices enable preparation of reactions and assays by introducing reagents into the droplet microenvironment at the proper time and concentration.

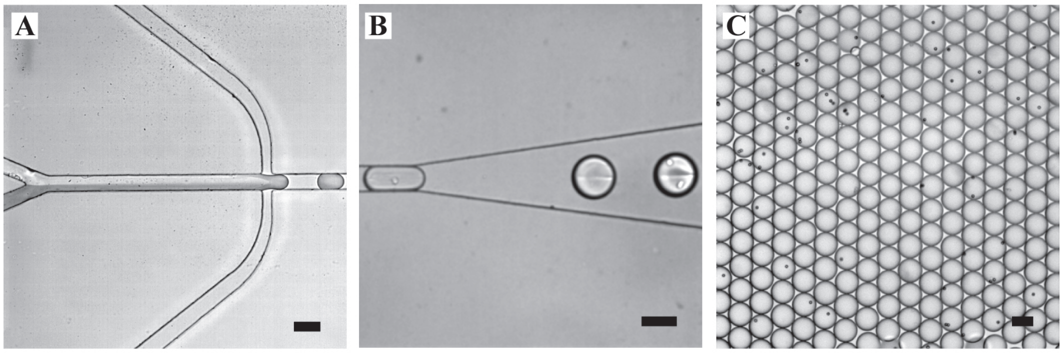

Figure 2.1: **(A)** Droplet formation from co-flowed aqueous streams. The dye in the lower stream diffuses very little into the upper stream prior to encapsulation. **(B)** Encapsulation of mammalian cells into droplets. (C) Encapsulation of 6 μm diameter polystyrene beads. The scale bars represent 50 μm.

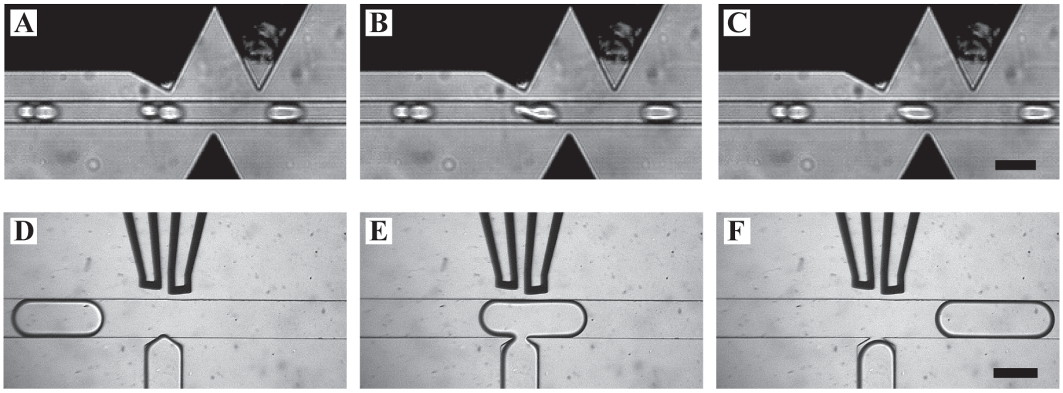

Figure 2.2: **(A)-(C)** Electrocoalescence of paired droplets. An electric field applied between the black electrodes above and below the channel causes the interface between droplets to destabilize, resulting in coalescence. The scale bar represents 100 μm. **(D)-(F)** Picoinjection of additional water into aqueous droplets. An electric field applied between the two black electrodes at the top of the image destabilize the interface between droplet and injection phase. The scale bar represents 500 μm.

2.1 Addressing Microfluidic Challenges

The challenges for use of droplets as microreaction volumes are briefly outlined in Section 1.7. These challenges fall into two broad categories: challenges related to device fabrication and operation, and challenges related to the biology and chemistry of the system being studied. Here we discuss solutions to issues in both categories.

2.1.1 Fabrication of Large Microfluidic Channels

Biological assays and reactions often require time to bind or react. Cells may require a certain volume of media and concentration of nutrients or waste. These requirements necessitate methods of fabricating large fluidic channels for either the timed storage of mass quantities of droplets ($> 10^5$ droplets) [64, 65, 28], building distribution channels to parallelize individual droplet makers [17, 66], or generating large volume droplets ($>$ 10 nL per droplet). As mentioned in Section 1.7, creation of large channels becomes difficult, if not impossible, with traditional photolithography.

Current routes to fabricate fluidic devices with channels that are more than 150 μm tall include direct machining in metals and plastics [67, 68, 69], fabrication of dies for hot embossing [70, 71], or 3D printing [72]. Direct machining and hot embossing produce well-defined features, but suffer from a limited choice of material for the final device as well as difficulty interfacing the device with fluid supply tubing. 3D printing equipment has become readily available, but printers lack the precision and material options provided by other techniques.

The limitations of direct machining and 3D printing are circumvented by fabricating plastic molds using a mechanical computer numeric control (CNC) mill. To highlight the strengths of this technique, we compare identical PDMS millifluidic devices cast in molds produced via three fabrication techniques: photolithographically patterning SU-8 photoresist, 3D printing (Objet Connex 500 printer), and CNC machining of Delrin. Delrin is chosen for its machinability, stiffness, and easy release of cast silicone parts.

We fabricate a mold of serpentine channels for on-chip storage of 25 μm diameter drops. The channel features are designed to have a cross section of 150 μm x 150 μm with an interchannel spacing of 500 μm, as shown in Figure 2.3(A). We also fabricate molds for drop makers that consist of square channels with three different cross sections: 150 μm x 150 μm, 250 μm x 250 μm, and 500 μm x 500 μm, as seen in Figure 2.3(B). The channel dimensions are larger than features conveniently produced via photolithography of SU-8, but smaller than the resolution limit of current 3D printers. Thus, when molds are fabricated in SU-8 or 3D printed materials, the resulting features suffer from long processing times, a lack of uniformity, and poor feature fidelity.

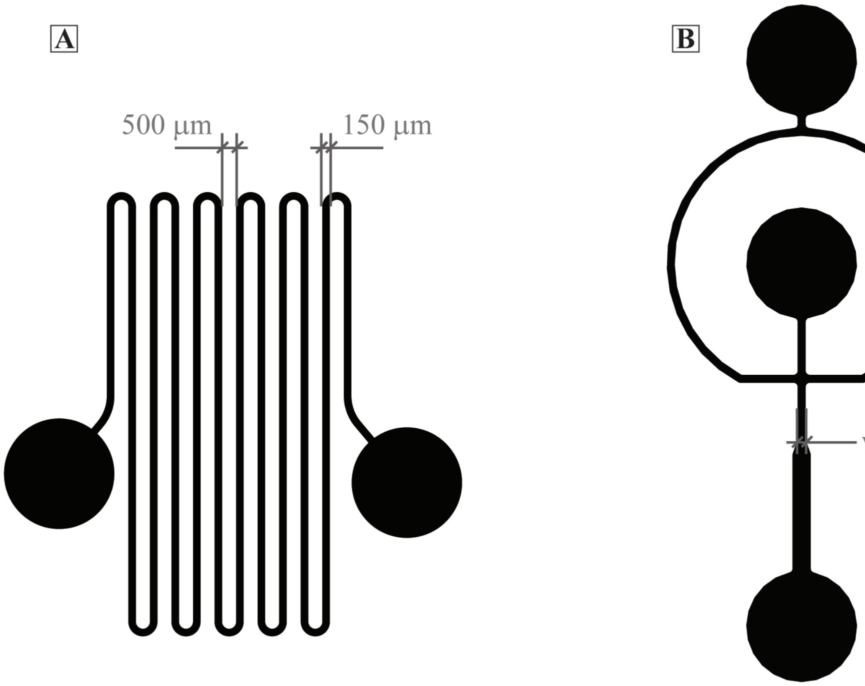

Figure 2.3: **(A)** Serpentine millifluidic channel design. The large circular areas are punch targets for fluid inlet and outlet. **(B)** Drop-forming millifluidic channel design. All four channels meeting at the central junction are of width and height, w. Three values of w were used for characterization: 150 μm, 250 μm, and 500 μm.

Using the machined mold fabrication technique, we can produce double-side patterned PDMS casts from a two-piece mold. The precision of the mill allows fabrication of tightly toleranced mold halves, such that features on each half are matched to one another without additional alignment steps, as seen in Figure 2.4. This device is unable to be produced via photolithography or 3D printing techniques.

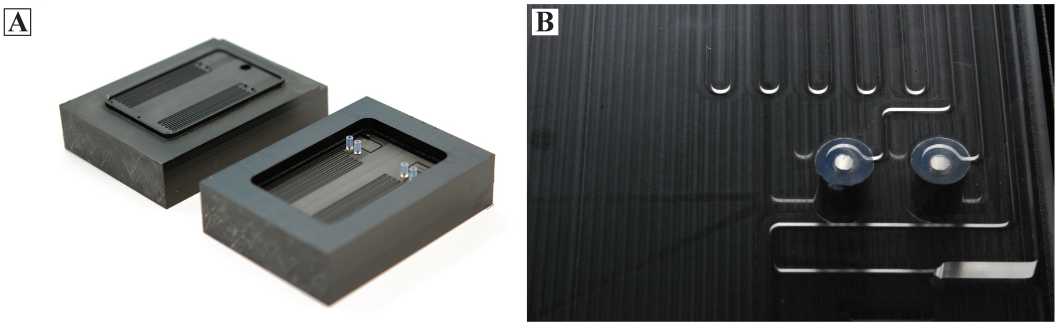

Figure 2.4: Images of double-sided machined molds. **(A)** Two mold halves with channel features milled into the surfaces. **(B)** Finished millifluidic device showing channels on the top and bottom surfaces of the cast PDMS. The channels are connected through the PDMS with FEP tubing cast in place.

The bonding strength between PDMS and the glass substrate depends on the surface roughness of the PDMS cast. Since PDMS casting reliably reproduces features below 10 nm [51], the surface roughness of the cast is largely determined by the roughness of the mold. Surface roughness of up to 9 μm allows sufficiently strong bonding for microfluidic operation, although lower roughness is preferred [72]. SU-8 molds have a roughness of 400 nm; this is significantly lower than the 5 μm roughness of machined and 3D printed molds, as seen in Figure 2.5. The rotating mill bit produces sharp, short wavelength features that are seen in Figure 2.5(A). The print head nozzles of the 3D printer produce the gentle waves seen in Figure 2.5(B). Though discernible in both the mold and cast PDMS part, 5 μm surface roughness affects neither bonding of devices nor flow in the fluidic channels.

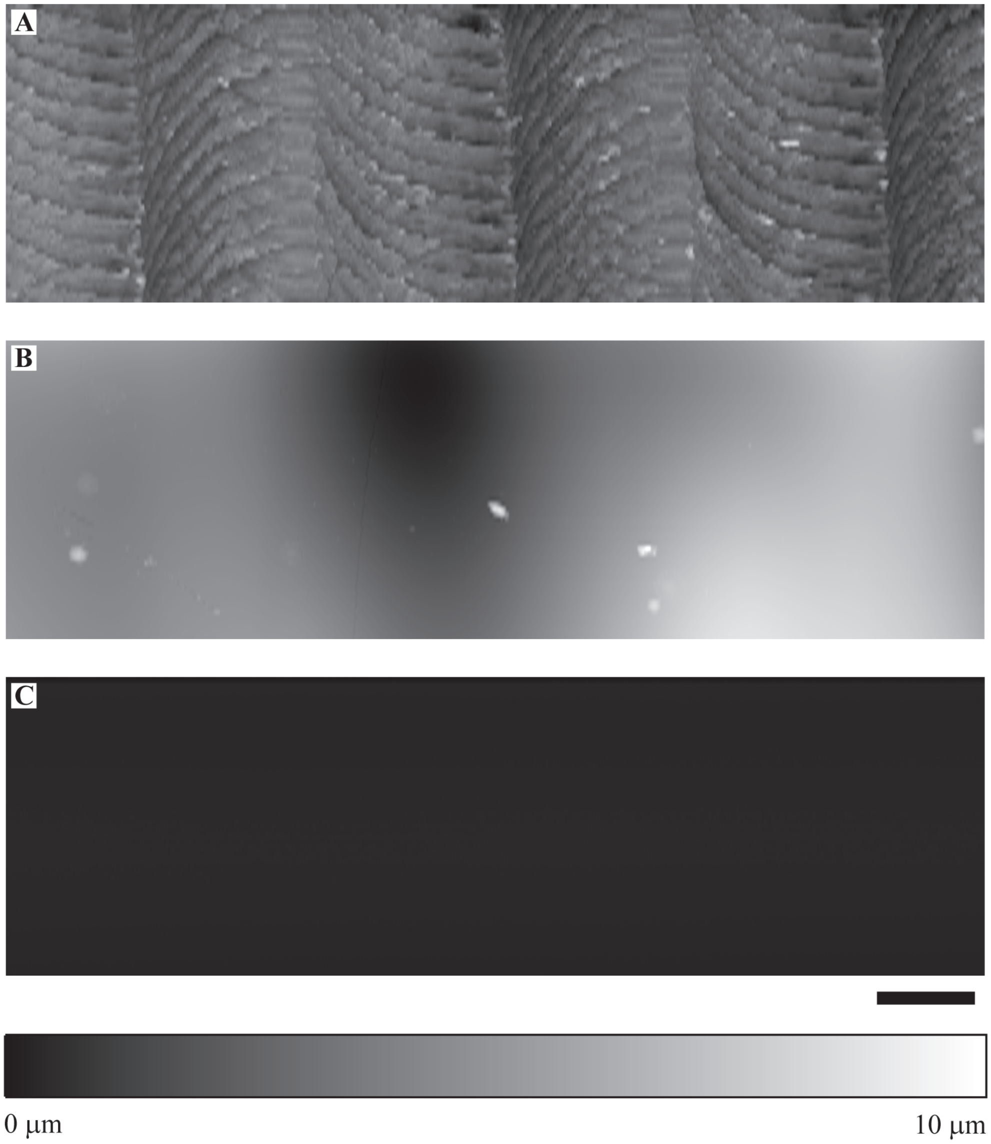

Figure 2.5: Surface topography by profilometer. Panels show the as-fabricated surface roughness for the three fabrication techniques: **(A)** milled Delrin plastic, **(B)** 3D printed Vero black plastic, and **(C)** SU-8 patterned via photolithography. Note: panel (C) is intentionally black to maintain identical scales for all three panels; the surface roughness of the spin-coated SU-8 is less than 1 μm and thus not visible at this scale. Scale bar represents 100 μm.

The spacing of roughness patterns on machined molds is controlled by the translation speed of the mill table, s, the rotation rate of the mill bit, r, and the number of flutes on the mill bit, n. The approximate spatial frequency, f, of these patterns is given by:

$$f = \frac{rn}{s}$$

Given a sufficiently small bit, the resulting roughness is similar in magnitude to that produced by 3D printing, but occurs at a much higher spatial frequency, as seen in Figures 2.5(A). To minimize roughness, we maximize the spatial frequency to maximize overlap between cuts of successive flutes; we chose a bit with four flutes, $n = 4$, and operating at a high rotation rate, $r = 2200$ rpm. Consequently, to fabricate a mold with a defined surface roughness, we minimize the fabrication time by increasing s and adjust r and n accordingly.

Although the magnitude of surface roughness for machined and 3D printed molds is similar, the molds differ greatly in channel cross section and feature fidelity, as seen in the scanning electron microscope (SEM) images of Figure 2.6. From the images, we observe that machined and SU-8 molds both show sharp corners at the top and bottom of the channel. These sharp corners and straight sidewalls indicate that the rectangular shape of the channels has been fabricated with good fidelity. 3D printed channel features are rounded and blurred, barely discernible at a magnification of 100x and indistinguishable from a flat surface at a magnification of 2000x.

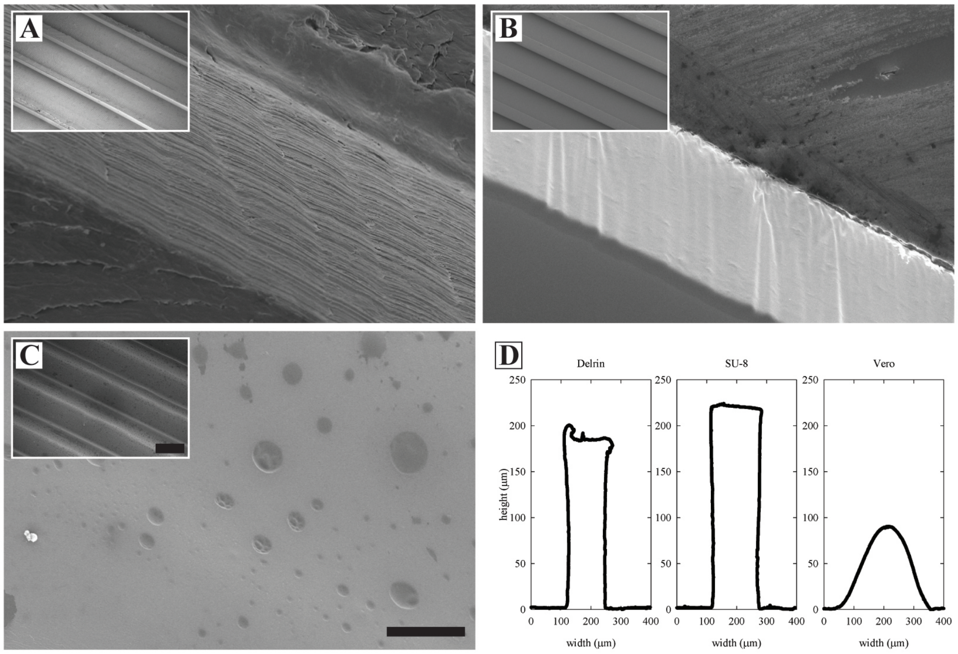

Figure 2.6: Edge sharpness and channel thickness characterized by SEM micrographs and channel sections. Primary micrographs show 2000x magnification images of the bottom, sidewall, and top surface of fluidic molds; inset images show 100x magnification images of the same channels. **(A)** milled Delrin plastic, **(B)** 3D printed Vero black plastic, **(C)** SU-8 patterned via photolithography. Scale bars represent 25 μm for primary images, and 500 μm for inset images. Panel **(D)** contains sections of PDMS channels for each mold fabrication technique.

None of the molds fabricated here completely conform to the original design of 150 μm square cross section channels, as seen in Figure 2.6(D). While the machined mold displays the correct channel width, it is 30 μm taller than the intended height of 150 μm. This error falls within the precision of +/-50 μm for the manual z-position on the mill. The features in the SU-8 mold are 75 μm taller than designed and the sidewalls are broadened by 10% at the top surface relative to their base width. The 3D printed mold displays the poorest fidelity of the features; channels resemble a rounded hill.

We test the impact of mold fabrication errors on the formation of monodisperse droplets of water in fluorocarbon oil using the drop making geometry in Figure 2.3(B). Droplets produced by channels cast from machined molds are consistently more monodisperse than those produced in channels cast from SU-8 or 3-D printed molds. We quantify the size distribution of drops by measuring their coefficient of variation (CV), defined as the standard deviation of the droplet diameter distribution divided by its mean, as shown in Table 2.1 and Figure 2.8. Droplets produced by devices with 250 μm tall channels cast from machined molds have a CV of less than 5% as noted in Table 2.1 and demonstrated by the fact that they crystallize in the image in Figure 2.7(A). By contrast, droplets produced by the channel cast from the 3-D printed mold display a larger diameter and CV, but still crystallize, indicating decent monodispersity. The droplets formed in devices cast from the SU-8 mold are not monodisperse enough to crystallize. A high monodispersity guarantees a more uniform initial condition for biological assays of cells encapsulated in droplets [10].

Table 2.1: Coefficient of variation calculated as standard deviation of droplet radius divided by the mean radius. Values in parentheses are FWHM divided by the mean. A CV for droplets produced in the 150 μm Vero device is unable to be calculated due to extreme polydispersity and misshapen droplets.

Characteristic Size	Delrin	Vero	SU-8
150 μm	0.6% (1.4%)	-	3.0% (7.1%)
250 μm	2.2% (5.1%)	2.8% (6.6%)	8.8% (20.8%)
500 μm	2.6% (6.0%)	5.4% (12.7%)	2.3% (5.5%)

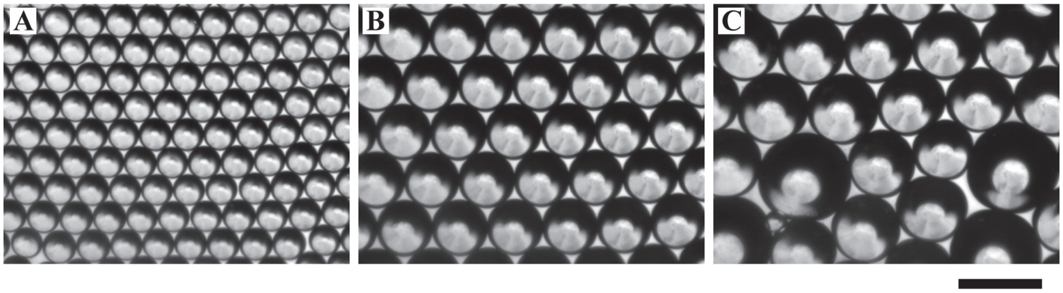

Figure 2.7: Droplets produced by 250 μm dropmakers: **(A)** milled Delrin, **(B)** printed Vero, and **(C)** SU-8. Scale bar represents 1 mm.

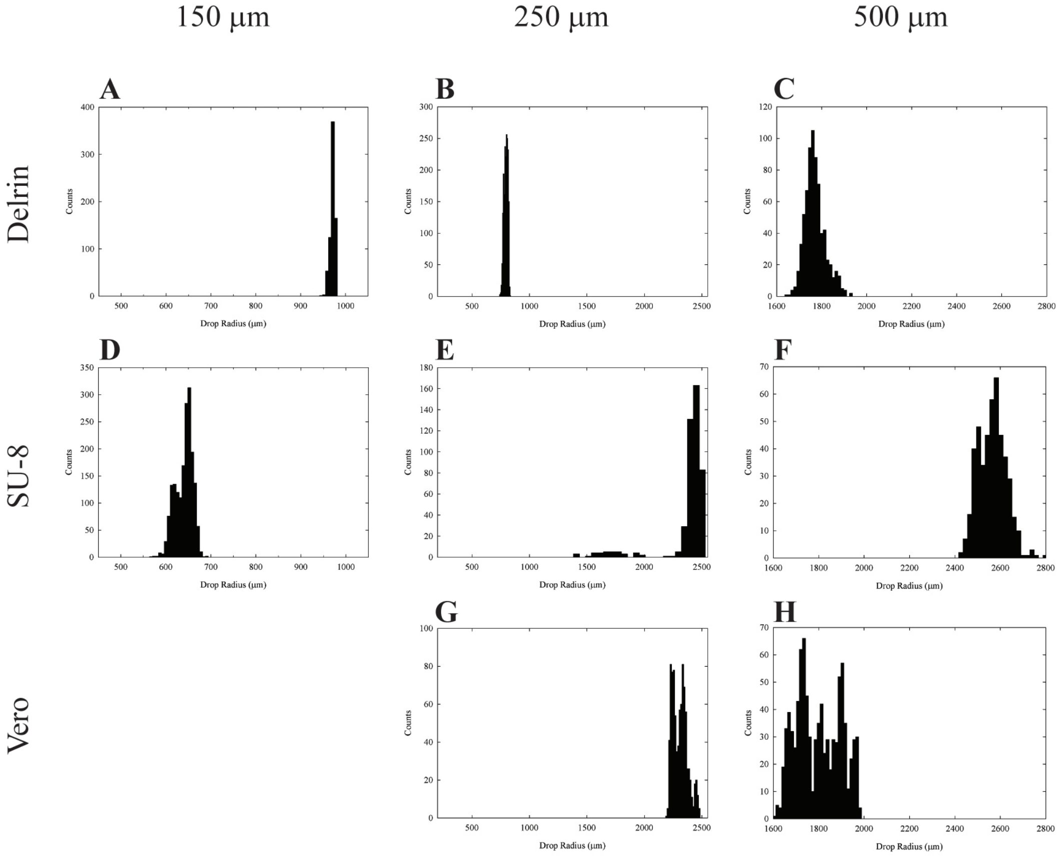

Figure 2.8: Histograms of radii for droplets produced in 150 μm, 250 μm, and 500 μm devices. Droplets produced in the 150 μm Vero device were too misshapen and polydisperse to measure accurate radii.

Mechanical milling produces the best molds for creating millifluidic devices and enables production of doubly-patterned devices through the use of two-part molds. The maximum roughness of machined molds is 5 μm, ensuring good bonding of the PDMS casts to glass substrates. Furthermore, milling ensures good fidelity of the features, and a rapid production of molds with features ranging from 150 μm to 2 mm. PDMS casts of these molds can be incorporated as complementary parts to microscale channels or used independently for millifluidic experiments. Channels cast from machined molds can be bonded and used with the operating procedures established for standard microfluidic devices. Machined Delrin molds produce millifluidic channels that display good control of fluid flow and enable stable production of droplets. This fabrication technique thus fills the current gap between microchannel and macroscale fluid handling, allowing us extension of precision fluid control to larger volumes.

2.1.2 Solvent Resistant PDMS

Section 1.4 details the basic physical mechanisms responsible for the formation of emulsion droplets in microfluidic channels. We optimize channel fabrication for working with aqueous droplets dispersed in fluorocarbon oils. However, occasions do arise where one of the emulsion phases must be a hydrocarbon and therefore will be miscible with the PDMS.

For instances where fluids miscible with PDMS must be used, such as particle synthesis [73, 74], we devise a method for limiting the effect of hydrocarbons on PDMS. Previous work has shown that lining the interior of the channels with a protective coating allows solvents such as toluene to be flowed through PDMS microfluidic channels. The most successful of these coatings are Parylene [29, 75] and a specially-formulated sol-gel [15, 16]. In both cases, the coating minimizes transport of small molecules to the PDMS and provides structural support for the channel. This minimizes changes in channel dimensions and prolongs device operation. However, in both cases, the coating is thick and uncontrolled, and thus channel designs must be adjusted to account for the coating.

Atomic layer deposition (ALD) is promising for addressing control of coating thickness, since the deposition process is self-limiting, depositing a single atomic layer at a time. This gives precise control of the surface composition and the thickness; the number of deposition cycles determines the finished coating thickness. One limitation to this process is the length of channel that can be coated. Since the ALD process relies on chemical vapor deposition, long channels and small cross sections impact the mean free path of the diffusing chemical species. For practical purposes, we determine a maximum channel length of 4 cm and minimum cross section of 10000 μm^2.

Sealed microfluidic channels are coated with nanometer-scale layers of Al_2O_3 using an S200 Savannah Atomic Layer Deposition system from Cambridge NanoTech. Temperatures are kept as low as possible to minimize the evolution of microscale structures and cracks on the surface of the PDMS. At high deposition temperatures or with thick coatings, the surface of the PDMS buckles into a series of interesting patterns. Similar patterns have been observed by other researchers performing chemical vapor deposition on PDMS at elevated temperature [76, 77, 41]. The elevated temperature during deposition creates residual stress at the interface between PDMS and the deposited film, leading to buckling of the surface.

We test the effectiveness of Al_2O_3 coating using solvent swelling and small molecule diffusion tests [15]. Coated and uncoated channels are filled with toluene, an organic solvent known to swell PDMS [14], as seen in Figure 2.9, and the change in channel dimensions are recorded, shown in Figure 2.10. The ALD coating limits contact of the toluene with the PDMS and provides structural support for the microchannel. Similar to the sol-gel coating, the Al_2O_3 coating does not fully eliminate swelling, but does extend the time over which a microchannel remains useful.

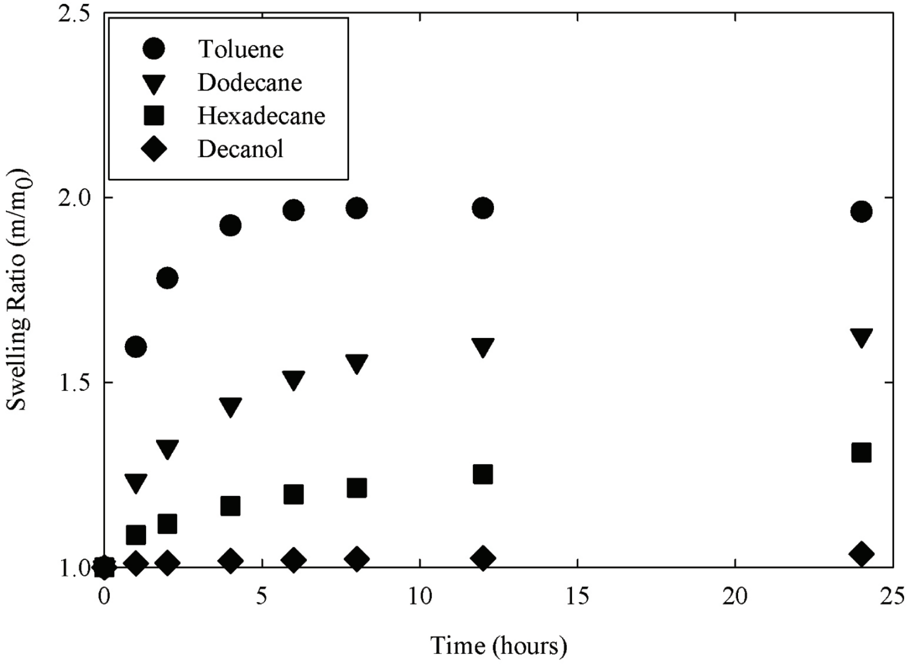

Figure 2.9: Swelling ratio of cross-linked PDMS in select organic liquids. Swelling ratio is calculated as m/m_0.

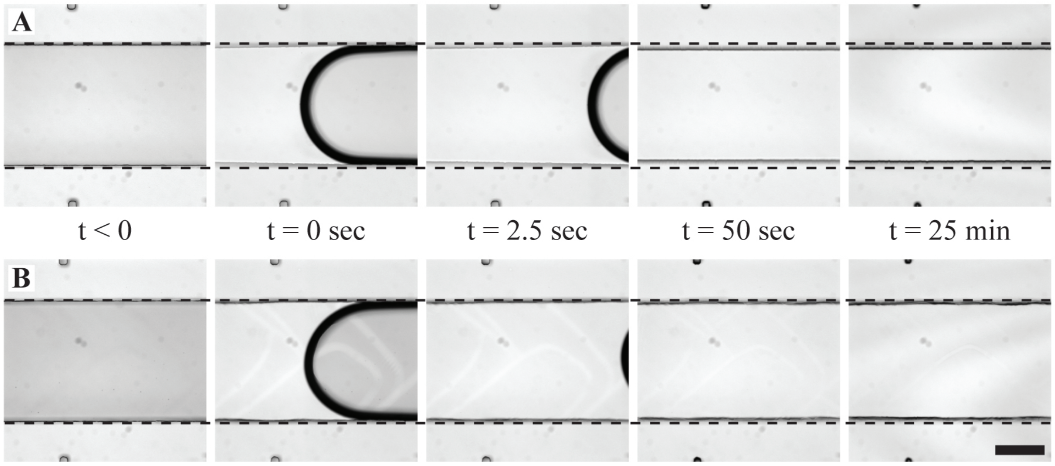

Figure 2.10: Minimization of toluene-induced swelling of PDMS microfluidic channels by Al_2O_3 coating. Dotted lines indicate channel sizes for $t < 0$. **(A)** Response of uncoated channel to toluene. **(B)** Response of Al_2O_3 coated channel to toluene. Scale bar represents 200 μm.

We also characterize the ability of the coating to limit transport of small molecules into the surrounding PDMS. This is especially important for biological assays involving small dyes and molecules, and for aqueous single phase experiments where solutes are in direct contact with the cross-linked PDMS network. In both cases, diffusion into and out of the PDMS leads to sample cross-contamination. To verify that the ALD coating successfully inhibits the diffusion of small species, coated and uncoated channels are filled with a concentrated solution of Rhodamine B in water and allowed to sit in a light-tight box for three days at room temperature. Comparing fluorescence images of coated and uncoated channels allows us to determine whether the Al_2O_3 coating inhibits diffusion. The uncoated channel displays bright rhodamine fluorescence in the channel walls, while there is no fluorescence visible in the walls of the coated channel, as seen in Figure 2.11. Thus, the Al_2O_3 coating prevents diffusion of the rhodamine into the PDMS.

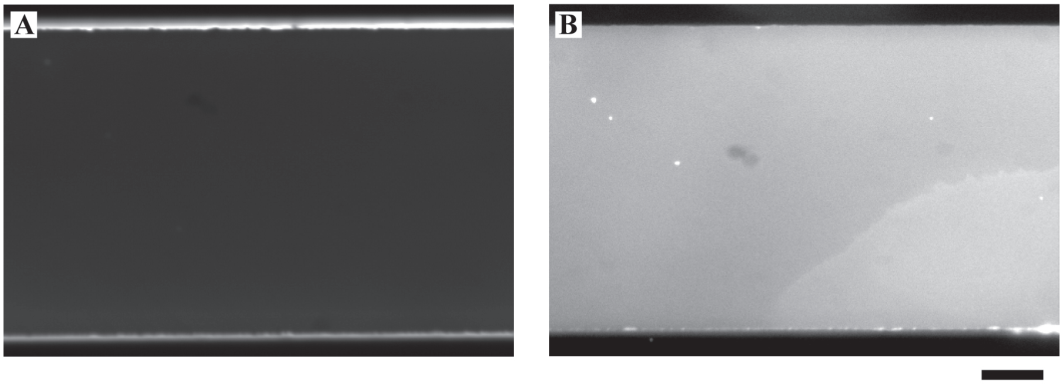

Figure 2.11: Minimization of rhodamine diffusion into PDMS by Al_2O_3 coating. **(A)** Fluorescence microscopy image of uncoated PDMS microfluidic channel. The bright sidewalls of the channel indicate that rhodamine diffuses into the PDMS. **(B)** Fluorescence microscopy image of Al_2O_3 coated PDMS microfluidic channel. The PDMS remains dark, while the channel volume is bright, indicating that rhodamine has dried on the channel surface but is unable to diffuse into the PDMS. Scale bar represents 100 μm.

With atomic layer deposition of Al_2O_3, we have demonstrated a robust protective coating for PDMS microfluidic channels that performs as well as other coatings, but is far easier to apply and has a smaller impact on the final channel features and geometry. As ALD is a CVD process, channel length and cross section must be carefully considered during the design of fluidic channels to ensure complete conformal coating for reasonable processing times.

2.1.3 Adaptation of Screening Assays

Droplet microfluidics has seen rapid adoption for screen experiments in biology. As mentioned in Section 1.2.2, the ability to produce and process droplets at rates of 100's to 1000's per second enables researchers to rapidly screen large libraries of cells and genes. Often, these searches screen through libraries of samples taken from the biosphere or produced in the laboratory by diversity generation methods like error-prone polymerase chain reaction (epPCR) and recombination [59].

While well-suited for screening large libraries for rare events, several concerns must be addressed before choosing droplet microfluidics over classical techniques. Due to their size, droplets contain a very small amount of assay product. Though concentrations may be high, total mass of product remains small and thus limits detection of the product to fluorescence methods. Consequently, an assay for a particular expression product may need to be developed or modified, since most current expression assays are spectrophotometric assays based on absorbance measurements. Commonly, a microfluidic droplet detection instrument will employ excitation lasers at 405nm, 488nm and 520nm. This prevents use of some published fluorescent assays, as their emissions overlap with excitation sources or their excitation wavelength is inaccessible with common laser wavelengths [78].

While the high concentration of product within a droplet can simplify detection, it also leads to complications. In substrate conversion assays, the high concentration of an active species, such as an enzyme, in the limited reaction volume will rapidly convert the limited amount of substrate and take the assay to its plateau value in a matter of seconds or minutes. Once the assay has plateaued, correlation between enzyme activity and fluorescence intensity is lost.

Surfactants used for stabilizing the emulsion droplets are of critical consideration when adapting assays for droplet systems. Surfactants capable of forming micelles should be avoided, if possible, since these micelles can transport fluorophores and expressed products, thereby enabling cross-talk between the droplets [79]. In addition, surfactants and reagents must be biochemically compatible with the cells or molecules being analyzed. Assays containing harmful chemical species risk lysing cells or denaturing genes and proteins; this results in loss of the genotype during characterization of the phenotype [78, 80].

In short, attention must be devoted to testing and characterizing assay performance in droplet systems. Microfluidic droplets are powerful screening tools, but the assay must produce independent, meaningful results.

2.2 Droplet Experiments

The casting, punching, and sealing of a PDMS microfluidic device is merely the initial step in conducting a droplet experiment. To make the device useful, several external systems are required to provide fluid flow, monitor the progress of droplet production, and measure droplet contents. A high level block diagram of these systems is shown in Figure 2.12. The three primary systems required for such experiments are fluidics, optics, and electronics [81]. Each will be detailed separately in the following sections.

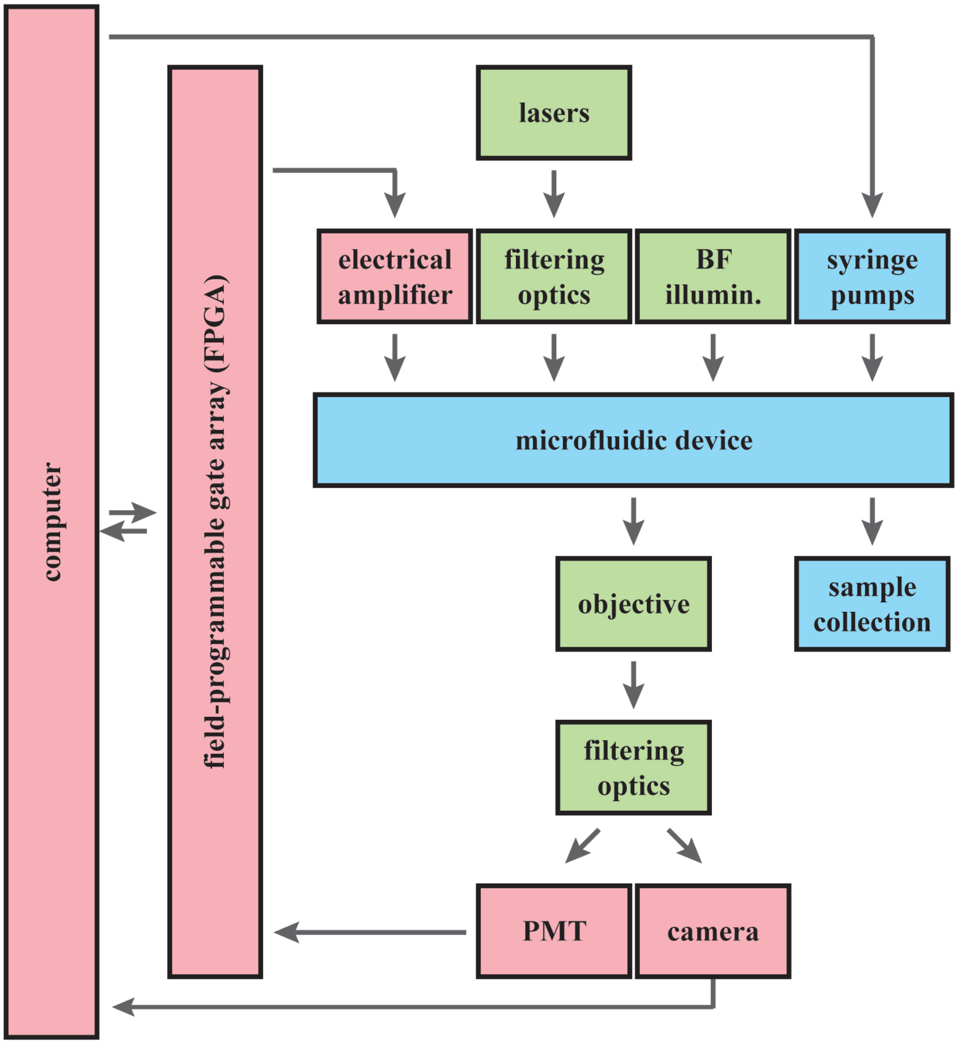

Figure 2.12: Schematic block diagram displaying the various components and systems required for integration in a fluorescence-based droplet sorting instrument. Colors denote the subsystem that a component belongs to: blue = fluidics, green = optics, and red = electronics.

2.2.1 Fluidics

The hardware requirements for fluidic controls are straightforward: sources of pressure to drive fluid flow, and microfluidic channels to produce and control droplets. Control of flow is achieved by either maintaining a particular pressure gradient (pressure controlled flow) or by maintaining a particular volumetric flow rate (volume controlled flow).

For low Reynolds number flows with a linear pressure gradient, the Navier-Stokes equation reduces to the following second order differential equation for the velocity, $v_x(y,z)$, through the cross section C:

$$\left[\partial_y^2 + \partial_z^2\right] v_x(y,z) = -\frac{\Delta p}{\eta L}, \text{ for } (y,z) \in C \tag{2.1}$$

The system is subject to a no-slip boundary condition at the walls, $\partial\Omega$:

$$v_x(y,z) = 0, \text{ for } (y,z) \in \partial\Omega \tag{2.2}$$

Analytical solutions to this ODE are possible for a limited number of cross sectional shapes, including a rectangular channel with cross section h x w, $h < w$, where $-\frac{1}{2}w < y < \frac{1}{2}w$ and $0 < z < h$. For a rectangular channel, the solution for the velocity profile is [82, 83]:

$$v_x(y,z) = \frac{4h^2\Delta p}{\pi^3\eta L}\sum_{n,\text{odd}}^{\infty}\frac{1}{n^3}\left[1 - \frac{\cosh\left(n\pi\frac{y}{h}\right)}{\cosh\left(n\pi\frac{w}{2h}\right)}\right]\sin\left(n\pi\frac{z}{h}\right) \tag{2.3}$$

Approximating the infinite sum and integrating the velocity, $v_x(y,z)$, over the channel cross section, we obtain the volumetric flow rate, Q:

$$Q \approx \left[1 - 0.630\frac{h}{w}\right]\frac{h^3 w}{12\eta L}\Delta p \tag{2.4}$$

This approximation is quite accurate for all rectangular geometries. For the worst case geometry, a square with $h = w$, the error in calculated flow rate is 13%. A channel with an aspect ratio of 0.5, such that $h = w/2$, has error in the calculated flow rate of only 0.2% [83].

Noting that in Equation 2.4, a constant pressure drop, Δp, results in a constant flow rate, Q, and drawing the parallel between electric current and fluid flow, and voltage and pressure, we arrive at the Hagen-Poiseuille relationship:

$$\Delta p = R_{hyd} Q \tag{2.5}$$

The proportionality constant, R_{hyd}, is the hydraulic resistance of the microfluidic channel network, akin to the electrical resistance of a circuit. Solving Equation 2.5 for R_{hyd} and substituting Q from Equation 2.4, we find an expression for the hydraulic resistance of a rectangular channel [83]:

$$R_{hyd} \approx \frac{12\eta L}{1 - 0.63(h/w)} \frac{1}{h^3 w} \tag{2.6}$$

R_{hyd} is a function of channel geometry, size, and the viscosity of the fluid. Since R_{hyd} is independent of the fluid driving force, by setting Δp, we determine Q for a given channel and fluid. Similarly, by setting Q, we determine Δp for a given channel and fluid. In practice, it is extremely difficult to determine R_{hyd} for an entire droplet microfluidic device, as branching channels and changing cross sections form complex resistance networks, and the presence of droplets creates additional resistance that is a function of the droplet volume fraction and the size ratio between the droplets and channels [84, 85].

Pressure controlled flow is easily achieved by maintaining a pressure set point over a reservoir of fluid using pressure regulators. Though extremely stable, this form of fluid control relies on the channel design to determine volumetric flow rate. Therefore, knowing a precise value for Q or the average velocity is quite rare for pressure controlled networks of droplet microfluidic channels. As many of our droplet operations rely on knowing droplet flow rate or average velocity, we rarely use pressure controlled flow in our systems, instead using volume controlled flow.

Volume controlled flow is easily implemented with a syringe pump. Pumps come in a variety of sizes, but most fall perfectly into the range useful for droplet microfluidics. By choosing volume controlled flow, we fix Q in Equation 2.5 and thus Δp is determined by the channel geometry. Assuming operation within the specified force range of the syringe pump, a volume controlled system offers precise control over flow rates and enables simple sample preparation using standard syringes. However, a volume controlled system suffers from long-lived pressure transients during startup and equilibration of the fluid flow.

Each particular droplet experiment relies on a unique channel design for droplet production. These designs display slight variations in performance. Droplet production in rectangular cross section microfluidic channels is well characterized by relationships that link droplet size, production frequency, and polydispersity to the channel geometry and fluid properties [1, 43, 44, 45, 61, 86, 87].

Once droplets are produced, there are often intermediate processing steps that must be accomplished before an assay is ready. These steps involve time delays to allow reactions to occur, incubation at elevated temperature, or the addition of other reagents to the droplets [28]. Delay or incubation steps require storage volume for a population of droplets; this can be achieved by collecting the droplets off-chip into a syringe or vial, or by flowing them into large volume serpentine channels, an example of which is shown in Figure 2.13. Serpentine channels and other on-chip storage techniques have the advantage of keeping the droplets in 100 μm - 1 mm scale channels that are easy to connect to other droplet processing channels. Keeping droplets on-chip minimizes risk to emulsion stability, but such channels are limited to smaller total storage volume than off-chip techniques.

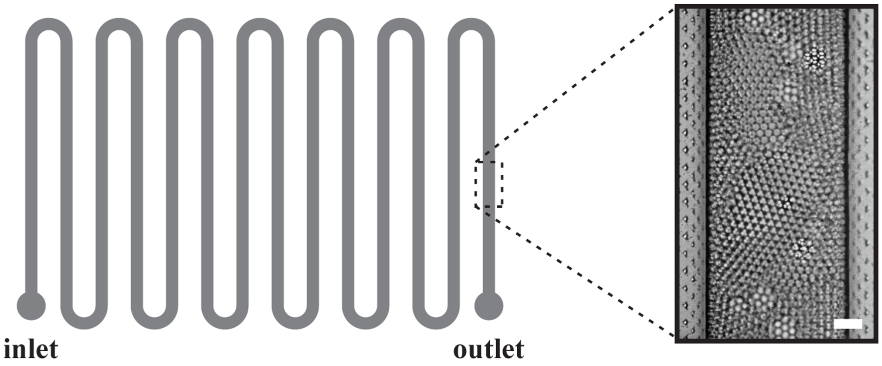

Figure 2.13: Schematic and image of aqueous droplets in a serpentine channel. These channels are used to incubate large quantities of droplets in a microfluidic device. The scale bar represents 100 μm.

Adding reagents to droplets is accomplished by coalescing additional aqueous phase with the existing droplet. Since the droplets are sterically stabilized by surfactant, coalescing droplets requires active destabilization of the oil-water interfaces. In microfluidic droplet devices, this is most commonly accomplished via electrocoalescence. Two device geometries have been developed: droplet merging, which coalescence a pairs of droplets as they flow between electrodes [26, 28, 88], and picoinjection, which coalesces passing droplets with a continuous aqueous phase [27]. These geometries are shown in Figure 2.2. We have also developed a new electrode-less method of coalescing droplets: this is described in Chapter 4.

Following the processing steps necessary to encapsulate and prepare the droplet contents, droplets are flowed into the microfluidic device for detection and sorting. This process is detailed in Chapter 5.

2.2.2 Optics

The optics form the heart of a microfluidic droplet detection and sorting instrument. There are a variety of choices available, so care must be taken to select components that are appropriate for a given experiment while maintaining flexibility. In the broadest scope, the optics consist of a bright field illumination source and high speed camera, a fluorescence excitation source, a fluorescence detector, an objective for collection of fluorescence and imaging, and an assortment of filters, dichroics, lenses, and mirrors. Choice and assembly of these components is detailed in this section.

The initial choice is between a microscope body or a completely custom optical setup. Use of a microscope simplifies choice and integration of the bright field and fluorescence components, but constrains the system to the microscope port geometries. A well-chosen microscope body provides a number of useful features, including: multiple access ports, Köhler illumination, translation stage, objective turret, filter cube carousel, and focusing optics for camera ports.

Alternatively, a similar system can be constructed on a custom fixture, eliminating all unnecessary components and simplifying the beam paths. The beam paths in a microscope are optimized for imaging, but often complicate the overall optics scheme. Switching to a custom fixture allows definition of optical path priority, and for many simple experiments, creates a more adaptable instrument. However, the features provided by the microscope body, including good illumination, a stage, and pre-alingment of components along the primary optical axis, must now be incorporated into the custom fixture.

The simplest schematic for the optics involved in our detection and sorting instrument is shown in Figure 2.14. The optics allow for simultaneous imaging in bright field and single color epifluorescence measurement using a focused laser spot. Recording the fluorescence excited by the laser yields two measures of the droplet contents: a spatial distribution of fluorescence with a droplet, since the flow maps spatial variation to temporal variation as the droplets pass the measurement point; and the total fluorescence, which is obtained by integrating the intensity over time.

White light bright field illumination is filtered by F1 (red) and illuminates droplets in the device. Simultaneously, the excitation laser (blue) is focused onto the microfluidic channel by the objective. The objective collects both the bright field image (red) and the emitted epifluorescence (green). Dichroic D1 transmits both the bright field and fluorescence, while reflecting the excitation laser. Dichroic D2 reflects the fluorescence through filter F2, which removes any fluorescence signal contamination before the detector measures intensity. Dichroic D2 transmits the bright field signal to lens L1, which images the droplets and channel on the camera sensor.

To add functionality and increase the sensitivity of the instrument, an optimized schematic is shown in Figure 2.15. This second system adds improved bright field illumination, creates a laser line instead of a laser spot, utilizes better dichroics, and adds the functionality of two color fluorescence detection. Most fluorescent assays require a system similar to that shown in Figure 2.15.

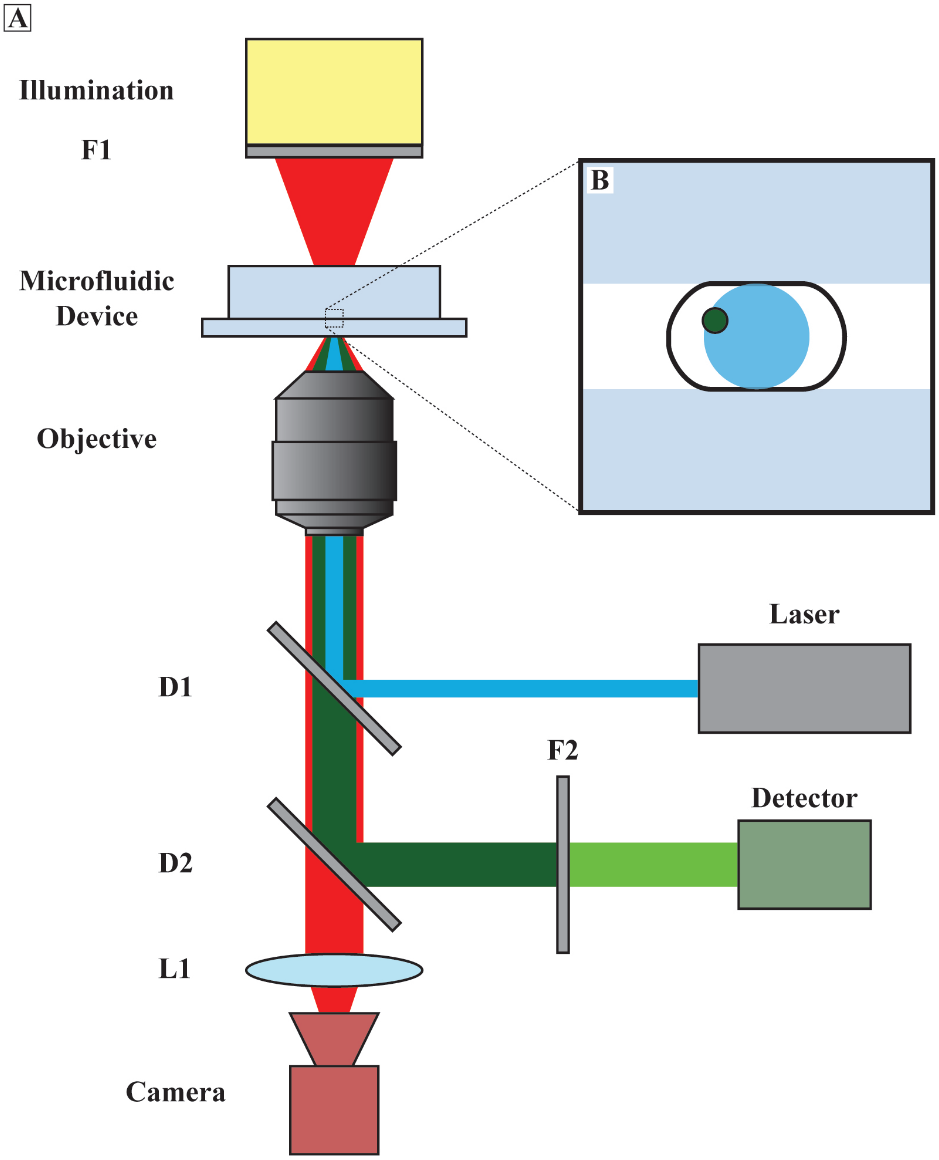

Figure 2.14: Schematic of the primary optical paths for fluorescence excitation and collection in the droplet sorting instrument. **(A)** Bright field illumination (red) is filtered by F1 and illuminates the microfluidic device. Simultaneously, the excitation laser (blue) is focused onto the sample by the objective. The objective collects both the bright field image and the emitted epifluorescence (green). **(B)** Schematic of laser spot illumination (blue circle) on a droplet (black outline) containing a fluorescent cell (green circle).

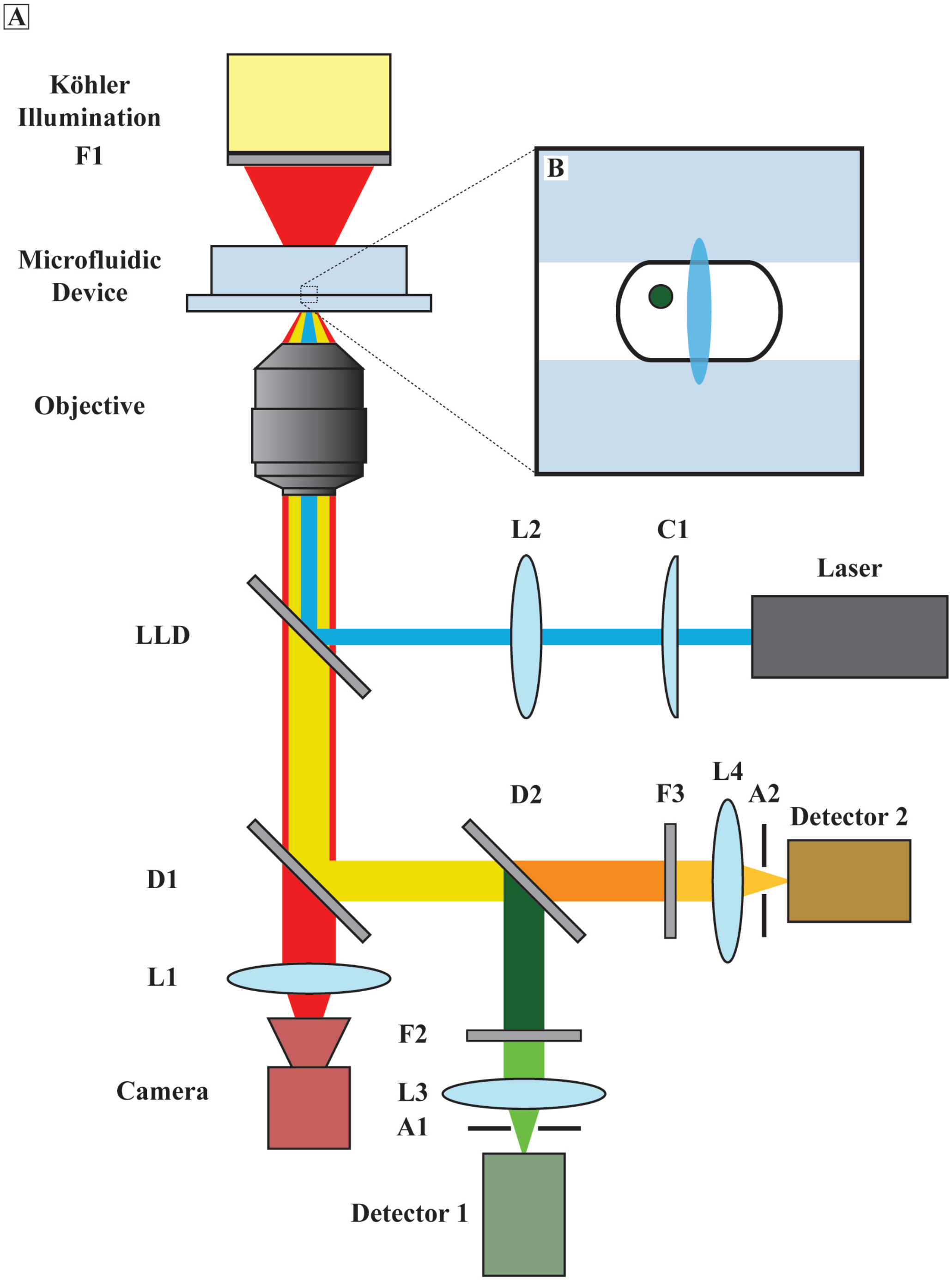

Figure 2.15: Schematic of optimized optical paths for droplet characterization. **(A)** Overview of full optics for bright field illumination and imaging, laser line excitation, and two color fluorescence detection. **(B)** Schematic of laser line illumination (blue oval) on a droplet (black outline) containing a fluorescent cell (green circle).

Functionally the same as Figure 2.14, the schematic shown in Figure 2.15 contains the following additions: Köhler bright field illumination, laser line dichroic (LLD), telescope with a cylindrical lens (C1, L2) to form a laser line with uniform illumination across the channel width, and two-color detection with focusing lenses and apertures (L3, A1, L4, A2). The laser line illuminates a smaller cross section of the droplet than the laser spot shown in Figure 2.14(B), thus achieving better detection of spatially separated objects within a droplet. The focusing lens associated with each fluorescence detector helps maximize signal by focusing all collected light onto the area of the sensor. The aperture minimizes noise in the fluorescence signal by eliminating light that originates from outside of the focal plane of the objective.

The schematics shown in Figures 2.14 and 2.15 are idealized illustrations free of physical constraints of space or other instrument components. These optical systems can be constructed as drawn using a custom fixture, but will likely need modification for use with a microscope body.

Once the primary fixture for the instrument is chosen, the optical components can be assembled. We will first discuss fluorescence illumination and filters. The choice of illumination and filter wavelengths depends on the assay being performed. Fluorophores display a distribution of intensity around their optimum wavelengths for excitation and emission. As such, choice of assay reagents determines the spectral features required of the fluorescence components. In practice, the droplet instrument is constructed with a versatile set of components that are adaptable for a range of different fluorophores and assays.

To illustrate choice of components, we consider a sample live/dead cell vitality assay and walk through determination of the components shown in Figure 2.15. The live/dead cell assay kit relies on two fluorophores: red fluorescent C_{12}-resorufin and green fluorescent SYTOX Green. The red C_{12}-resorufin is produced by reduction of C_{12}-resazurin in metabolically active cells, while the green SYTOX permeates damaged plasma membranes and stains nucleic acids. Thus, healthy cells exhibit red fluorescence, while dead or damaged cells exhibit green fluorescence [89]. The fluorescence spectra for C_{12}-resorufin and SYTOX Green are shown in Figure 2.16.

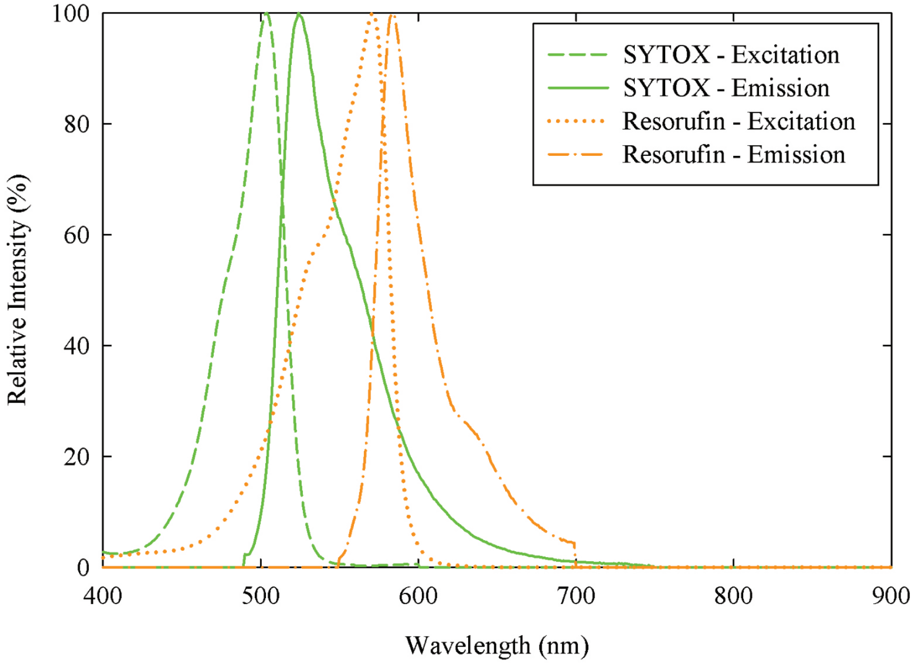

Figure 2.16: Excitation and emission spectra for the SYTOX and resorufin dyes used in a cellular live-dead assay.

From Figure 2.16, we see that though there is overlap between the emission spectra of the fluorophores, the emission peaks are distinct and lie in the middle of the visible spectrum. The excitation spectra overlap enough that we should be able to use a single excitation source, though one of the colors will suffer from decreased excitation. We chose a 488 nm laser for the excitation, as it will work for both fluorophores, is compatible with many other fluorophores, and lies outside of the emission spectra for C_{12}-resorufin and SYTOX Green, thus simplifying choice of other components. This choice requires that LLD in Figure 2.15 have a 488 nm reflection band. Since we are concerned with single source excitation, we choose a single-edge dichroic beamsplitter with a sharp edge at 495.5 nm (Semrock Di02-R488-25x36). If multicolor excitation is required, a multi-edge laser-flat dichoric beamsplitter with reflection bands that cover all the excitation wavelengths is installed at LLD.

Based on the fluorophore emission spectra, we see that the far red and near infrared lie outside of the emission spectra. The illumination for bright field imaging should be placed in this part of the spectrum to minimize overlap interference with the fluorophores. Many digital imaging sensors are sensitive in the infrared spectrum, but we must ensure that the bright field illumination stays within the camera's detectable range. Using the FastTec HiSpec 1 as a sample camera, we see that the sensor is responsive to 900 nm. We chose a 695 nm colored glass longpass filter (Thorlabs FGL695) for F1 on the light source and a corresponding 700 nm dichroic longpass for filter D1 (Semrock FF700-Di01-25x36).

Filter D2 is responsible for splitting the collected fluorescence emission to each of the color sensors. Thus, we need a filter that splits the spectrum between the emission peaks of the two fluorophores. We accomplish this by selecting a 538 nm longpass dichroic (FF538-FDi01-25x36). Choice of a bandpass with its edge below 540nm eliminates fluorescent cross-talk from the C_{12}-resorufin emission into the SYTOX Green detector.

We use a bandpass filter at each detector to minimize contamination of the fluorescence signal from each fluorophore. Ideally, these filters are narrow bands centered around the emission peak of each fluorophore. However, compromise must be made between what is ideal and what is commercially available. We select a 520/35 nm filter (Semrock FF01-

520/35-25) for F2 on the green channel and a 585/29 nm filter (Semrock FF01-585/29-25) for F3 on the orange channel. We plot the relevant spectral features for all portions of the chosen optics in Figure 2.17. Notice there is no overlap between excitation, emission, or imaging filters.

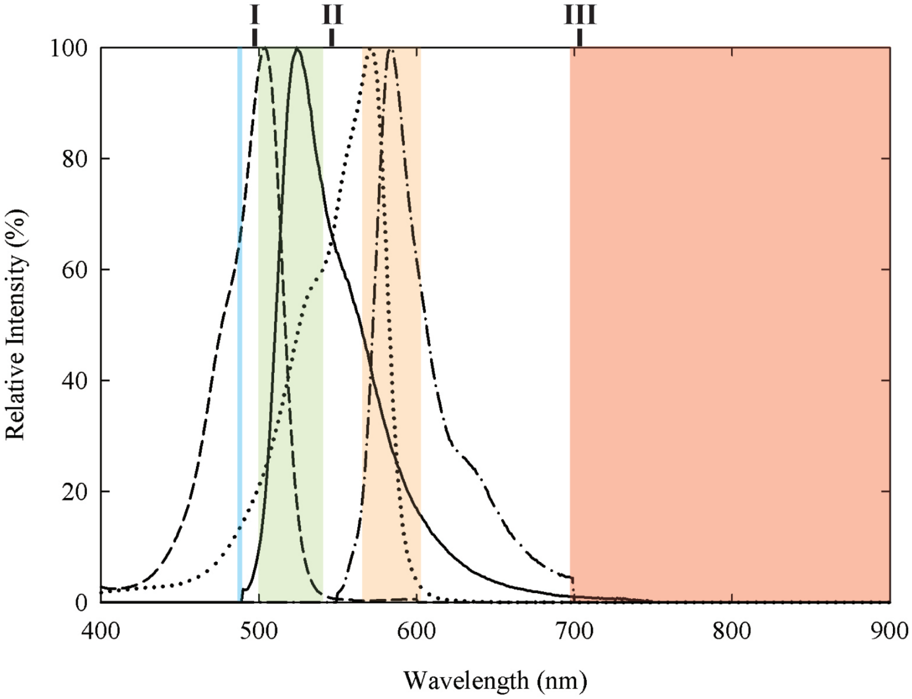

Figure 2.17: Excitation and emission spectra for SYTOX and resorufin, overlaid with filter pass bands and dichroic long pass edges for components outlined in the text. Blue indicates the laser excitation at 488 nm. Green indicates the 503-537 nm pass band of filter F2. Orange indicates the 570-600 nm pass band of filter F3. Red indicates the >695 nm pass band of filter F1. I indicates the edge of dichroic LLD at 495 nm. II indicates the edge of dichroic D2 at 538 nm. III indicates the edge of dichroic D1 at 700 nm.

While our selection of the fluorescence components is tailored for a particular assay, it is not difficult to modify the instrument to accommodate additional assays. Since 488 nm is a common excitation wavelength and many fluorophores emit wavelenths below 700 nm, we can leave F1, LLD, and D1 in place and simply adjust the other components for alternative fluorophores. Dichroic D2 is also rather versatile for many fluorophores, so by simply replacing filters F2 and F3, we accommodate different fluorophores in the green and yellow/orange/red spectra. This process is simplified through the use of filter wheels at positions F2 and F3, allowing multiple filters to be pre-mounted and simply rotated into place when needed.

After determining all of the filtering optics, the objective is the final component to be selected. Available objectives will be limited by the choice of instrument fixture and available adapters, since microscope manufacturers and optical component manufacturers have varying thread specifications. Basic suggestions for an objective include: a long working distance, since most microfluidic devices are bonded to microscope slides; a high numerical aperture (NA), to maximize the light collected at a given magnification; and an appropriate magnification, such that the laser is focused to a spot with a diameter roughly equivalent to the microfluidic channel width at the point where droplets will be analyzed.

2.2.3 Electronics

The basic electronic requirement is a computer devoted to the droplet instrument. Custom MATLAB and Labview interfaces are used to set, monitor, and control flow rates on syringe pumps, set points on pressure and vacuum reservoirs, and process droplet fluorescence intensities [81]. The computer also records digital video from the fast camera.

Syringe pump control is provided via serial port to RJ14 connectors. Harvard Apparatus, KD Scientific, and New Era OEM syringe pumps are selected for their compact size and appropriate range of flow rates and syringe sizes. All three brands lack user input controls on individual pumps, but support serial port communication and chaining pumps. Though each has proprietary control software, the textual commands can be sent via serial communication from MATLAB or Labview. These commands provide complete control of the syringe pump, allowing individual pump addressing; setting of syringe size, flow rate, and flow direction; and engaging/disengaging flow.

Most microfluidic processes occur on timescales of 10's of milliseconds: too fast to see in real time. To address this, experiments are recorded with a digital camera. The cameras vary from simple video frame rate cameras capturing at 30-60 fps to fast cameras recording images at >1000 fps. Most simple processes, such as droplet production, can be characterized using standard frame rates; the video will not capture the full time-resolved droplet formation, but individual frames can be used to verify droplet contents and proper droplet size. Fast cameras are used to image individual droplet formation or specific flow processes, such as coalescing of droplets.

For use on the instrument, the imaging sensor on a fast camera must have sensitivity in the infrared, otherwise it will require illumination that overlaps with fluorescence emission and will compromise the fluorescence signal. The camera must be capable of recording at least 5,000 fps at a resolution of 320 x 240 pixels. It is best if the camera is capable of very short exposures, ideally 10-100 μsec, as this minimizes blurring of moving droplets.

To achieve high-throughput screening of experiments in droplet microreactors, we must flow the droplets through the microfluidic detection channel rapidly. Ideally, we screen on the order of 1000 droplets per second. To obtain good sampling of fluorescence intensity within each drop, we need on the order of 100 data points per droplet. This necessitates data acquisition and processing rates of 100 kHz for two or more channels, assuming at least a two-color assay. Rapid acquisition and handling of these parallel datasets is best achieve using a field-programmable gate array (FPGA) interfaced to a Labview program. This allows rapid acquisition, processing, triggering, and storage to be performed by the FPGA, while data is fed to user displays at a decimated rate. Thus, data handling and storage is decoupled from user response time and input. Additional information about the specifics of the FPGA/Labview interface can be found in References [34] and [81].

The fluorescence detectors must be sensitive and capable of rapid acquisition. Photomultiplier tubes (PMTs) are an ideal choice, but could be substituted for avalanche photodiodes (APDs). The detectors must be easily mounted on a 1 inch lens tube. Since we sample fluorescence at 100kHz to ensure at least 100 samples per droplet, the detectors must have a frequency bandwidth greater than this; we chose PMTs with a bandwidth of 200kHz (Hamamatsu H9656). It is ideal for the PMT or other detector to have an on-board amplifier, such that the fluorescence intensity is output as a voltage signal. This allows the FPGA to directly measure the detector output.

In addition to the basic requirement of a computer for flow control and imaging, droplet experiments may incorporate a variety of other electronic instruments, including an oscilloscope, electrical waveform function generator, and high voltage amplifier. The function generators and amplifier are used to generate electrical pulses for electrocoalescence and dielectrophoretic droplet sorting. Pulses for these operations require frequencies of 10's of kHz at voltages of 200-1200 V. The oscilloscope is used for troubleshooting or verification of the high voltage pulses.

The electronics for any droplet instrument follow a relatively simple work flow. A schematic of this work flow is shown in Figure 2.18.

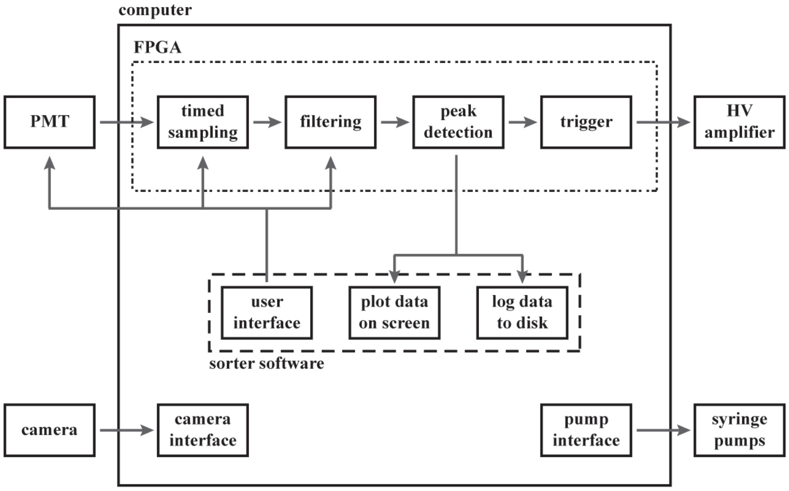

Figure 2.18: Schematic block diagram of the electrical components and data flow of the fluorescence-based droplet sorting instrument. A field programmable gate array (FPGA) samples the fluorescence intensity signal from the photomultiplier tubes, processes the data, and triggers the high voltage amplifier to actuate droplets of interest. The FPGA communicates with a Labview user interface that displays samples of the data and logs the data to memory. The PC also runs software for the user to interface with a digital high speed camera and the syringe pumps.

Chapter 3

Droplet Microfluidic Instruments

In the previous chapters, the basic principles of microfluidic droplet production, handling, and application to screening assays have been discussed. As outlined in Section 2.2, the microfluidic on-chip operations are supported by a network of external systems that control fluid flow, analyze droplet contents, and manipulate the droplets. Improvements to these external systems enable more accurate measurements and new experiments. In this chapter, we focus on two key advances in the instrumentation that controls droplet-based experiments. We discuss improvements to the optical paths used for fluorescence excitation on the droplet detection instruments, and detail the design and development of a precision thermal stage.

3.1 Fluorescence Excitation and Detection Optics

The key to a droplet-based assay is determining what has occurred within the reaction volume. As motivated in Section 2.1.3, most droplet assays rely on fluorescence measurements, owing to the vast array of fluorogenic compounds available and the relative ease with which these molecules can be conjugated to other biomolecules or incorporated into the assay. To measure the fluorescence within each droplet we need an excitation source and a detector to record the emission wavelength and intensity.

For most experiments, we use lasers for fluorescence excitation. As discussed in Section 2.2.2, the spatial confinement of our droplets and the speed at which they flow preclude the use of full-field or low intensity illumination sources. Maximizing the signal-to-noise of the collected fluorescence requires optimization of three issues: minimizing collection of stray light, maximizing excitation intensity, and maximizing collection of emitted fluorescence. The first issue is addressed by enclosing the sample and optical paths in a light-tight environment; this can be small optical tubes and a sample chamber, or may involve a dark-curtained microscopy bay.

The second and third issues are linked to the choices of instrument platform and optical components. Our instruments are typically based on an inverted fluorescence microscope to which the other optics are integrated. The microscope simplifies initial construction, as all of its components are aligned to the optical axis, and the microscope body provides mounting options for objectives, filters, and simultaneous light collection via multiple ports. Using an inverted microscope allows us to simultaneously image bright field and epifluorescence, while providing space above the microfluidic device for fluid tubing connections. The major integration required to transform the microscope to a droplet analysis instrument is coupling of the excitation lasers and fluorescence detectors to the microscope's optical path.

The inverted microscope includes a rear port for fluorescence excitation. Lasers and detection optics are coupled to the optical path through this port. The use of 30 mm optical cage cubes for the array of fluorescence filters and detectors makes the detection portion of the optics robust and simple to align with the microscope. Each of those components can be installed and aligned on the bench top away from the microscope, and this entire assembly installed onto the microscope as a unit. The assembly must simply be aligned and leveled with the optical axis of the microscope's rear port. This approach maximizes fluorescence collection.

The remaining challenge lies in maximizing excitation intensity. Aligning one or more lasers to the optical path of a microscope is non-trivial. Small angular deviations result in large deviations from uniform, focused illumination at the focal plane of the objective. The illumination intensity is also impacted by the turning mirrors used to steer the laser beam from the laser head to the microscope. Mirror materials and coatings provide maximum reflection for specific wavelength ranges. Mirror quality, as characterized by percent reflection at a given wavelength, typically correlates with mirror price. When several mirrors will be used in a system, it is best to use mirrors with the maximum reflectance, since a series of low-quality mirrors can lose several percent of the initial intensity to transmission at each mirror. In addition to mirror quality, incident angle has an impact on reflected intensity; ideally, reflection angles (twice the incident angle) of all mirrors in the system should be kept to acute angles.

Figure 3.1 shows the initial optical configuration for the droplet detection instrument [33]. While compact, the arrangement is exceptionally difficult to align and suffers from loss of laser intensity. The three things that can be improved are: 1) use of higher quality turning mirrors; 2) elimination of the periscope (M1), which is a large source of alignment error; and 3) the inclusion of dedicated mirrors for fine-tuning the laser position.

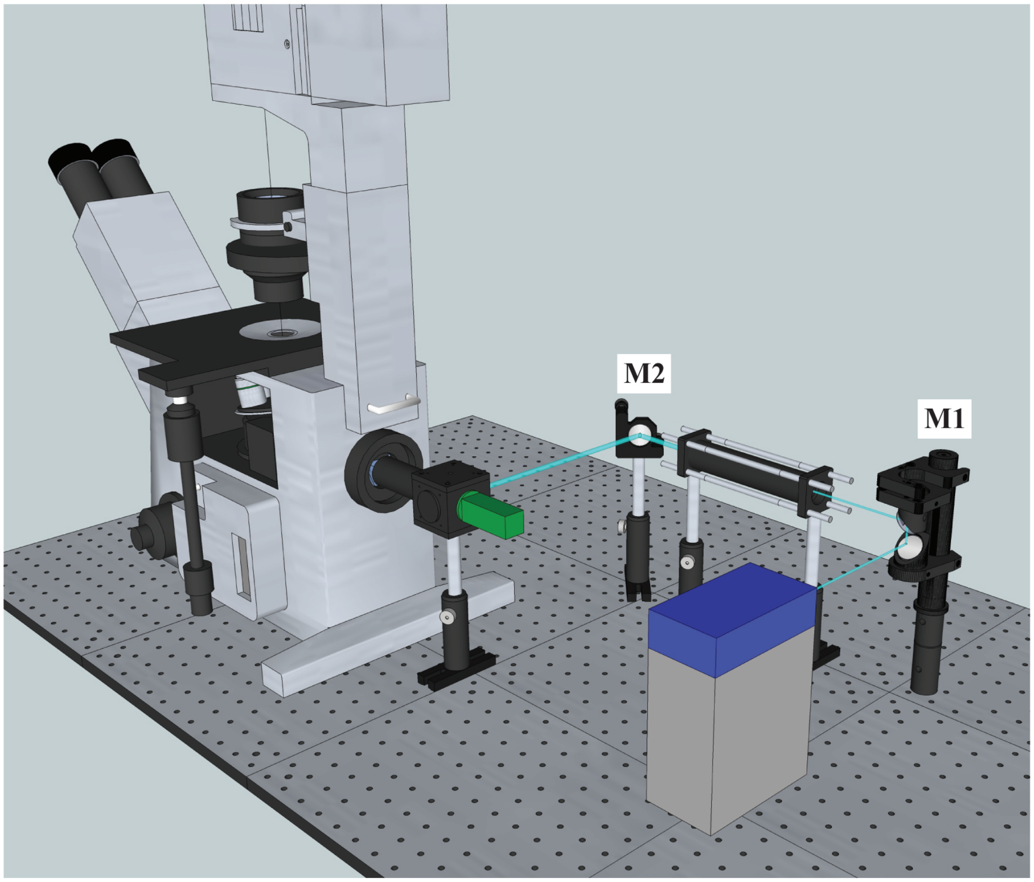

Figure 3.1: Original configuration for incorporating laser excitation and fluorescence detection via the rear illumination port on an inverted microscope. The laser head (blue) is mounted to its heatsink. The beam is brought up to the level of the illumination port by periscope M1, enlarged by a telescope, and then directed by mirror M2 into the filter cube. The photomultiplier tube (green) detects fluorescence collected by the microscope objective. Refer to Figures 2.14 and 2.15 for details on the optical paths.

Figure 3.2 shows the improved laser path. We have addressed all three improvements mentioned above. Moving the laser head to a labjack eliminates the need for the periscope, as we can precisely set the starting elevation of the laser beam. We have exchanged the aluminum mirrors for higher quality silver mirrors (Thorlabs PF10-03-P01) and incorporated gimbaled mounts for fine tuning of the beam path (Thorlabs GM100). Of particular importance, the beam path and turning motion of the mounts were selected such that the x- and y-positions of the beam at the entrance to the microscope and at the objective turret can be adjusted separately.

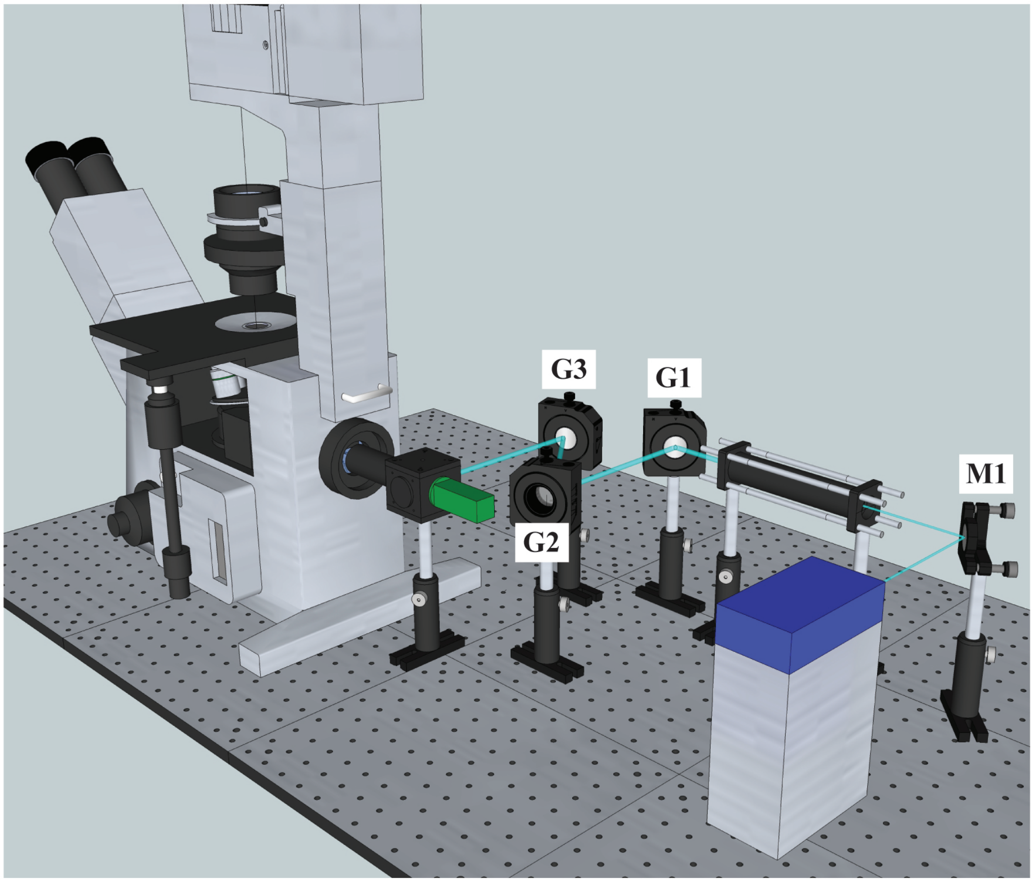

Figure 3.2: Improved configuration for incorporating laser excitation and fluorescence detection via the rear illumination port on an inverted microscope. The laser head, in blue, is mounted to its heatsink on a labjack. Using the labjack, the laser beam is brought level with the center of microscope's illumination port. Mirror M1 reflects the laser beam through the telescope to gimbaled mirror G1. G1 directs the laser beam to gimbaled mirror mounts G2 and G3. G2 is used to fine-tune position of the laser beam at the entrance to the filter cube, while G3 is used to fine-tune the position of the laser beam at the objective.

Following the installation of this new optics configuration and subsequent alignment, fluorescent detection of droplets is much improved. Due to the strong dependence of measured fluorescence on the microscope objective used, assay preparation, laser position relative to the microfluidic channel, and laser focus relative to the equator of the droplets, it is only possible to give a qualitative impression of improvements to detection. We observe roughly an order of magnitude higher intensity for a given PMT gain, but cannot quantify more precisely than that. See Section A.4 for the laser alignment procedure.

3.2 Thermal Control of Microfluidic Devices

Many of the biological systems that are studied using droplet microfluidics require temperature control. Cells and samples must be kept cool during loading and encapsulation to minimize cross-contamination from growth and expression. Following encapsulation in droplets, the samples must be incubated at an elevated temperature to promote growth and expression. Cycling of temperatures may be needed, as is the case for performing polymerase chain reactions (PCR) in droplets on-chip. These requirements necessitate the development of a versatile thermal stage for use with PDMS microfluidics.

A simple version of a thermal stage can be constructed by sandwiching a Peltier thermoelectric device between copper plates. The upper plate uniformly distributes heat from the Peltier, minimizing thermal gradients. The lower plate is a heat sink for the lower side of the Peltier and allows the thermoelectric to couple more efficiently to the environment or a heat exchanger.

The upper surface of the topmost plate is thermally coupled to the underside of the microfluidic device. Temperature feedback provided by a thermistor inserted into the upper copper plate allows a circuit to control the Peltier and regulate the temperature of the upper plate. Construction of this assembly is detailed in Appendix C.

Though the assembly discussed in Appendix C provides excellent temperature regulation, it requires a reflection microscope to image the microfluidic device. Imaging quality is degraded due to the long working distance, obstructions in the field of view from fluid tubing, and poor reflection by the thermal paste that couples the device substrate to the thermal stage. Ideally, the thermal stage would provide thermal control while still allowing the microfluidic device to be imaged in transmission by an inverted microscope. This arrangement would provide thermal control and optimum imaging of the microfluidic channels.

To enable the microfluidic device to be imaged in transmission, the thermal stage design must be altered from that shown in Appendix C and Figure 3.3(A). The Peltier must be moved off the center axis of the stage and holes must be machined through the copper plates to allow imaging. This reconfiguration is best accomplished by using multiple small area Peltier thermoelectric devices in place of the single large thermoelectric. The smaller Peltiers give uniform temperature control, while keeping the center of the stage clear for imaging. This new arrangement is shown in Figure 3.3(B). The copper stage is sized to match the standard 50 mm x 75 mm glass microscope slide used as a substrate for microfluidic devices.

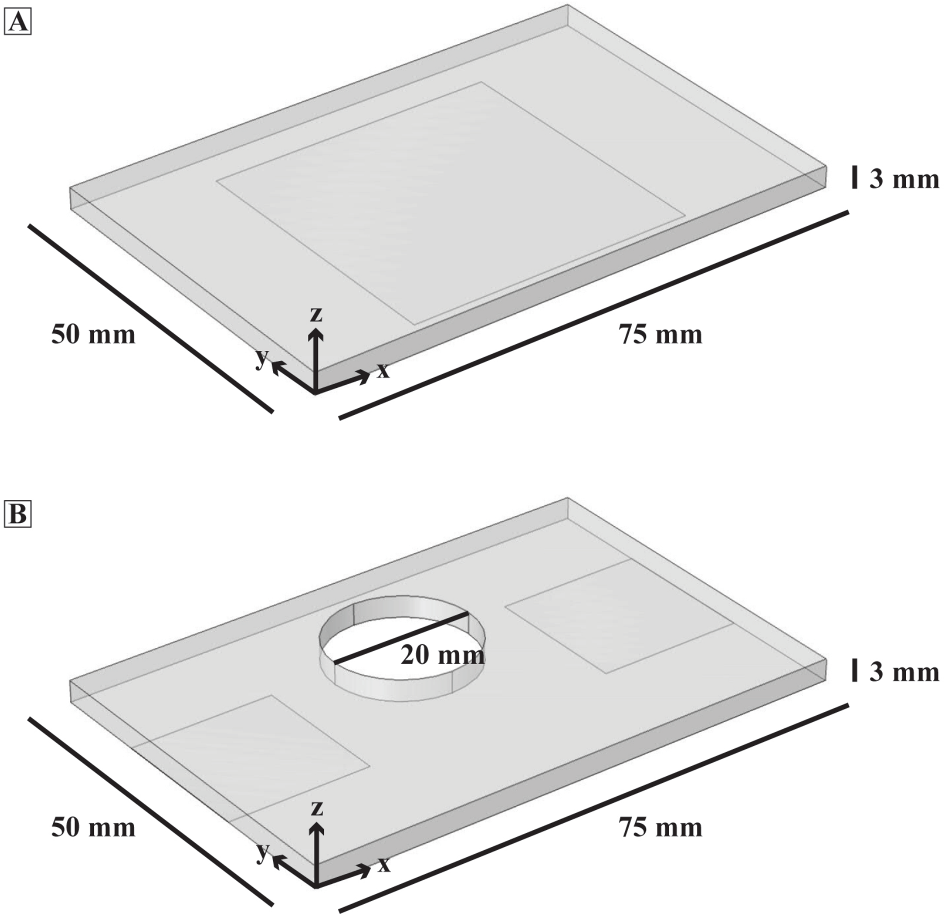

Figure 3.3: Dimensions of copper stages for comparative modeling and experimental characterization. **(A)** Solid stage coupled to a 40 mm x 40 mm Peltier device, shown as a gray outline on the underside. **(B)** Imaging stage coupled to two 20 mm x 20 mm Peltier devices, shown as gray outlines on the underside.

After designing the stage, we run comparative simulations in COMSOL to investigate the temperature distribution in a microfluidic device. Three dimensional finite element simulations compute the temperature distribution for each stage design: a single Peltier under a solid stage, and dual Peltiers under a stage with a hole. We model the microfluidic device by incorporating a glass slide and PDMS block on top of the copper stage. The simulations apply a constant temperature of 30°C to the area of the Peltier device(s) and solve for equilibrium temperature of the stage and representative microfluidic device. We assume free convection in air at all exterior surfaces with a heat transfer coefficient of 25 W/m^2K [90]. The equilibrium temperatures are plotted in two planes: the xz-plane at the center of the imaging hole ($y = 34.5$ mm), and the xy-plane at the level of the microfluidic channels ($z = 4$ mm). Results for the solid stage are shown in Figure 3.4, while results for the imaging stage are shown in Figure 3.5.

Simulations lead us to expect reasonably uniform temperature across the entire microfluidic device. The solid stage creates a very uniform temperature distribution at the channel level, as seen in Figure 3.4(B). As seen in Figure 3.5(B), the hole in the stage creates a thermal gradient across the imaging port. However, this gradient is 2°C at most, and we can tune our feedback to ensure the entire microfluidic device remains above the desired temperature. In particular, the location of the feedback thermistor will directly impact the temperature through the imaging area. Locating the thermistor near the edge of the imaging port will bring the area of the port nearer to the set point, at the cost of elevating the temperature of the rest of the device.

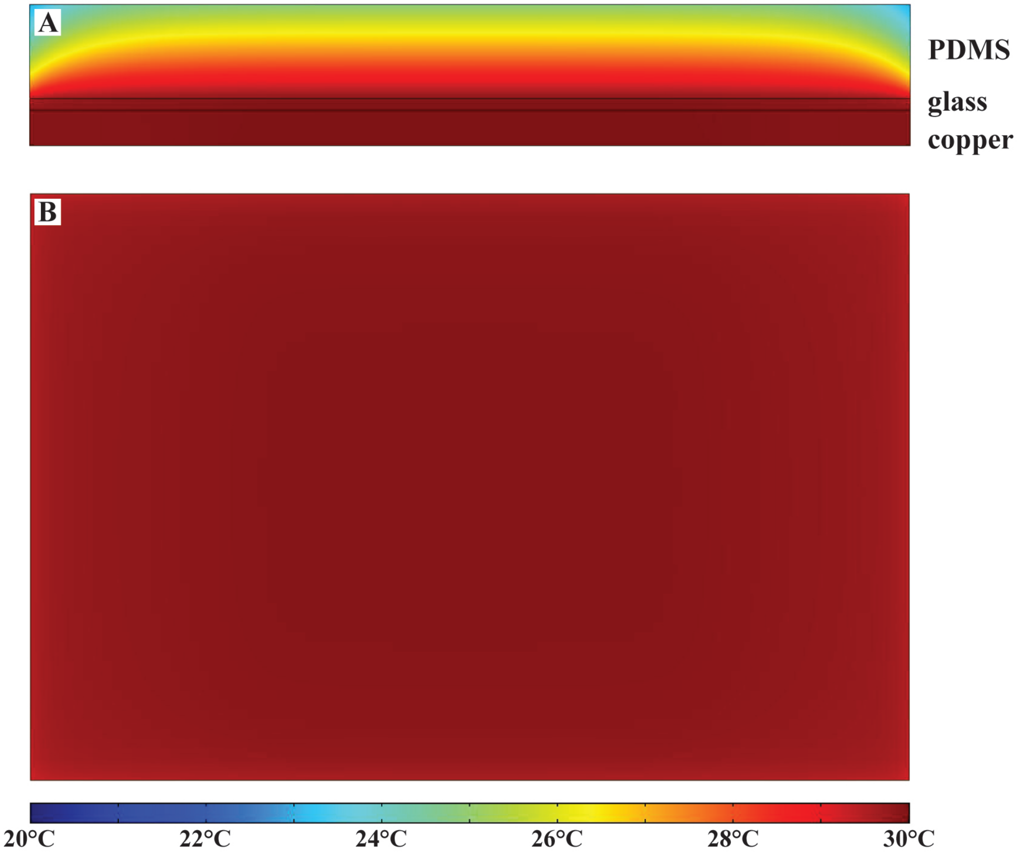

Figure 3.4: Results of steady-state COMSOL simulation for the solid stage and coupled microfluidic device. **(A)** Temperature profile of the xz-plane at y = 34.5 mm. The lowest rectangle is the copper stage and shows a uniform temperature. The middle rectangle is the glass substrate of the microfluidic device and shows temperature and uniformity similar to the copper. The upper rectangle is the PDMS piece and shows a large gradient from its interior to exterior. **(B)** xy-plane at z = 4mm, the plane of microfluidic channels, showing that the channels are subject to a uniform temperature.

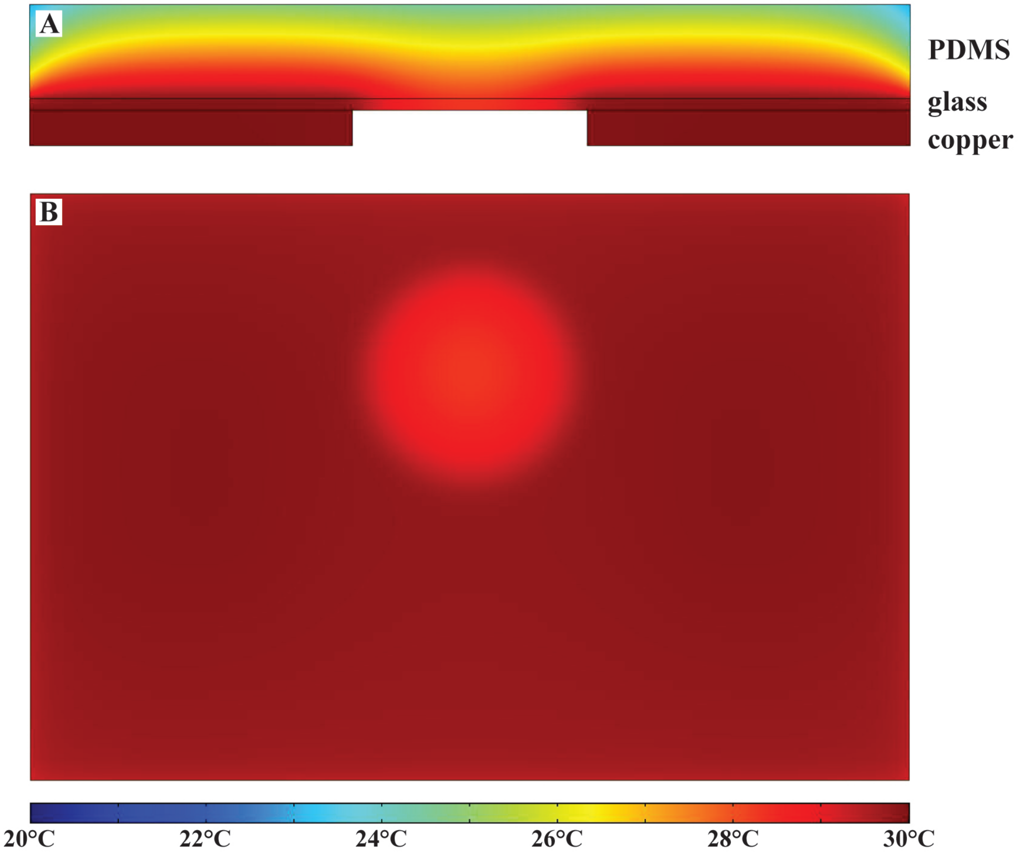

Figure 3.5: Results of steady-state COMSOL simulation for the imaging stage and coupled microfluidic device. **(A)** Temperature profile of the xz-plane at y = 34.5 mm, the center of the imaging hole. The lowest rectangles separated by a blank space is the copper stage and shows a uniform temperature. The middle rectangle is the glass substrate of the microfluidic device. The slight temperature gradient over the imaging hole continues into the PDMS layer. **(B)** xy-plane at z = 4mm, the plane of microfluidic channels. Channels crossing the imaging hole will be subject to a 1°C decrease in temperature, but the rest of the stage displays minimal gradients.

To further verify our expected temperature distribution in the imaging stage, we perform a test of the imaging stage using thermally responsive sheets embedded in a model microfluidic device. The thermally responsive sheets consist of liquid crystals embedded in a polymer matrix and are tuned in 5°C increments (Edmund Optics). We embed an alternating pattern of sheets sensitive in the 25-30°C and 30-35°C ranges in a PDMS slab at the standard microfluidic channel location, such that by imaging the PDMS/LCD sheet hybrid, we directly observe temperatures at the channel level. The results for stage temperature set points of 30°C and 37°C are shown in Figure 3.6.

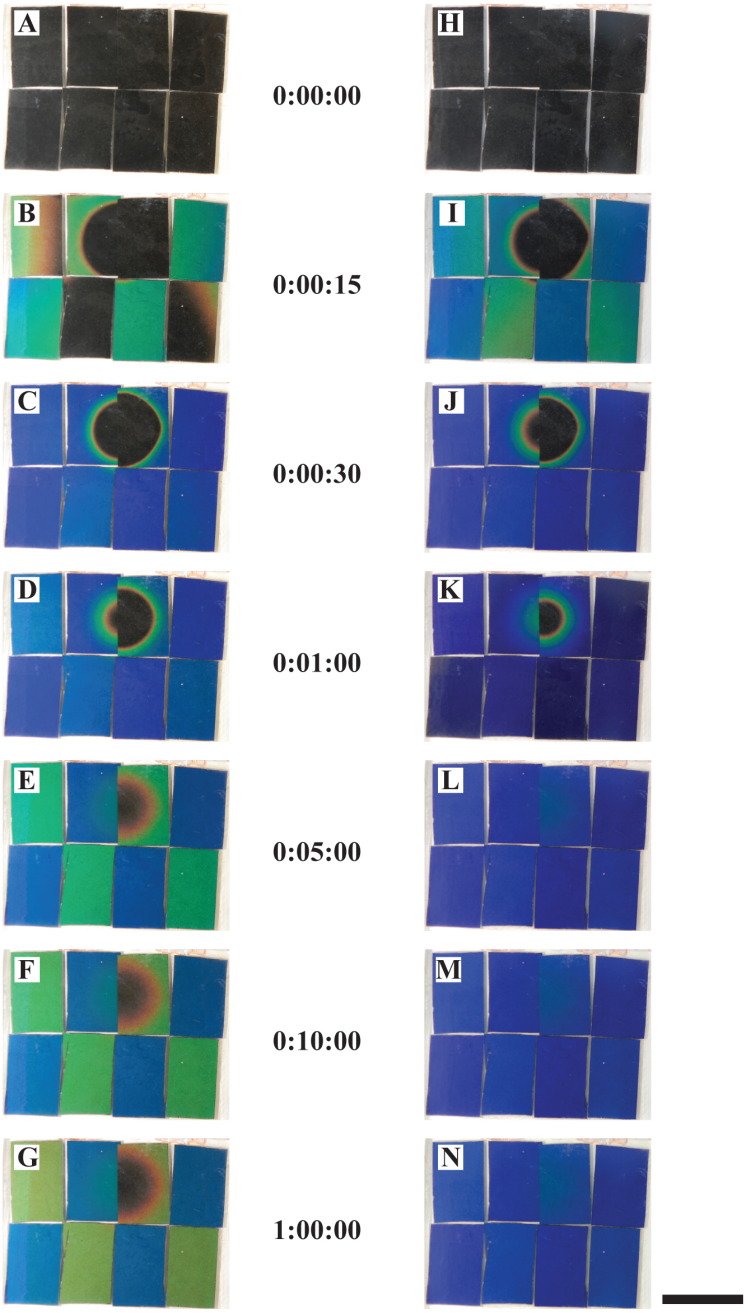

Figure 3.6: Imaging thermal gradients in a microfluidic device on the imaging stage. Thermally responsive LCD sheets display temperature ranges of: 25-30°C or 30-35°C. Black corresponds to the lowest temperature, while blue corresponds to the highest. **(A)-(G)** Temperature profile of the microfluidic device with a stage set point of 30°C. **(H)-(N)** Temperature profile of the microfluidic device with a stage set point of 37°C.

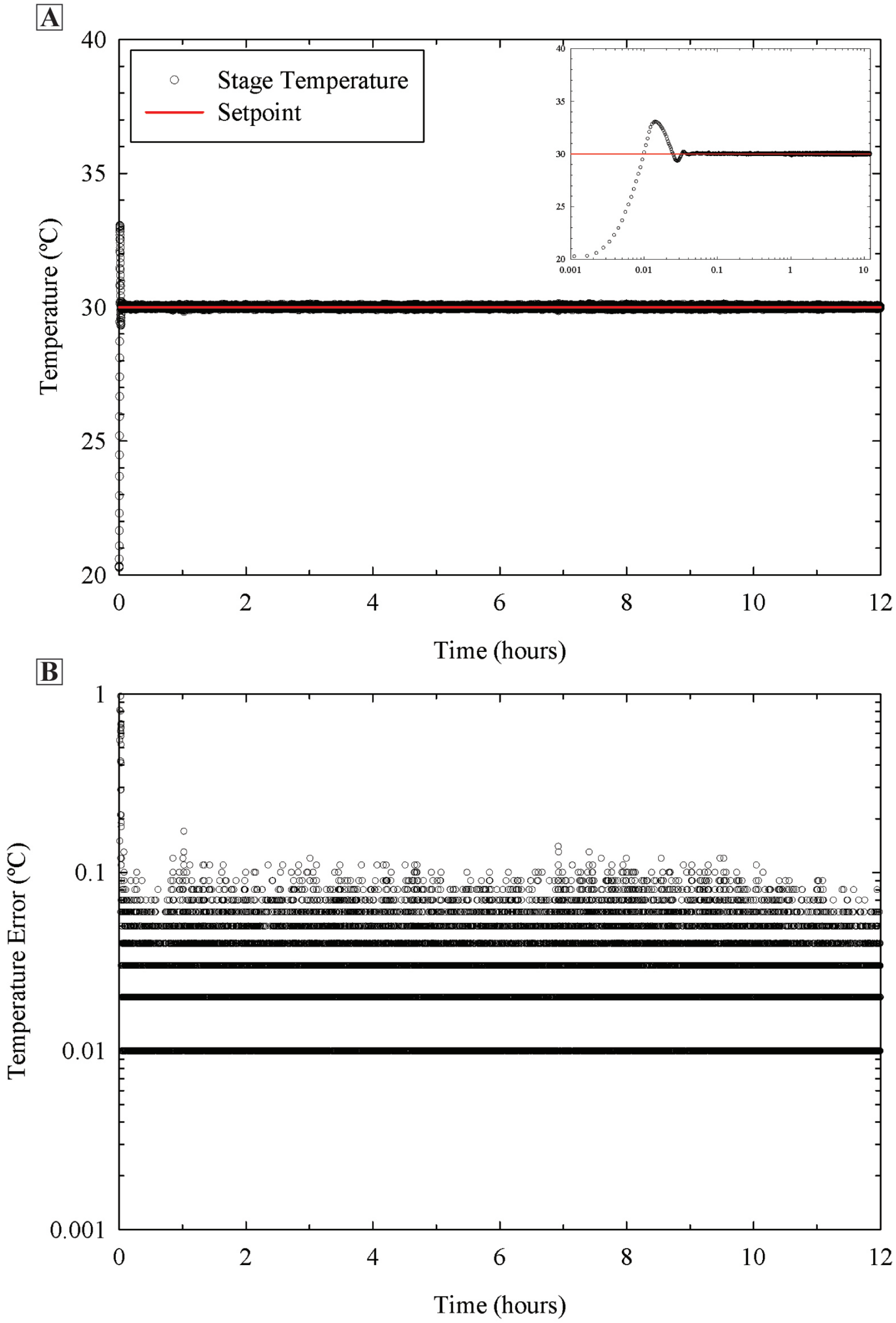

Figure 3.7: **(A)** Measured stage temperature over the course of 12 hours for 30°C set point. Inset is a semilog-x plot to highlight the temperature at startup. **(B)** Stage temperature error over 12 hours. Error is calculated as $abs(T_{setpoint} - T_{measured})$.

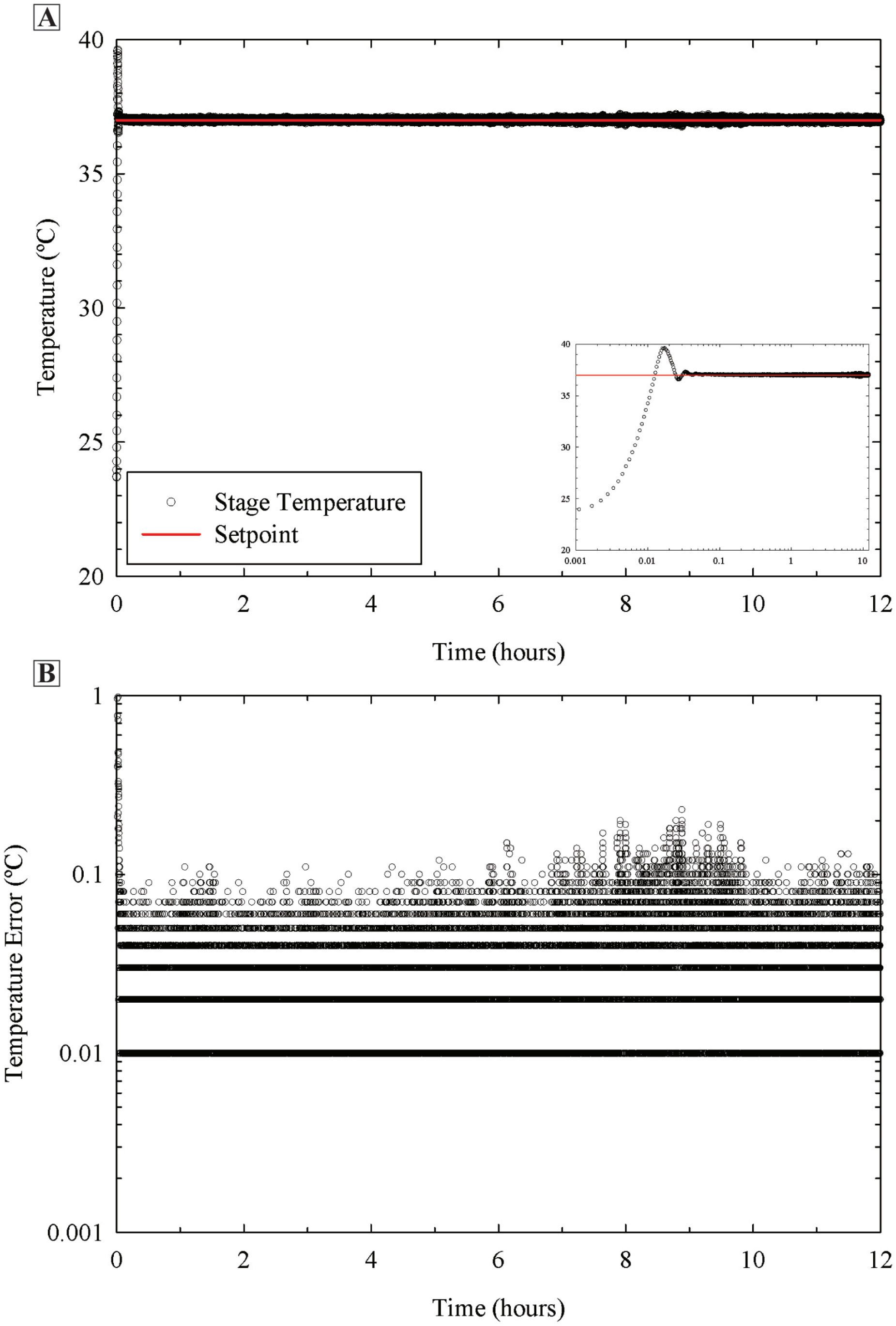

Figure 3.8: **(A)** Measured stage temperature over the course of 12 hours for 37° set point. Inset is a semilog-x plot to highlight the temperature at startup. **(B)** Stage temperature error over 12 hours. Error is calculated as $abs(T_{setpoint} - T_{measured})$.

The embedded LCD sheets enable observation of the evolution of the temperature gradients within the microfluidic device. The stage rapidly comes to temperature, but overshoots the set point slightly. Within 1 minute, this overshoot has diminished. Within 5 minutes, the overshoot has been fully corrected and the device area over the imaging port has come to its equilibrium temperature. Once this equilibrium has been established, it is stable for hours.

We also characterize the thermal stability of our imaging stage. The feedback thermistor is mounted to the bottom of the stage, halfway between the Peltier devices, at the very edge of the imaging port. Initial equilibration of the stage temperature requires approximately 5 minutes, followed by excellent stability at the set point over the course of 12 hours, as seen in Figures 3.7 and 3.8. Temperature stability for a set point of 30°C is shown in Figure 3.7, while stability for a 37°C set point is shown in Figure 3.8.

Having successfully demonstrated operation of the thermal stage, we have furthered the set of tools available for development of droplet microfluidic assays. Long term thermal stability at elevated temperature enables on-chip operations such as multi-day cell culture, PCR in droplets, and manipulations of thermally-responsive colloids loaded into droplets.

Chapter 4

Manipulating Droplet Microreactors

The key advantage to utilizing droplet systems for experiments is the ability to generate many identical samples to access large number statistics. However, this requires that each droplet act as an independent reaction volume, with no exchange of material between droplets. In this manner, differences between droplets are due solely to their contents, not to interactions with other droplets or the external environment. In this Chapter, we detail device designs and operational principles for the microfluidic channels that prepare droplet assays. We begin by considering emulsion stability and characterize the standard fluids we use for droplet assays. Then, we detail microfluidic devices that temporarily destabilize droplets to add fluid to the droplets.

4.1 Surfactant

To prevent contamination of droplet contents, all droplets must remain stable. So long as droplet contents are soluble only in the dispersed phase and the droplets are surrounded by the continuous phase, there is no exchange of material with other droplets or the channel walls. However, if the protective film of continuous phase drains away, the droplet is no longer guaranteed to be isolated.

As discussed in Section 1.5, a surfactant is used to stabilize the interface. If the continuous phase drains away, the surfactant provides steric stabilization for the dispersed phase, preventing coalescence between droplets or interactions with the channel surfaces. With a good surfactant, only extreme stress will cause destabilization of the droplets.

Since we work primarily with water/fluorocarbon systems, we are limited in our surfactant choices. Most commercially available surfactants are designed for water/hydrocarbon systems. Previous work created custom fluorosurfactants for our microfluidic systems, but the synthesis remains non-trivial and purity of the final product has proven to be of utmost importance for ensuring droplet stability [91, 92]. The most promising of these surfactants is a triblock copolymer composed of two perfluoropolyether (PFPE) blocks linked to a middle polyethylene glycol (PEG) block, shown in Figure 4.1.

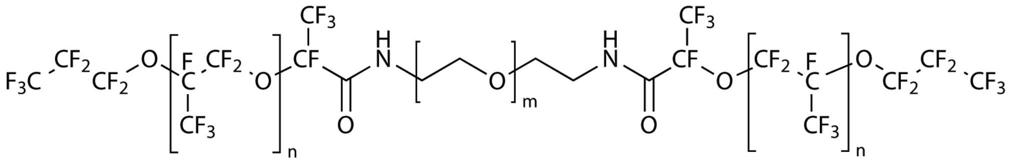

Figure 4.1: Chemical structure of the PFPE-PEG-PFPE triblock fluorosurfactant used for microfluidic experiments. As synthesized, $n = 40$ (MW = 6000 g mol^{-1}), $m = 12$ (MW = 600 g mol^{-1}).

This PFPE-PEG-PFPE triblock surfactant stabilizes aqueous water drops and is soluble in the fluorocarbon oil phases we use: Fluorinert FC-40, Fluorinert FC-3283, Novec HFE-7500, and Novec HFE-7100. The surfactant's long, heavily fluorinated PFPE blocks guarantee miscibility in the fluorocarbon phase, while the medium-size PEG middle block preferentially embeds itself in the aqueous phase. Adsorption of the surfactant at a water/HFE-7500 interface causes the interfacial tension to decrease from ~ 35 mN/m to ~ 2 mN/m. Though initial characterization of the surfactant demonstrates its effectiveness for a variety of microfluidic droplet experiments [91, 28, 33], little of the surfactant's physiochemical properties have been quantified.

Due to the finite area of the interface and the size of surfactant molecules, there is a rough geometric limit to the amount of surfactant that can occupy locations on the interface. Considering a low pressure, dilute monolayer of surfactant at the interface, we invoke a two-dimensional version of the ideal gas law to understand the effects of surfactant. We replace pressure in the ideal gas law with surface pressure, Π_s, the pressure required to prevent the surfactant film at the interface from spreading.

$$\Pi_s A = nRT \tag{4.1}$$

It is easier to consider an area per molecule, $a_0 = A/(nN_{Av})$, than total area. Introducing a_0, equation 4.1 is transformed to:

$$\Pi_s a_0 = kT \tag{4.2}$$

Since Π_s of the surfactant film opposes the interfacial tension, Π_s is also the decrease in interfacial tension attributed to the adsorption of surfactant at the interface. Thus, using Equation 4.2, for a given surfactant size, we can estimate the decrease in interfacial tension due to the adsorption of the surfactant. Conversely, a measured decrease in interfacial tension caused by a surfactant can be used to estimate the area each surfactant molecule occupies.

However, the ideal gas law is applicable only for surface pressures below ~ 0.1 mN/m. At these low pressures, the nonpolar chains of the surfactant molecules lie flat on the interface. As surface pressure increases, the surfactant layer transitions from a gaseous state to a liquid expanded state and then to a liquid condensed state. For extremely high surface pressures, the layer becomes solid-like. In the solid-like extreme, the surfactant is packed so tightly that the nonpolar chains are oriented perpendicular to the interface and each surfactant molecule occupies its minimum area on the interface [93].

The highest pressure a surfactant film can support, the collapse pressure, Π_c, occurs for $a_0 \sim 0.2$ nm^2 per molecule. This value of a_0 corresponds to a surface pressure of $\Pi_c = \Pi_s \sim 20 - 50$ mN/m [94]. Considering our PFPE-PEG-PFPE triblock and the ~ 30 mN/m decrease in interfacial tension it creates, the surfactant molecules must be compressed beyond the gaseous state. Hence, we estimate a value of a_0 of roughly 0.25 nm^2 per molecule.

Using the C-C bond distance of 1.54 $\mathring{A}$, our 40 unit PFPE tails are each roughly 20 nm long and the area occupied by these chains lying on the interface far exceeds the 0.25 nm^2 per molecule we expect based on the surface pressure estimate. Thus, the surfactant molecules must rearrange once adsorbed to the interface, orienting their PFPE tails perpendicular to the interface and packing very tightly. This tightly packed structure provides excellent steric hindrance and strong adsorption to the interface, both of which contribute to the emulsion stability observed when using this surfactant.

Dynamic interfacial tension curves for the surfactant in a water/HFE-7500 system are measured using a pendant drop tensiometer. A sample curve for low surfactant concentration is shown in Figure 4.2. Though it takes several minutes to evolve, the water/HFE-7500 interfacial tension decreases to values near the resolution limit of the instrument. The magnitude of this decrease in interfacial tension is verified by measurements of identical samples using pendant drop, DuNuoy ring, and spinning drop tensiometry. Since the interfacial tension decrease far exceeds estimates made above using geometric arguments and the ideal gas law, we conclude that there are two timescales for the stabilization of the interface: a very rapid initial adsorption of surfactant up to the geometric limit with the nonpolar chains lying on the interface, followed by a long-time reorganization of surfactant geometry that permits additional loading of molecules and further decreases the interfacial tension. This second timescale is what is observed in the plot in Figure 4.2.

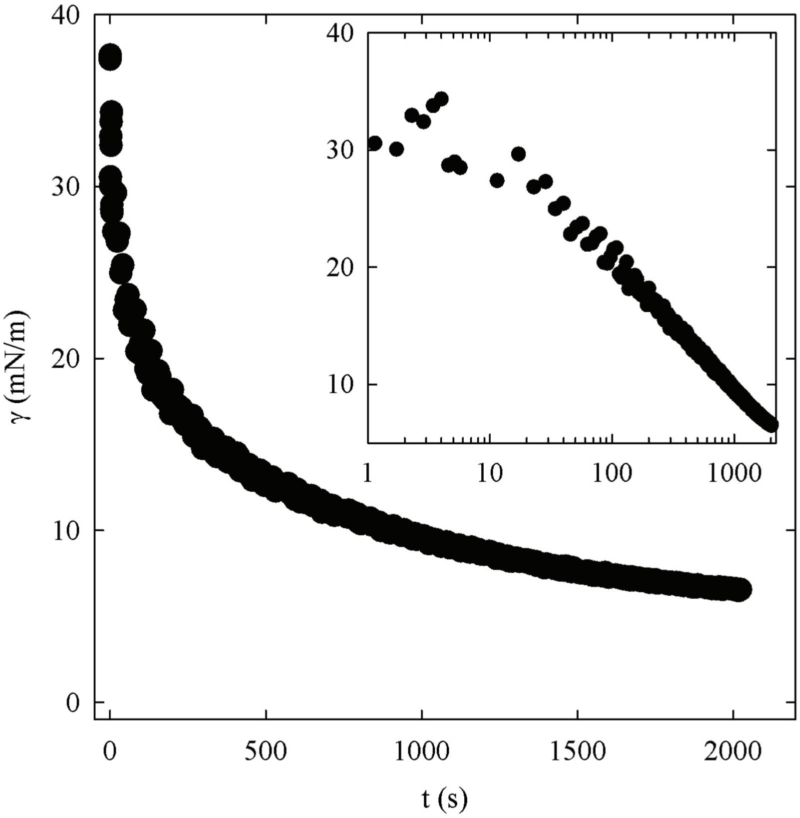

Figure 4.2: Sample plot of interfacial tension versus time for a deionized water droplet in HFE-7500 containing 0.02wt% PFPE-PEG-PFPE surfactant. The inset shows a semilog-x plot of the same data; the linear nature of data points on the inset plot suggests an exponential decay of the surface tension with time.

4.1.1 CMC of the Triblock Surfactant

The long-time adsorption of surfactant on the interface can be limited by diffusion of surfactant molecules through the solvent if the surfactant is sufficiently dilute. We use this to determine the critical micelle concentration (CMC) of the surfactant [95, 96]. This value is important to characterize, since working with surfactant concentrations above the CMC ensures the greatest emulsion stability. Above the CMC, surfactant molecules in solution group into ordered micellular structures and provide excess surfactant to the interface as needed. As surfactant molecules desorb from the interface, new molecules are already present to take their place and do not need to diffuse in from the bulk portion of the solvent. This maximizes coverage of the interface at all times and thus maximizes stability.

To determine the CMC for our triblock surfactant in a water/HFE-7500 system, we measure the dynamic interfacial tension for a range of surfactant concentrations, such as the plot in Figure 4.2. A simple decaying exponential of the form: $\gamma = ae^{-bt}$ is fit to each curve and a characteristic time, $\tau = 1/b$, is extracted. These characteristic times are plotted as a function of surfactant concentration in Figure 4.3.

We observe a monotonic decrease in the characteristic time with increasing surfactant concentration until a concentration of roughly 0.7wt% is reached. All microfluidic experiments are performed with 2wt% surfactant solutions, thus ensuring that we work above the CMC and maximize the stability of our emulsion.

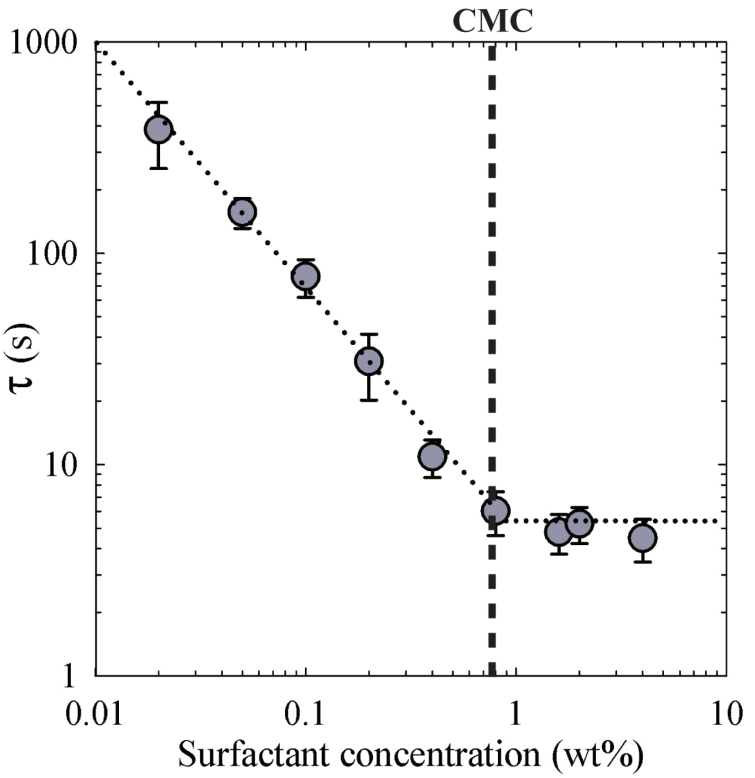

Figure 4.3: Plot of characteristic time versus concentration of PFPE-PEG-PFPE triblock surfactant for a water/HFE-7500 system. Characteristic time constants are determined from exponential fits to data such as that shown in Figure 4.2. We denote the CMC as the minimum surfactant concentration at which τ no longer changes.

4.2 Manipulation of Droplet Contents

Production of microfluidic droplets, detailed in Section 1.4, is reliable and allows for the simultaneous encapsulation of one or more dispersed phases [97, 98, 33]. However, experiments often require separate encapsulation and processing of samples until a key step, at which point droplets must be coalesced together to combine their contents. Examples of such situations include introduction of a lysis buffer or stain to process cells following growth in emulsion droplets [28], or combination of droplets containing different cell lines for a competition assay or cell fusion [99].

Unlike bench top experiments, where vials and pipettors perform these operations on bulk samples, microfluidic droplet systems preclude manual operations due to droplet size, fragility, and large sample numbers. This problem is made tractable by controlling fluid flows to bring select droplets together and cause them to coalesce. This process requires:

1. The triggering mechanism for coalescence between droplets must overcome the steric stabilization provided by the surfactant.
2. The coalescence must be controllable and specific to particular droplets.
3. The droplets must return to being stable after coalescing.

Though work has explored mechanisms for causing droplet coalescence in the absence of surfactant stabilized systems [100], we focus here on those systems employing surfactants, as they are a necessary part of the experiments the devices are designed for.

4.2.1 Electrocoalescence

Initial microfluidic droplet coalescence took lessons from bulk emulsion research and employed electric fields to coalesce adjacent aqueous droplets. Electrocoalescence can be performed with electrodes directly in contact with the aqueous phase [26, 101] or simply by polarizing the droplets with an external electric field, as shown in Figure 2.2(A)-(C), with local attraction between neighboring droplets causing coalescence [102, 103, 104, 105, 106]. Electrocoalescence fulfills requirements 1 and 3 in the list above, as the surfactant is not affected by the process and restabilizes the interface of the new droplet. Requirement two is achieved by synchronizing and pairing droplets in the fluidic channel upstream of the electrodes [26].

While electrocoalescence of paired droplets is quick and reliable, it necessitates the production of two droplet populations, with at least one of the populations being pre-made and reinjected onto the electrocoalescence chip. Often times, the same reagent is being added to the entire population of droplets and does not require encapsulation in a droplet itself. In this case, a better scheme employs a channel near the electrodes that fuses with each passing droplet and injects a small volume into the droplet. This process is known as picoinjection [27] and is shown in Figure 2.2(D)-(F).

Picoinjection has the advantage of not requiring synchronization of droplet pairs. This simplifies device design as well as operation. So long as droplets maintain a minimum separation, small fluctuations in flow that would affect pairing have no effect on picoinjection. Ideally, these two modes of electrocoalescence could be combined to provide the synchronization-independent operation of picoinjection with the ability to merge multiple pre-encapsulated droplet populations.

4.2.2 Droplet-Droplet Picoinjection

An ideal droplet merging device would not require upstream pairing of droplets, but rather would introduce one population of droplets to the other at a picoinjector-like junction near the electrodes. Initial efforts show positive results, with a coalescence efficiency of 70% [107]. Figure 4.4 is an image sequence of droplet merging in this device.

The standard picoinjector demonstrates excellent performance without droplet pairing because the aqueous interface is pinned at the end of the injection channel, as seen in Figure

2.2(A). The pinned interface and resulting Laplace pressure allows the aqueous injection line to be pressurized relative to the main channel, ensuring the interface remains located at the junction and ready to merge with the next droplet that passes [27]. Since this interface does not exist between the oil phases in the droplet-droplet injection device shown in Figure 4.4, there is no easy method of pinning a droplet there. The continuous phase will always flow around the droplets, causing the droplets to move. This limits coalescence efficiency and forces merging to rely on a sensitive balance of fluid flows.

Designing an obstruction to trap droplets while permitting flow of the continuous phase and releasing the lead droplet upon coalescence with a passing droplet is non-trivial. Following studies of droplet trapping [108, 109], we design a droplet buffer that permits partial trapping of injection droplets. As shown in Figure 4.5, a spaced array of posts combined with an alcove in the channel ceiling trap a droplet, but allow continuous phase oil to bypass the trapped droplet.

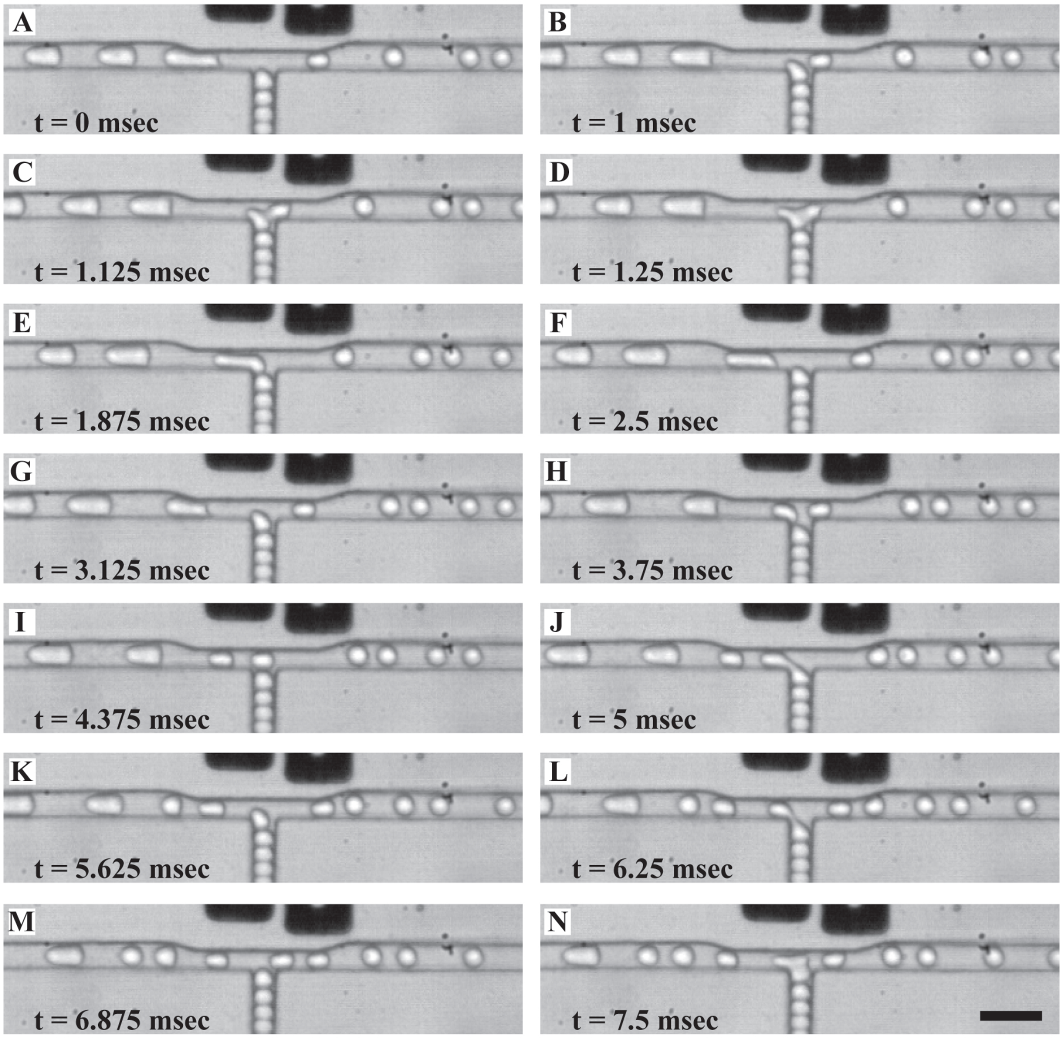

Figure 4.4: Time series of initial droplet-droplet picoinjection. One droplet population is reinjected from the right and meets the second droplet population coming up the leg of the T-junction. The black areas are metallic electrodes that generate an electric field to coalesce droplets. Scale bar represents 50 μm.

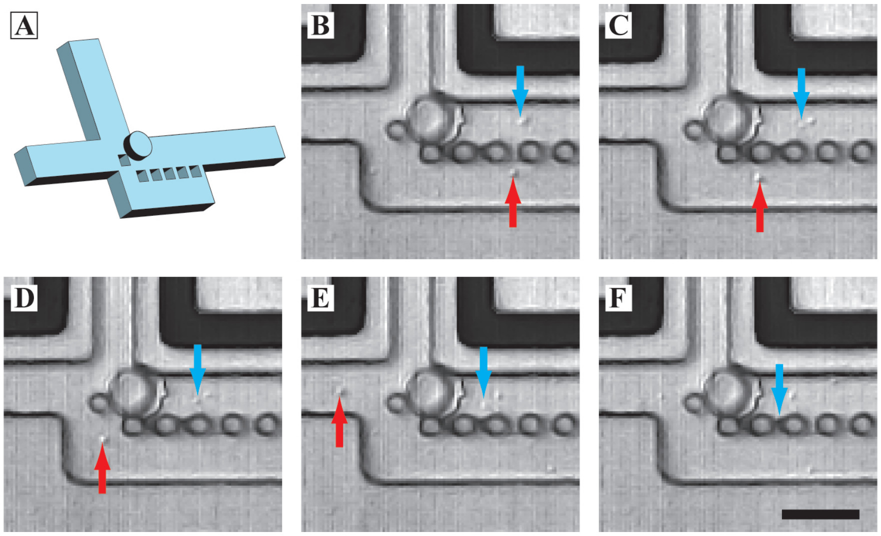

Figure 4.5: Trapping of a microfluidic droplet via a cylindrical alcove in the microfluidic channel ceiling. **(A)** Rendering of the microfluidic channel showing the alcove and bypass areas. **(B)**-**(F)** Time series of a single droplet trapped in the alcove. Blue and red arrows highlight small tracer particles carried by the continuous phase. The particles flow around the trapped droplet, indicating that flow of the continuous phase is insufficient to push the droplet out of the alcove. Scale bar represents 50 μm.

Continuous phase must be allowed to flow, otherwise droplets will not be pushed into the post array buffer to keep it full and ready for coalescence with passing droplets. Since the droplets are buoyant, the droplet nearest the exit of the buffer will float up and setting into the alcove, giving it holding pressure to resist incoming flow [110].

The presence of multiple droplets in the buffer forces the first droplet out of the buffer. The first droplet position has insufficient holding pressure to resist the pressure that builds up as droplets occlude the post array and bypass channel. This results in droplets being released into the main channel with defined, but uncontrolled frequency, as seen in Figure 4.6. Using a design such as this, coalescence efficiency is not improved over the initial value of 70%.

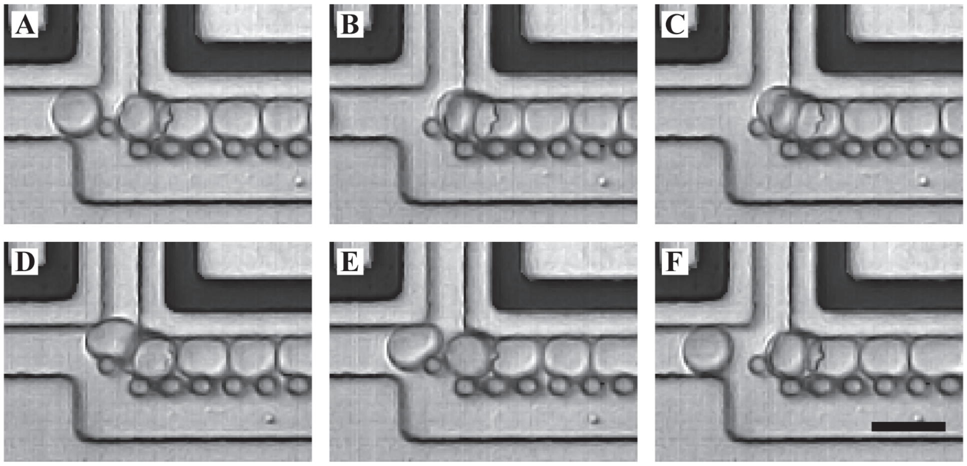

Figure 4.6: Time series of buffer failure. The holding pressure of a single droplet in the cylindrical alcove is insufficient to resist the pressure of a packed emulsion extending beyond the continuous phase bypass channel. Incoming droplets push the first droplet out of the buffer. Scale bar represents 50 μm.

4.2.3 Reinjected Droplet Coalescer

In addition to the droplet-droplet injection device, we develop a second device for the electrocoalescence of pre-made droplets [88]. Existing methods for coalescing droplets require that at least one popluation of droplets be created on the coalescence device [26, 111, 18, 100, 112]. Existing designs for the coalescence region require specific conditions on droplet size ratio [28], droplet separation [100], and flow rate [113, 114]. These requirements must be balanced against the requirements for proper droplet production and downstream flow. This limits the overall usefulness of the coalescence operation, as droplet size and throughput must be tuned for ideal coalescence instead of ideal experimental conditions.

To address robustness of reinjection and ensure that we have pairs of alternating droplet species, we design a reinjection channel that is similar to the flow focusing junction shown in

Figures 1.2(B)+(C). The reinjection geometry brings two droplet species together in opposed channels, seen in Figure 4.7. As one droplet exits the channel, it occludes the flow of continuous phase in the main channel and prevents a droplet in the opposed channel from exiting simultaneously [115]. This blockage increases pressure in the main channel and the opposed droplet channel, which pushes the initial droplet downstream and makes a droplet from the opposed channel most likely to enter the main channel next. Since this mechanism relies on small pressure fluctuations to operate robustly, precise control of small pressures in each droplet population is required. Pressure control is achieved using hydrostatic pressure to drive fluid flow.

Downstream of the reinjection junction, droplets are trapped near electrodes and coalesced, as seen in Figure 4.8. The droplet trap use the Laplace pressure of an incoming droplet to pin it in place. The leading droplet enters the trap, encounters the constriction in the channel, and cannot pass. Oil is diverted around the droplet, through the bypass channels. Only after additional droplets have entered the trap, blocked bypasses, and coalesced with the intial droplet, is there sufficient fluid pressure to overcome the Laplace pressure of the droplet and force it through the constriction [116].

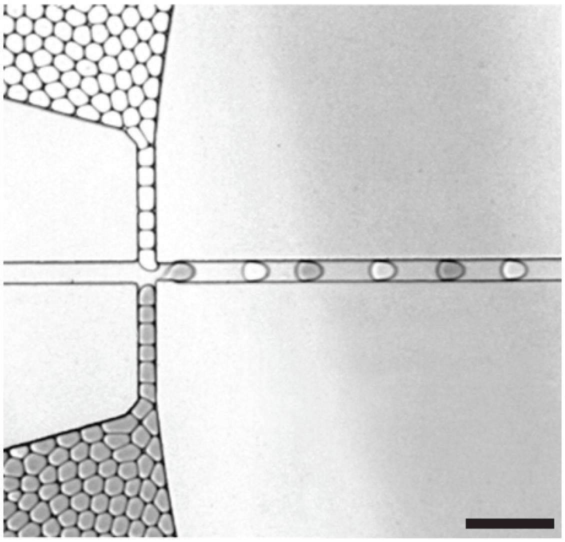

Figure 4.7: Simultaneous reinjection of two droplet species. White droplets and gray droplets are forced to alternate as they flow through the channel junction. The presence of one droplet in the junction causes a buildup of pressure in the second droplet line, making it favorable for a droplet of the second population to enter the junction. Oil is added from the left to space the droplets apart from one another. Scale bar represents 100 μm.

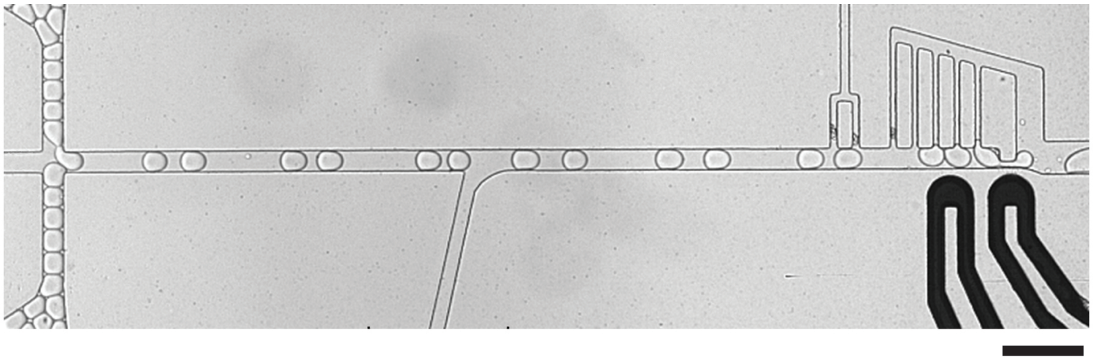

Figure 4.8: Alternating droplets flow from the channel junction at left toward the pair of electrodes at right. After passing auxiliary channels above and below the main channel, the droplet arrive at a constriction and series of bypasses. The first droplet plugs the constriction in the main channel, forcing continuous phase through the bypasses. Other droplets arrive and plug successive bypass channels. Once all bypasses are all blocked, droplets are forced into contact and the electrodes cause all droplets to coalesce. The resulting large droplet flows through the constriction. The process then repeats with the next series of droplets. Scale bar represents 100 μm.

With this coalescence device, we are able to robustly coalesce droplet pairs or trains of identically-sized droplets, an operation that is unachievable with other high throughput coalescence microfluidic designs. The device relies only on an incoming stream of alternating droplet species. Multiple bypasses at the point of coalescence allow tuning of device operation for coalescence of multiple droplets.

4.2.4 Passive Droplet Coalescence

The external function generators and high voltage amplifiers required for electrocoalescence adds unnecessary complexity to droplet experiments, and the interaction of strong electric fields with cells and biological samples is of concern. A method of controllably coalescing droplets without an applied electric field is needed. We pursue an alternative method of triggering coalescence between droplets that relies on passive techniques to control the surfactant-stabilized interfaces.

Alcohols and fluorinated alcohols are known to modify the interfacial tension of emulsions and can be used to destabilize surfactant-laden interfaces [117, 118]. Paired with hydrodynamic forcing of droplet interfaces [100, 119], the controlled addition of alcohol to an emulsion in a microfluidic device results in electrode-free coalescence of aqueous emulsions. This electrode-free coalescence is of interest for biological applications of microfluidic devices, including collection or analysis of biological assay samples [120, 121, 122], and microfluidic droplet microreactors [33, 92].

Within our microfluidic device, three key operations must be performed to ensure robust, controlled coalescence of aqueous droplets via destabilization with a fluoroalcohol. The device geometry is shown in Figure 4.9. First, droplets are paired (region I) and steered to the wall of the channel nearest the point where fluoroalcohol is introduced (region II). Second, the fluoroalcohol is brought into contact with the droplets without disturbing droplet pairing and causes coalescence (region III). Third, the droplets are restabilized, so they can be collected off-chip or subject to further processing (region IV).

To pair droplets, we employ a Y-channel design that brings droplets species together. From the lower arm of the Y, we reinject a pre-made population of 20 μm diameter droplets. From the upper arm of the Y, we form droplets with diameter 40 μm. Forming one droplet population on-chip and reinjecting the other allows us to tune the droplet production frequency to the droplet reinjection rate and thus synchronize the two droplet streams. This proper pairing is shown in Figure 4.10(A).

Figure 4.9: Schematic of the microfluidic device for coalescence of droplet pairs by addition of fluorinated alcohol. Droplet pairing occurs in region I, and the pair are brought together and steered toward the bottom wall in region II. Fluorinated alcohol is added to the continuous phase in region III and the droplets coalesce. The coalesced droplets are restabilized by dilution of the alcohol and the addition of fresh surfactant in region IV. Scale bar represents 500 μm.

Once synchronized, each droplet pair flows down the leg of the Y. Here, the smaller droplets catch larger droplets, as the smaller droplets sample less of the flow profile and thus experience a higher average velocity [26]. In early experiments, we observe a failure of droplet coalescence if droplets are not in contact with the sidewall of the channel where the fluoroalcohol is introduced. To steer the droplets to the lower channel wall, we incorporate a tapering attic feature in region II. Since the water droplets are buoyant in the fluorocarbon oil, they float to the top of the fluidic channel and enter this attic region, as shown in the schematic in Figure 4.10(C). The width of the attic decreases as the droplets flow downstream, thus forcing them to the lower wall of the channel, as seen in Figure 4.10(E). It is at this wall of the channel that we introduce the fluoroalcohol (region III). Single droplets are shown in Figure 4.10(D)+(E) for clarity. Droplet pairs follow the same trajectory as single droplets.

To characterize the guiding effectiveness of the tapered attic feature, we track droplets as they flow through region II. The average position of droplet centers is plotted as a function of distance along the channel in Figure 4.10(F). We also plot the average position of droplets in an identical channel without the attic feature. These plots confirm that the attic feature steers droplets to the lower wall of the channel. With the attic channel missing, droplets are located much closer to the center of the channel when they encounter the fluoroalcohol stream.

Heptafluorobutanol (PFB) is used as the destabilizing fluoroalcohol phase. At the point of PFB introduction in region III, the droplet pairs contact the stream of PFB, pass through a slight constriction, and coalesce with one another. Following exposure to the PFB stream, droplets encounter a fresh stream of pure HFE-7500 containing additional PFPE-PEG-PFPE surfactant in region IV, which promotes collection of stable droplets. The additional flow increases the continuous phase velocity and causes droplets to accelerate away from one another, ensuring that they are separated by oil. The flow also dilutes the concentration of

PFB in the oil, giving a final concentration of approximately 1vol% PFB in the collected emulsion.

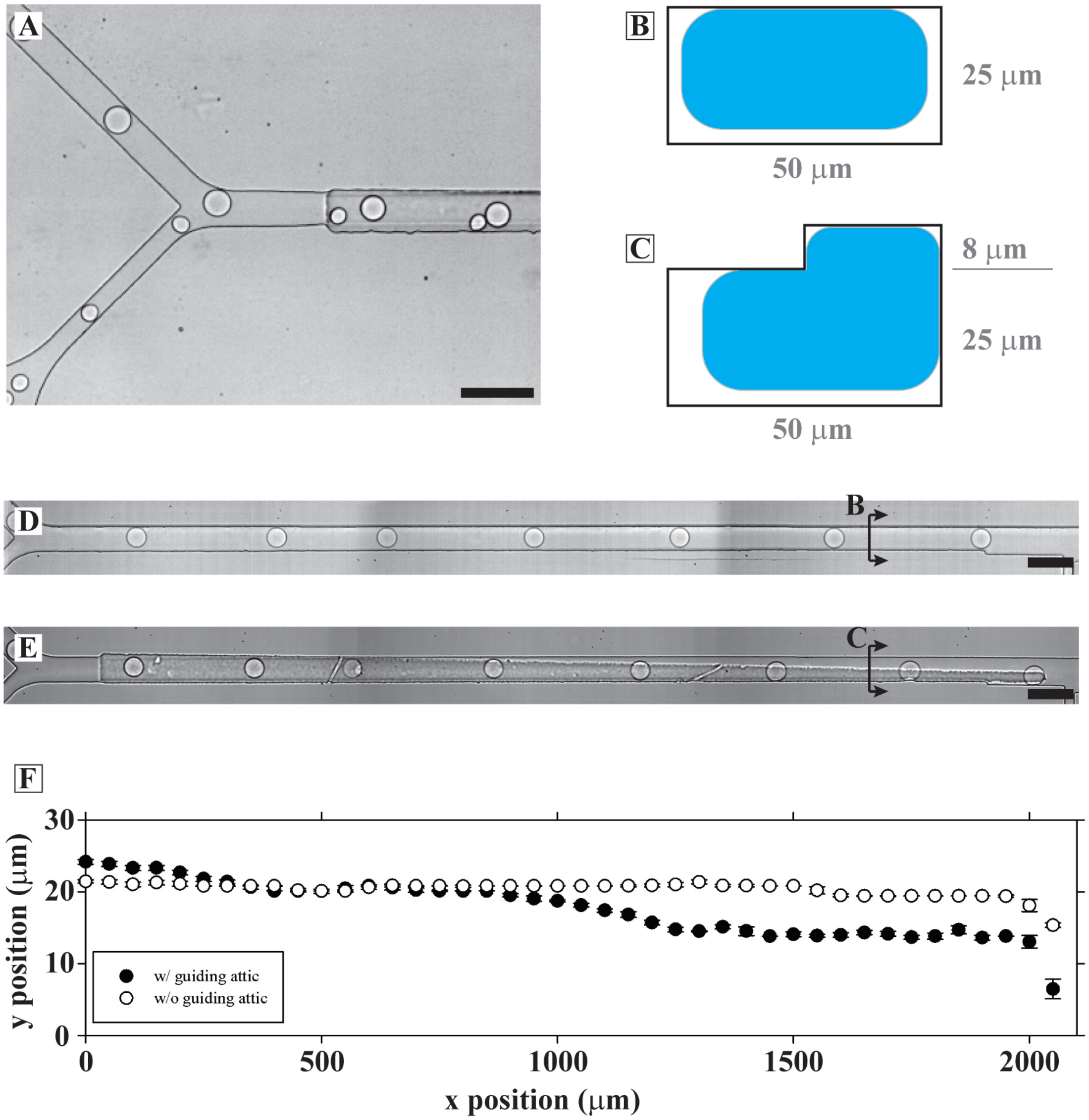

Figure 4.10: Pairing of droplets and control of droplet position in the microfluidic channel. **(A)** Pairing of 20 μm and 40 μm diameter droplets. **(B)** cross section of regular channel in region II. **(C)** cross section of channel with guiding attic in region II. **(D)** Overhead view of regular channel in region II with cross section (B) indicated. **(E)** Overhead view of channel with guiding attic in region II with cross section (C) indicated. **(F)** Measured position of droplet centers with and without guiding attic. Scale bar represents 100 μm.

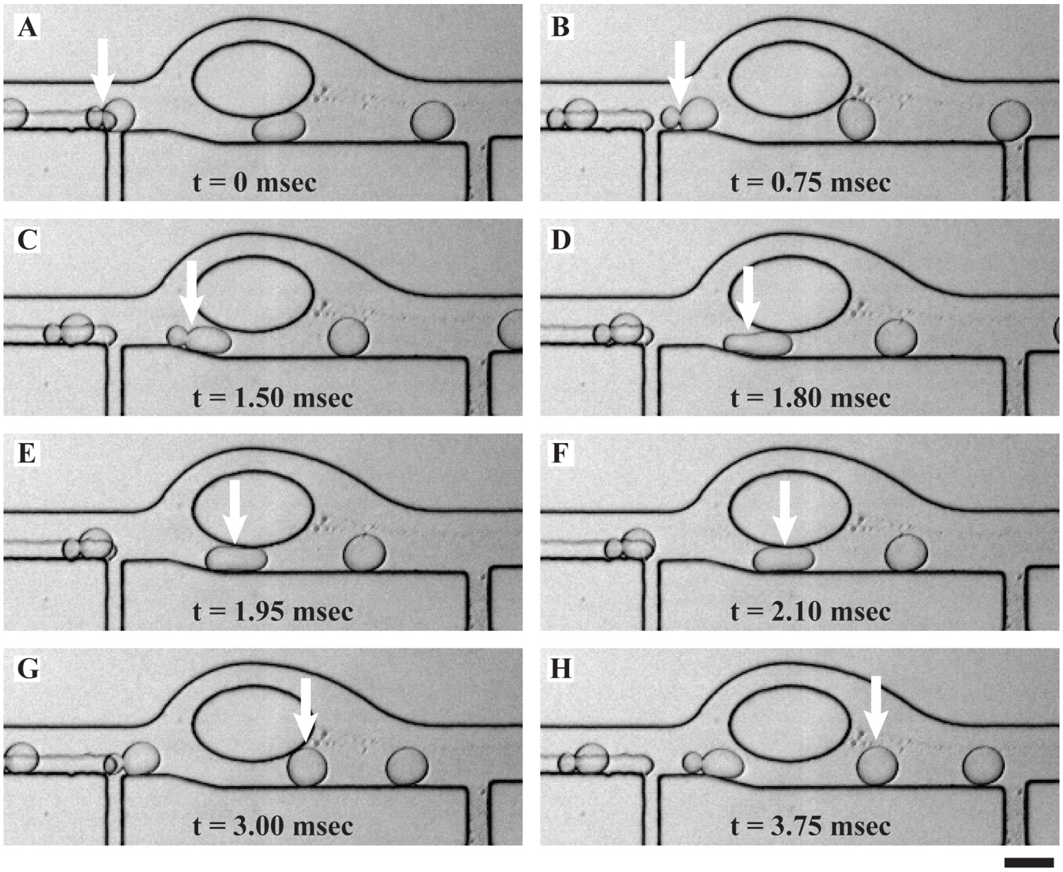

Figure 4.11: Droplet pairs enter from the left and encounter the PFB stream entering from the first side channel. Droplets are engulfed by PFB, pass through an accelerating flow and coalesce. Scale bar represents 50 μm.

We image the coalescence with a high speed camera to capture dynamics of the droplet interactions. A series of frames from one such movie are shown in Figure 4.11. As the large droplet exits the end of the attic feature, it enters the vicinity of the PFB stream. Once the thin oil shell surrounding the droplet drains away, the PFB contacts the droplet interface and within 3 msec wets the entire interface, pulling the droplet into contact with the PFB and channel wall. The smaller droplet follows and becomes stuck to the first droplet. After passing through the constriction, the droplets merge and then encounter the surfactant-rich restabilizing oil.

4.2.5 Quantifying Passive Coalescence Efficiency

To characterize the coalescence efficiency of our microfluidic device, we encapsulate fluorescent components in the droplets. We pre-make and reinject a population of 20 μm diameter droplets containing 0.5 mg/mL RITC-dextran (MW = 70 kDa) in water. The 40 μm droplets made on-chip contain 0.5 mg/mL FITC-dextran (MW = 70 kDa) in water. Thus, the small droplets appear red when imaged with a fluorescence microscope, while the large droplets appear green, as shown in the schematic of Figure 4.12.

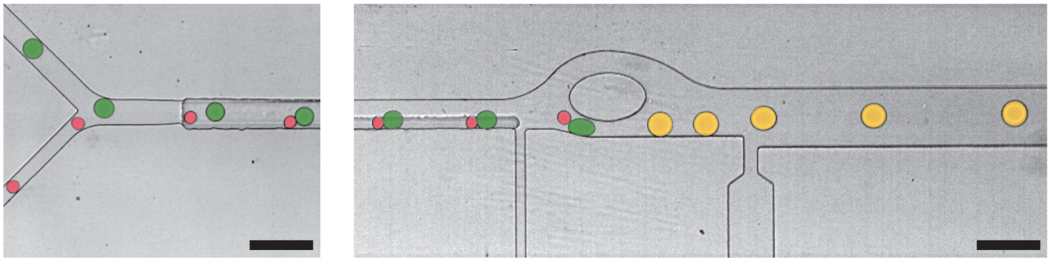

Figure 4.12: Schematic of planned two-color assay. Small red and large green droplets are coalesced as a pair and flowed off-chip for collection and analysis. Scale bar represents 100 μm.

Imaging the collected emulsion in a fluorescence confocal microscope allows quantification of the efficiency of coalescence by simultaneously measuring fluorescence intensity in both red and green wavelength bands. Uncoalesced droplets will contain only red or green fluorescence, while coalesced droplets will contain both. Droplet diameters are measured to characterize multiple coalescence events.

As seen in Figure 4.13, the emulsion collected downstream of the coalescence device is stable and close to exactly what we desire. A majority of collected droplets appear yellow, corresponding to the presence of both red and green fluorescent dyes. The emulsion shows some polydispersity and multiple merging events, but is no worse than what is produced by an electrocoalescence device [123].

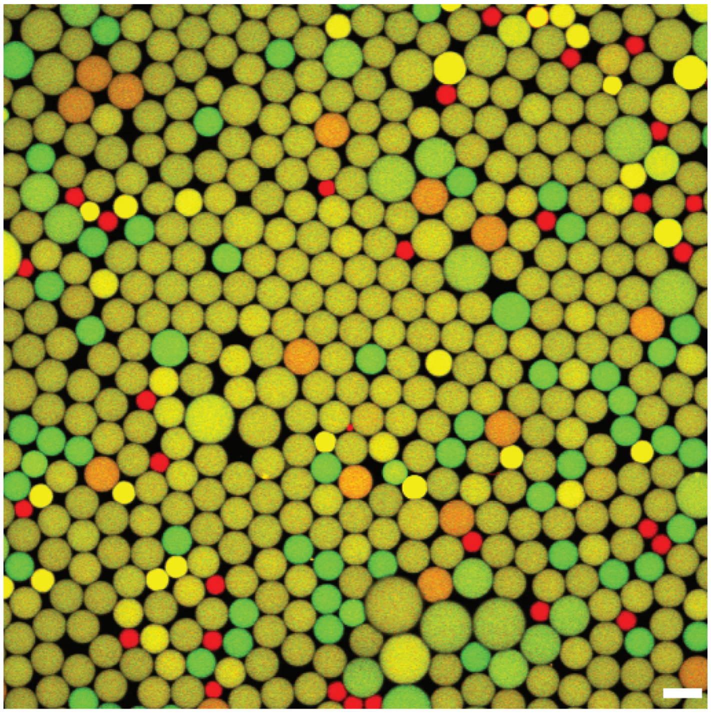

Figure 4.13: Droplets collected and imaged after paired coalescence using PFB. Droplets are imaged in red and green fluorescence and the color channels are overlaid to generate this image. Scale bar represents 50 μm.

Following analysis of fluorescence images similar to the example shown in Figure 4.13, we construct a two-dimensional histogram of the fluorescence intensities of the collected droplets. We plot red fluorescence intensity on the x-axis and green fluorescence intensity on the y-axis in Figure 4.14. From this plot, it is apparent that we have five subpopulations, labeled (A)-(E), contained within our analyzed droplets.

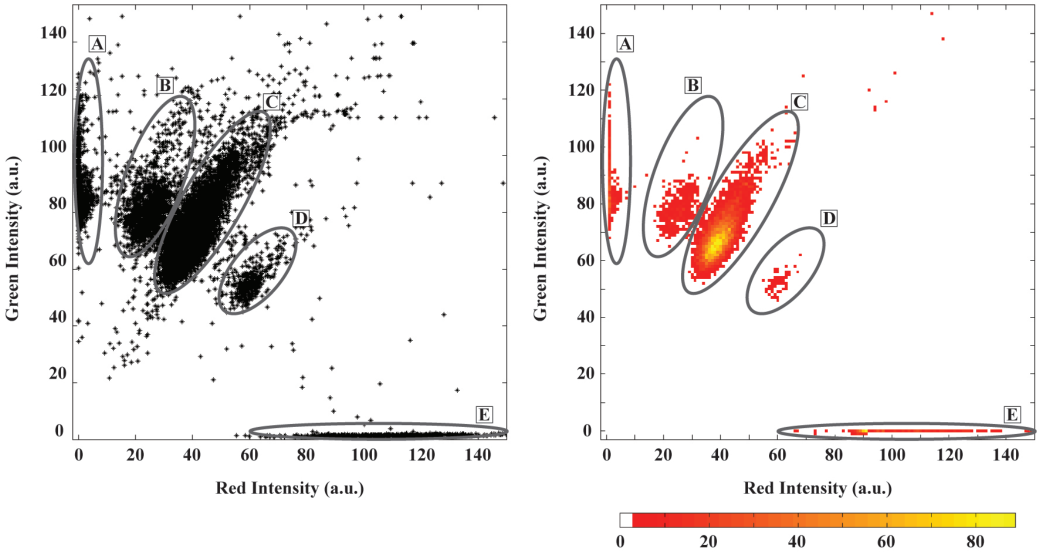

Figure 4.14: Two color raw data and two dimensional histogram of droplet fluorescence intensities. Five subpopulations are evident, labeled **(A)**-**(E)**. Total droplets plotted, $N = 15384$.

To determine the droplets from Figure 4.13 that correspond to the subpopulations in Figure 4.14, we select each subpopulation and generate an image of the droplets from Figure 4.13 that belong to it. These five images are displayed as the panels in Figure 4.15. The five subpopulations correspond to the following merged droplet ratios (expressed as [green]:[red]): (A) 1:0, (B) 2:1, (C) 1:1, (D) 1:2, and (E) 0:1. Table 4.1 shows the relative size of each subpopulation as a percentage of the total population. The subpopulation display and percentage establish that the desired ratio of one red to one green is the dominant coalescence occurring on the device.

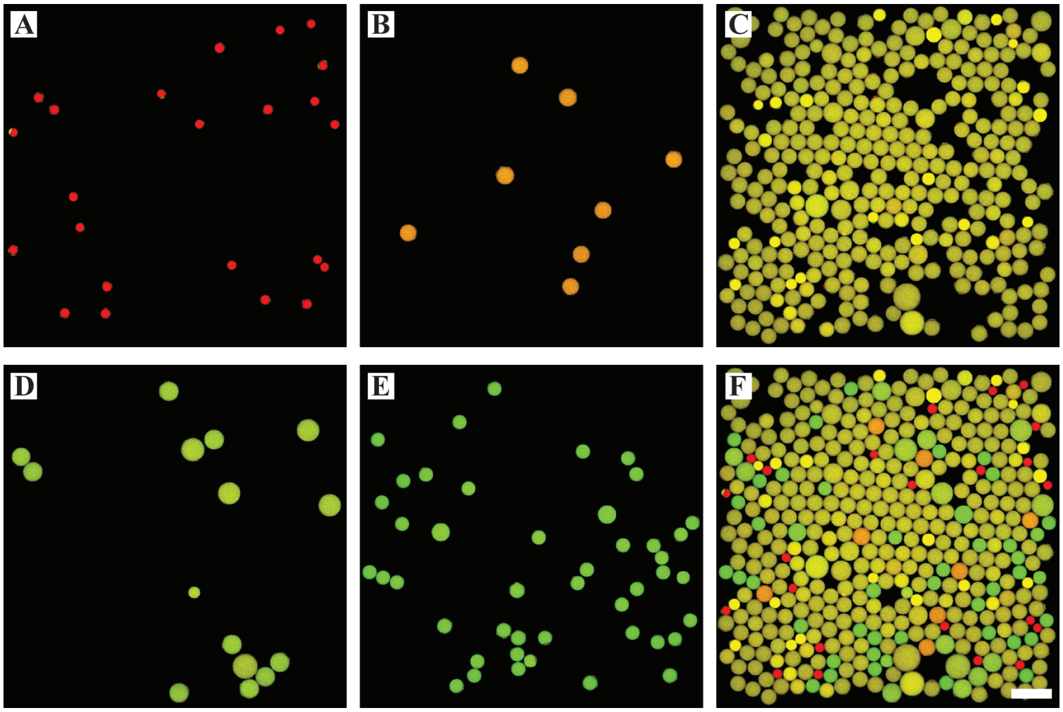

Figure 4.15: Images of droplets according to subpopulations defined in Figure 4.14. The subpopulations correspond to coalesced droplets with the following ratios of [green]:[red]: **(A)** 1:0, **(B)** 2:1, **(C)** 1:1, **(D)** 1:2, and **(E)** 0:1. A composite image overlaying all subpopulations is displayed in panel **(F)**. Scale bar represents 100 μm.

Table 4.1: Analysis of subpopulations contained with collected emulsion. The number of droplets belonging each subpopulation identified in Figure 4.14 is expressed as a percentage of the total number of droplets. The row marked "other" corresponds to droplets lying outside of the regions indicated by (A)-(E) on Figure 4.14.

Subpopulation	Percentage of Total Population
A	6%
B	2%
C	66%
D	10%
E	6%
other	10%

The final parameter we characterize is the size distribution of the collected droplets. The droplets corresponding to subpopulation (C) are selected and their radii measured. The histogram of these radii is shown in Figure 4.16. A dominant peak emerges at a radius of 21 μm, exactly what is expected for the radius of a droplet produced by the coalescence of a 40 μm diameter droplet with a 20 μm diameter droplet. We conclude that the coalescence device is behaving properly and predominately produces the 1:1 droplet coalescence for which it is designed.

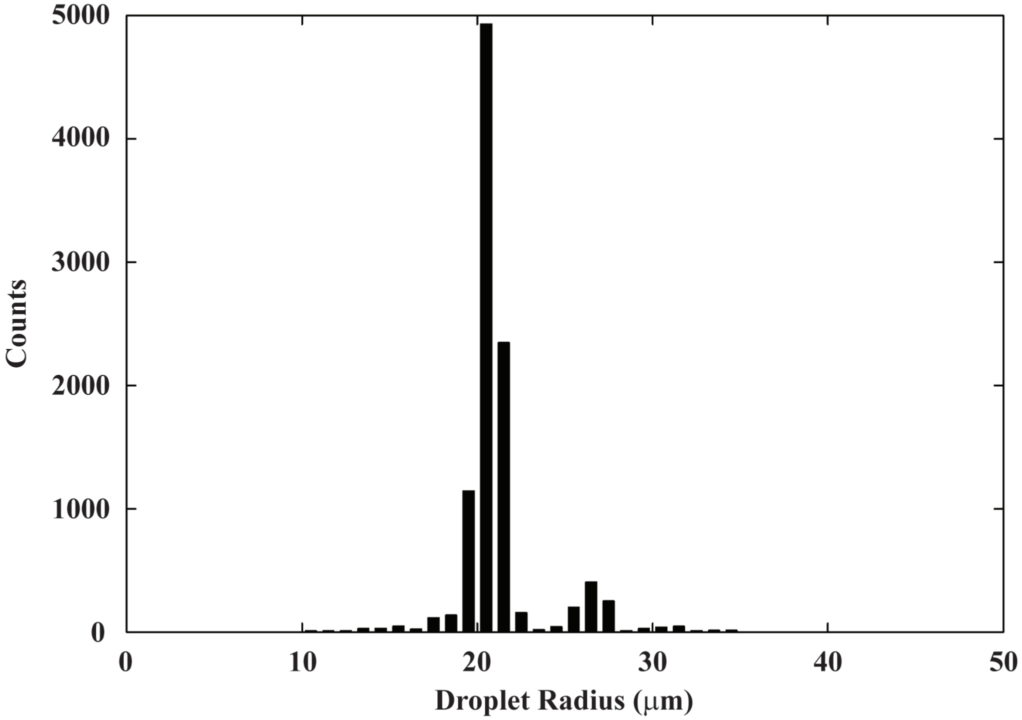

Figure 4.16: Histogram of droplet radii for droplets belonging to subpopulation (C), from Figures 4.14 and 4.15. The dominant peak corresponds to single pair coalescence events.

Though samples collected and imaged immediately after coalescence appear stable against additional coalescence, stability must be maintained over days for this device to be useful for microfluidic assay operations. The droplets collected for color analysis are stored in vials for an additional three days and samples removed at 24 and 72 hours. Images and two color histograms of the time points are shown in Figure 4.17. We observe that droplets remain stable over the course of 72 hours and the same five color ratio populations exist at all time points. Differences in the slopes and appearance of the subpopulations between Figures 4.17(D)-(F) are due to slight differences in the fluorescence imaging parameters, including the confocal microscope used, laser power, wavelength band recorded, and detector gain.

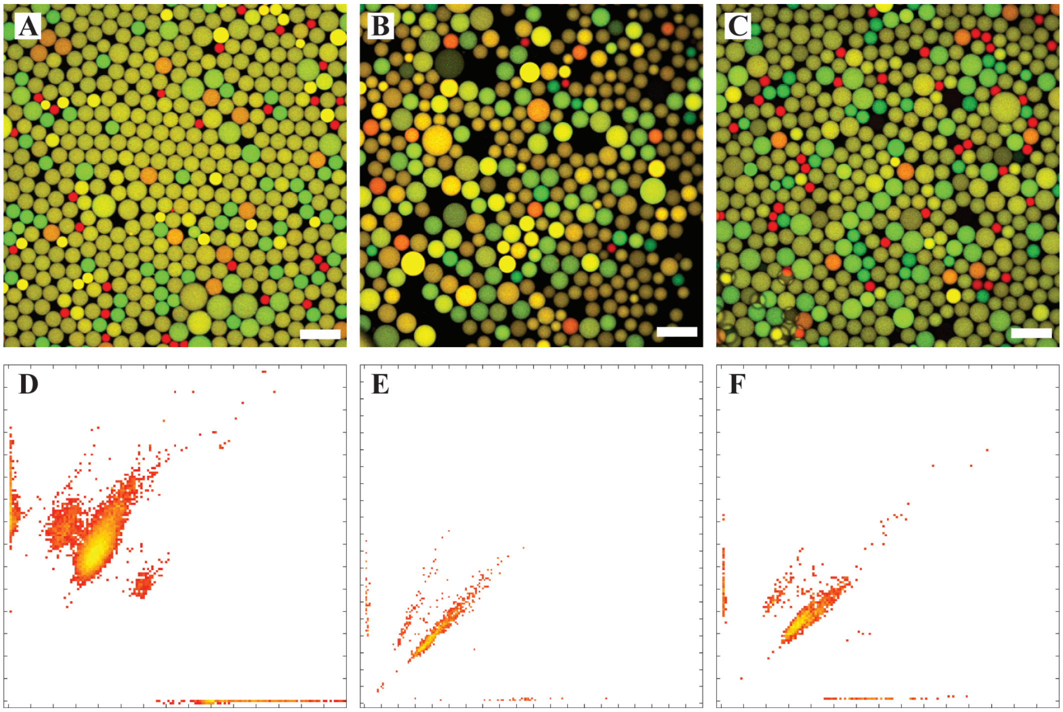

Figure 4.17: Stability of the collected emulsion. The top row of images are fluorescence images collected at the following time points: **(A)** 0 hours after paired coalescence; **(B)** 24 hours after paired coalescence; **(C)** 72 hours after paired coalescence. Scale bars represent 100 μm. The bottom row of images are green vs red histograms for images (A)-(C): **(D)** 0 hours after paired coalescence, $N = 15384$; **(E)** 24 hours after paired coalescence, $N = 2457$; **(F)** 72 hours after paired coalescence, $N = 2496$.

4.2.6 Mechanism Driving Passive Coalescence

Now that we have demonstrated proper function of the passive coalescence device, we explore the mechanism that leads to destabilization of the surfactant-coated droplet interface. There are two potential mechanisms for the source of droplet coalescence: 1) the PFB may remove the surfactant from the interface via precipitation or convective flow; or 2) the device geometry could cause coalescence by inducing a point of low pressure between paired droplets [100].

Since direct imaging of the surfactant flow at the interface is not possible for our microfluidic system, we use 2 μm colloids as tracer particles. The colloids are encapsulated into the aqueous droplets at the time of production. Upon reinjection of these droplets into our coalescence device, we observe that the colloids lie at the water/HFE-7500 interface, as seen in Figure 4.18. This is unexpected, as these electrosterically-stabilized particles should be extremely hydrophilic [124]. When these droplets interact with the PFB stream, a rapidly moving front of PFB engulfs the droplet and sweeps the colloids from the droplet interface within 3 msec, as seen in the sequence in Figure 4.18. This is even more unexpected, as in bulk tests, the colloids cannot be dispersed in either the HFE-7500 or PFB phases, even with surfactant present in the fluorinated phases. In addition, the spreading parameter for this system is negative, indicating that the PFB should not spontaneously wet the surfactant-coated interface.

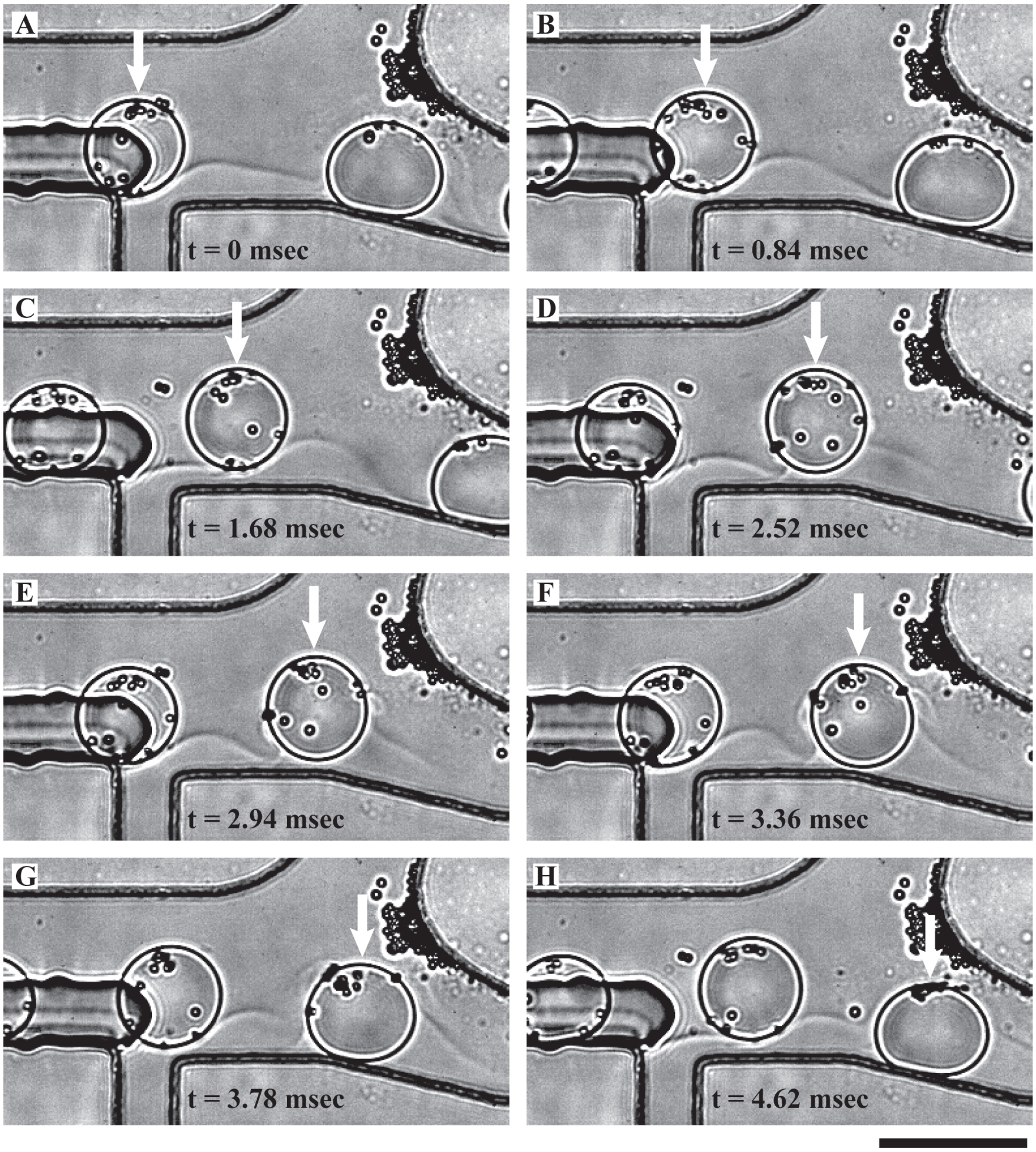

Figure 4.18: High speed image sequence of droplets coated with 2 μm colloids passing through the coalescence region of the microfluidic device with a perfusion flow of PFB. The PFB stream engulfs the droplet between panels (D) and (F). Scale bar represents 50 μm.

Though the colloid experiment indicates that PFB wetting causes convection at the droplet interface, bulk measurements of dynamic and equilibrium interfacial tensions yield two important observations about the surfactant on the droplet interface. First, from dynamic measurements, the characteristic time scale for the surfactant to adsorbed to and stabilize the interface is on the order of 5-10 seconds, seen in Figure 4.3. Second, from equilibrium interfacial tension measurements, a large decrease in interfacial tension upon surfactant addition, ~ 30 mN/m, is attributed to a large surface pressure supplied by the surfactant at the interface, implying that the surfactant is strongly adsorbed. From disparate timescales for the convective flow we see at the interface (3 msec) and the surfactant absorption dynamics (10 sec), as well as the known strong adsorption of the surfactant, we conclude that the PFB is not removing surfactant from the interface.

We also investigate whether the microfluidic device geometry alone is sufficient for droplet coalescence. Droplet pairs are flowed through the coalescence region of the device without a perfusion flow of PFB. The image sequence displayed in Figure 4.19 shows that droplet pairs pass through this region without coalescing. Thus, the device geometry is not the dominant force for coalescence. The PFB clearly affects droplet stability, but is not completely removing the surfactant from the interface. To determine the effect of PFB on the surfactant-coated interfaces, we take a closer look at the image sequences of droplets flowing through the coalescence region of the microfluidic device.

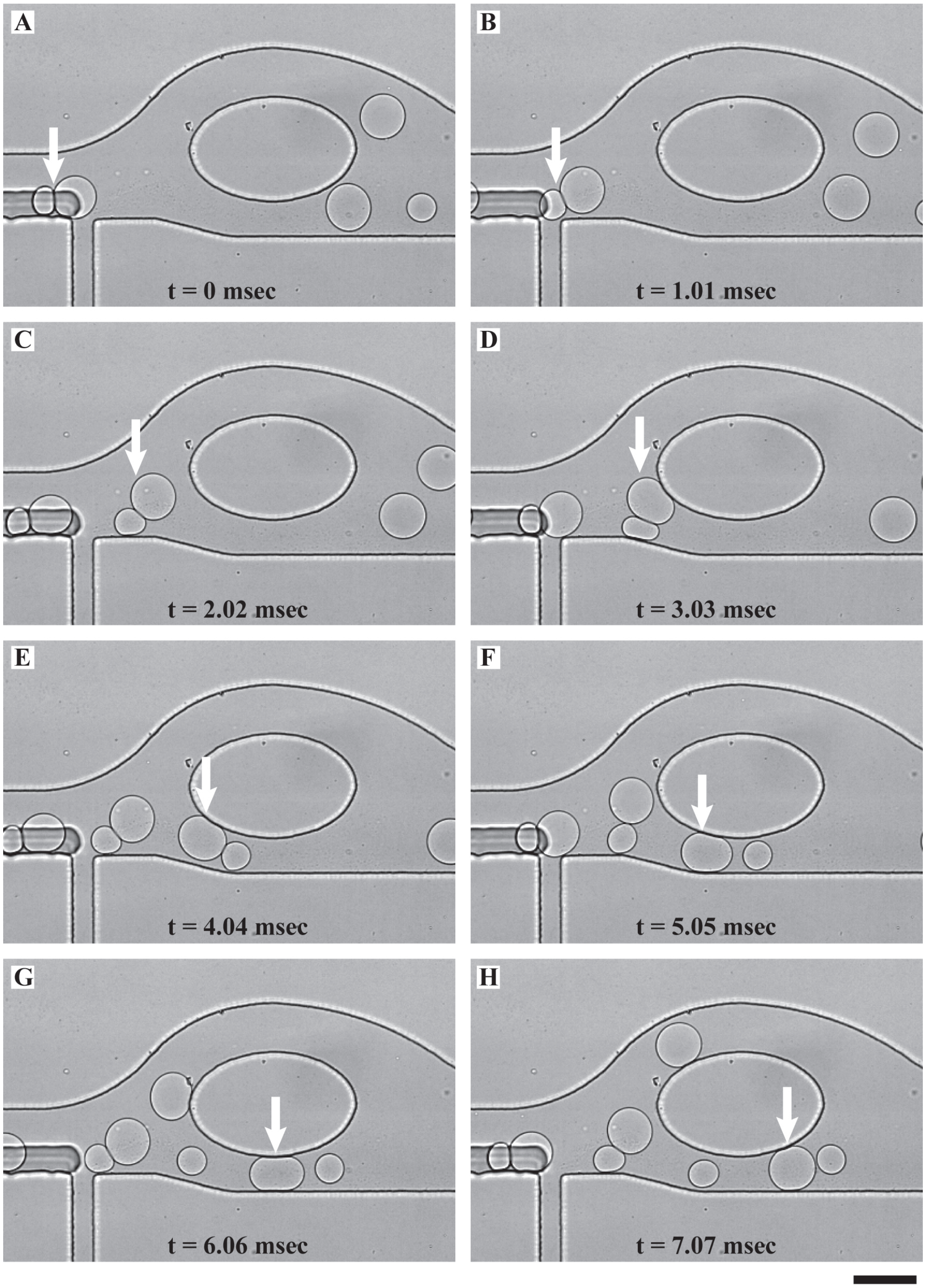

Figure 4.19: High speed image sequence of droplets passing through the coalescence region of the microfluidic device without a perfusion flow of PFB. Droplets flow through the constriction without coalescing. Scale bar represents 50 μm.

Comparing the image sequences of Figures 4.11, 4.18, and 4.19, we note an interesting behavior when the droplets interact with the PFB stream: the droplets are pulled into the PFB and appear to stick to the channel wall. This observation brings to mind work on adhesive water-in-oil emulsions [125], which demonstrates that the composition of the continuous phase can drive adhesion between surfactant-stabilized aqueous droplets. This adhesion requires surfactant-coated interfaces, allowing us to conclude that the surfactant remains on the interface of the droplets. In a continuous phase composed of a mixture of good and poor solvents for the surfactant, as the ratio between good and poor solvents is adjusted toward the poor solvent, the surfactant stabilized interfaces are driven into contact and become adhesive. These adhesive droplets are stable only in the absence of physical perturbations to the interface. The presence of any flow in the continuous phase is sufficient to cause the adhesive droplets to coalesce. Since we observe adhesion between surfactant coated interfaces (droplet to droplet, or droplet to channel wall), this is a plausible mechanism if the PFB proves to be a poor solvent for the triblock surfactant.

To check the solvency of the PFPE-PEG-PFPE surfactant in PFB, we prepare solutions of 2wt% surfactant in a series of HFE-7500 and PFB mixture ratios. Samples ranging from 0-90% PFB are shown in Figure 4.20(A). We observe that from 0% to 80% PFB, the solutions are clear and colorless. However, the 90% solution is turbid with a slight blueish cast, indicating that the surfactant has begun to precipitate out of solution. A second set of samples is prepared to investigate solutions of 80-90% PFB, shown in Figure 4.20(B). The onset of turbidity is at 85% PFB, thus the surfactant becomes insoluble in HFE-7500/PFB solutions containing $> 85\%$ PFB, and we expect droplets to display adhesive behavior in this range of PFB concentrations.

Figure 4.20: 1 mL sample solutions of 2wt% PFPE-PEG-PFPE triblock surfactant in mixtures of HFE-7500 and PFB. **(A)** Series of mixtures from 0% to 90% PFB. **(B)** Series of mixtures from 80% to 90%. The triblock surfactant begins to precipitate out of solutions composed of >85% PFB. Scale bar represents 1 cm.

We further characterize the adhesive nature of our droplets in HFE-7500/PFB solutions by directly imaging the adhesion and droplet shape using confocal microscopy. 40 μm diameter aqueous droplets containing FITC-conjugated dextran are collected into a vial containing 2wt% surfactant in pure HFE-7500. We fabricate imaging chambers as shown in the schematic in Figure 4.21. Droplets and alcohol-oil mixtures are pipetted into the chamber. Droplets in the chamber are buoyant and float up into contact with the surfactant and PDMS-coated coverslip. Recording XYZ image stacks of both the droplet fluorescence and the confocal reflectance signal allows us to recreate the droplet shape and determine the size of the adhesive patch between the droplet and PDMS. Signal from the confocal reflectance measurement relies on a spatially sharp (0.2 μm, approximately the confocal slice thickness) change in refractive index: adhesive droplets will produce black patches in the reflection signal similar to black spots in thin liquid films and foams.

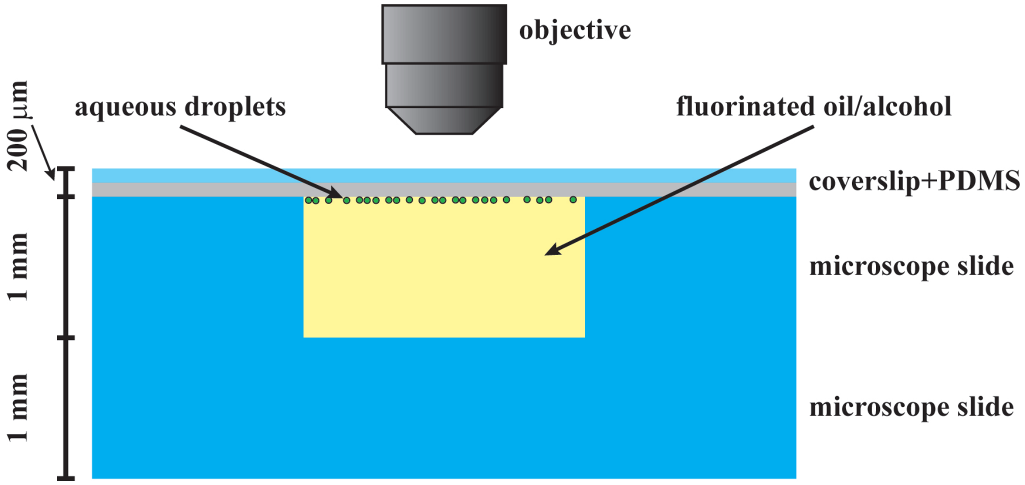

Figure 4.21: Cross section schematic of the sample chambers used for upright fluorescence confocal microscopy of adhesive aqueous droplets.

Overlay images of droplets and adhesion patches are shown in Figure 4.23, while energy of adhesion is plotted as a function of fluorinated alcohol concentration in Figure 4.24. We define the energy of adhesion [126, 125, 127]:

$$\Delta F = 2\gamma\,(1 - \cos(\theta)) \tag{4.3}$$

where the contact angle, θ, is calculated from the measured geometry of the droplets. If r is the radius of the adhesion patch between the droplet and the PDMS, and R is the radius of the droplet:

$$\theta = \sin^{-1}(r/R) \tag{4.4}$$

Given the interfacial tension values we measure and plot in Figure 4.22, we calculate the energy of adhesion for each concentration of fluorinated alcohol from size measurements of a droplet and it's adhesive patch.

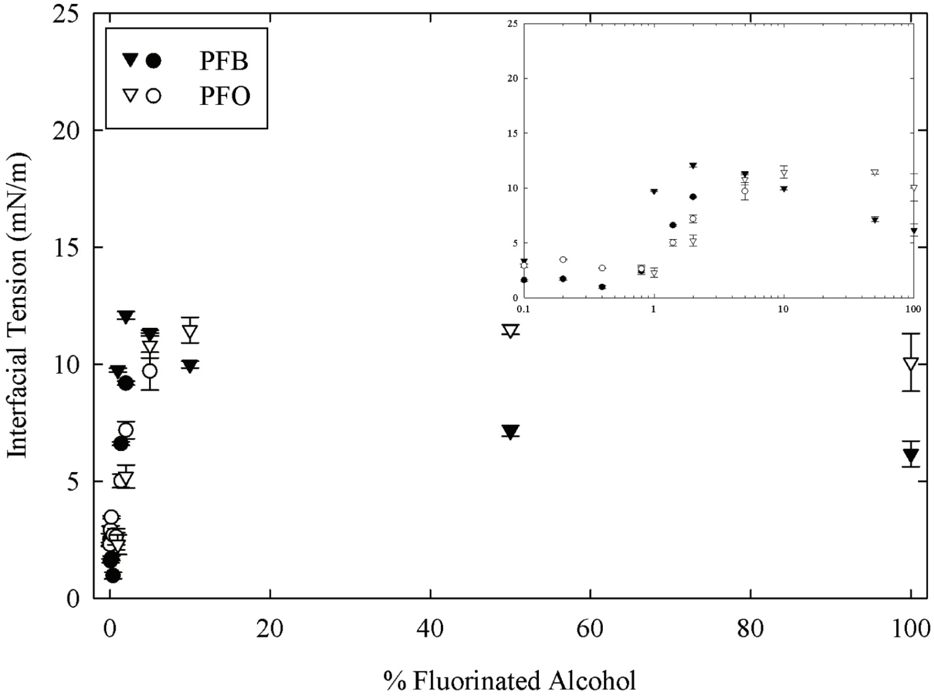

Figure 4.22: Equilibrium interfacial tension measurements. Data points plotted as circles are measured on a Du Nuoy ring tensiometer. Data points plotted as triangles are measured with a pendant drop tensiometer. All measurements are performed with 2wt% PFPE-PEG-PFPE surfactant in the continuous phase. Black data points correspond to measurements with perfluorinated butanol in the continuous phase, while white data points correspond to measurements with perfluorinated octanol in the continuous phase. Error bars represent the standard deviation of measurements.

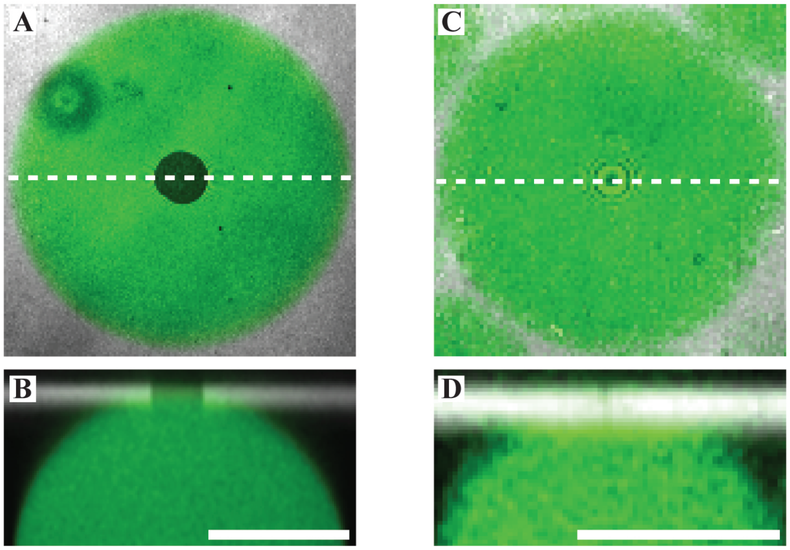

Figure 4.23: Profiles of droplets and adhesive patches reconstructed from 3D fluorescence confocal microscopy stacks. **(A)+(B)** XY and XZ profiles of droplets (green), adhesive patch (black), and reflectance at PDMS surface (white) for droplets in 50% PFB. **(C)+(D)** XY and XZ profiles of droplets (green), adhesive patch (black), and reflectance at PDMS surface (white) for droplets in 50% PFO. White dotted lines indicate plane of XZ slice shown in (B) and (D). Scale bars represent 50 μm.

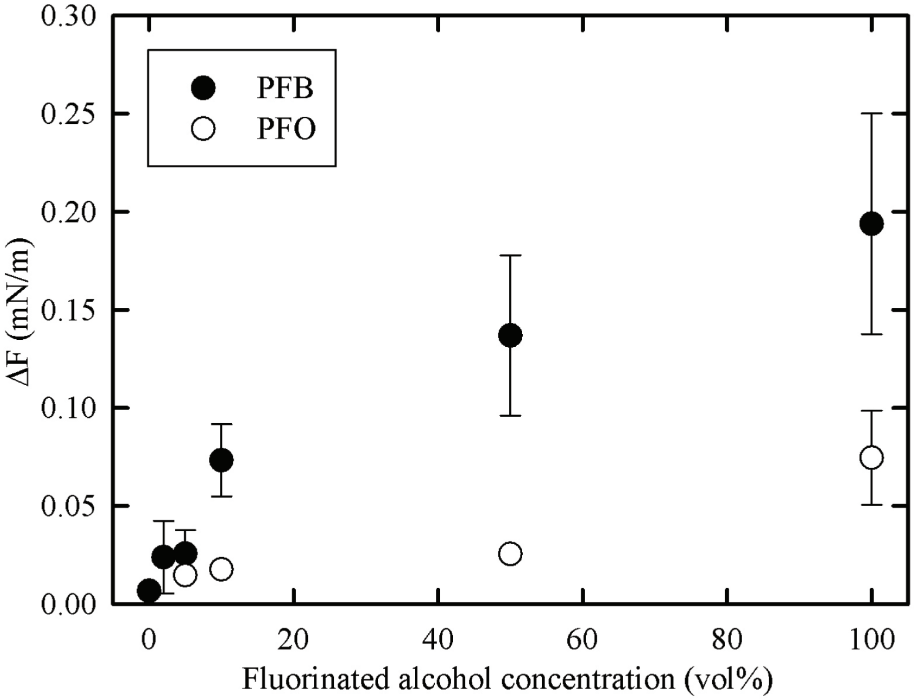

Figure 4.24: Plot of droplet adhesion energy, ΔF, determined from analysis of confocal microscopy sections.

Droplets immersed in solutions containing more than 2% PFB display adhesion to the surfactant-coated PDMS. While loading droplets into these samples, we observe coalescence within the imaging chamber. The droplet coalescence occurs while pipetting droplets and while they float to the PDMS surface, leading us to conclude that flow and droplet motion is sufficient to perturb the adhesive emulsions and cause coalescence. The 2% bulk concentration limit of PFB also agrees with operation of our microfluidic device: if the concentration of PFB in the collection channel or vial is above 1-2%, the droplets are unstable and we experience uncontrolled coalescence in the collected sample. We do not observe adhesion or coalescence between droplets immersed in PFO solutions. This leads us to hypothesize that PFO will not cause droplet coalescence when used in our microfluidic device.

As a final test of the mechanism, we perform negative control experiments. Since the insolubility of the surfactant in PFB is the parameter driving the coalescence, we perform tests of the microfluidic device using two additional fluids for the perfusion phase: perfluorinated octanol (PFO) and HFE-7500. Both of these fluids are good solvents for the surfactant. The results of using each fluid as the perfusion phase are compared to the results for using PFB. Images of the microfluidic device in operation are shown in Figure 4.25. Fluorescence images of the emulsion collected from each trial are shown in Figure 4.26. Finally, the two-color histograms for the collected emulsions are plotted in Figure 4.27.

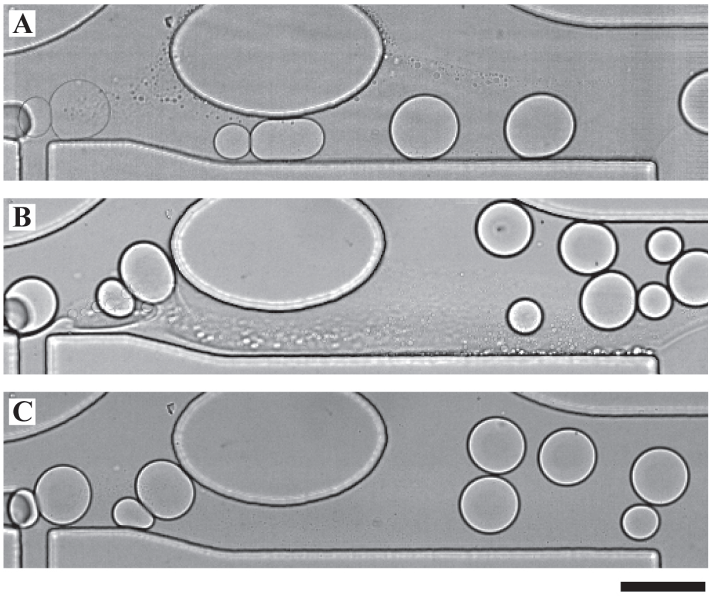

Figure 4.25: Images of droplet behavior within the chemical coalescence microfluidic channel for three different perfusion phases. **(A)** Positive control with PFB as the perfusion phase. **(B)** Negative control with PFO as the perfusion phase. **(C)** Negative control with HFE-7500 as the perfusion phase. Scale bars represent 50 μm.

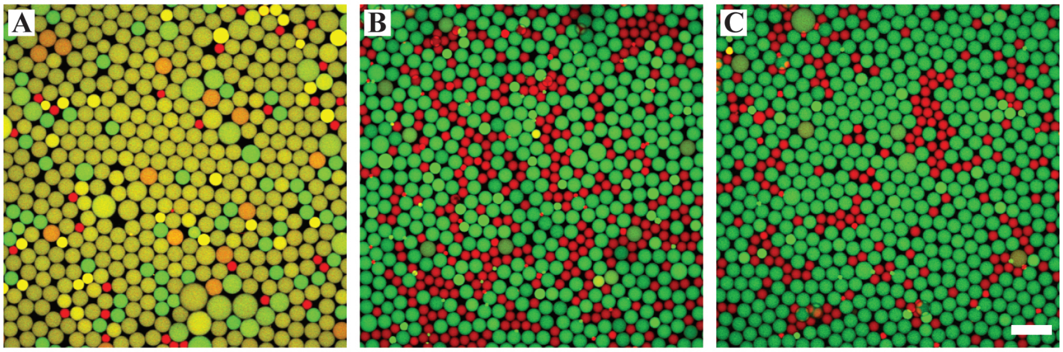

Figure 4.26: Fluorescence images of collected droplet populations from three experiments with the chemical coalescence microfluidic device. **(A)** Positive control with PFB as the perfusion phase. **(B)** Negative control with PFO as the perfusion phase. **(C)** Negative control with HFE-7500 as the perfusion phase. Minimal coalescence is observed when using PFO or HFE-7500. Scale bars represent 100 μm.

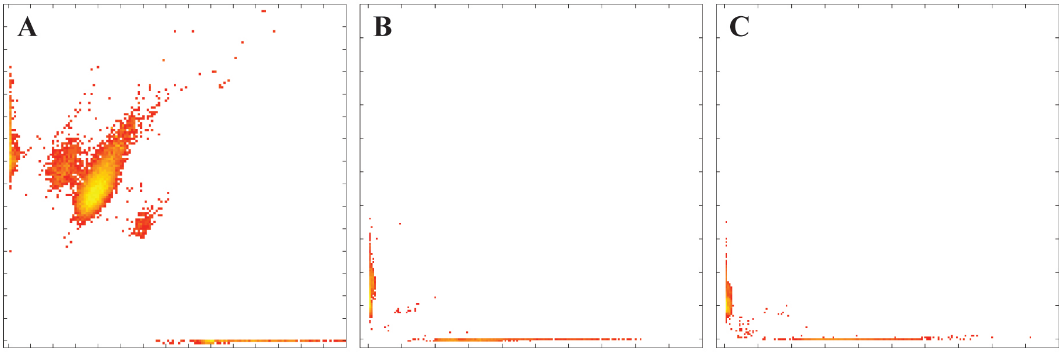

Figure 4.27: Two color histograms of fluorescence intensity of collected droplet populations from three experiments with the chemical coalescence microfluidic device. Red fluorescence intensity is plotted on the x-axis and green fluorescence intensity is plotted on the y-axis. **(A)** Positive control with PFB as the perfusion phase. **(B)** Negative control with PFO as the perfusion phase. **(C)** Negative control with HFE-7500 as the perfusion phase.

As expected, neither PFO or HFE-7500 cause coalescence of droplet pairs on-chip, as shown in Figure 4.25. Analyzing the collected emulsion, we see very few coalescence events, and instead observe a split population in the histograms shown in Figure 4.27(B)+(C): collected droplets are either entirely green or entirely red, indicating no coalescence has occurred.

In summary, we have demonstrated controlled coalescence of surfactant-stabilized emulsion droplets by employing perfusion of a poor solvent for the surfactant. As droplets are brought into contact with this poor solvent, the surfactant-coated interfaces become adhesive and exclude solvent from between the droplets. Flow of the continuous phase cause perturbations to this thin, adhesive interface and nucleates a pore through the interface. Once this pore has been nucleated, the droplets spontaneously coalesce. This new, larger droplet is restabilized by addition of fresh surfactant and dilution of the poor solvent, allowing collection of the droplets off-chip for additional sample processing.

Chapter 5

Microfluidics as an Analytical Screening Tool

The analysis of individual droplets requires a sensitive measurement to determine what has occurred in each droplet. This information may the final data of an experiment, similar to flow cytometry, or it may be used to sort a sub-population of droplets away from the main population, similar to fluorescence-activated cell sorting (FACS). The data may consist of fluorescence measurements [33, 28, 19], image processing of features within the droplet [35], or electrical measurements [128]. As many biological system of interest already have bulk assays developed for fluorescent readout of enzyme activity, protein production, or antibody affinity, we adapt these for use in droplets and design a droplet detection and sorting device that measures the fluorescence intensity of individual droplets.

5.1 Detection of Droplets

The primary advantage of performing assays in droplets is the ability to access large numbers of samples while keeping expressed products physically associated with the cell that produces them. Measuring results requires inclusion of assay components and barcodes in the droplets at the time of encapsulation or addition to the droplets later [33, 28, 88, 129].

As detailed in Section 2.2, the assay results are recorded by measuring the fluorescence intensity of each droplet. Focusing the excitation laser to a small spot limits the fluorescence signal to a particular droplet and we design a fluidic channel that forces droplets to pass this point serially.

Droplets are flowed into the detection channel at high volume fraction. The droplets pass through a constriction that forces them into a single-file line, as seen in Figure 5.1(A). After this constriction, an inlet adds oil to space the droplets. Each droplet needs to have sufficient separation from its neighbors such that fluorescence of one droplet does not contribute to the measurement of the next droplet. Downstream of the spacer oil, the droplets pass through a straight channel where detection of the assay state is performed. A plot of the fluorescence intensity of two droplets is shown in Figure 5.1(B). From this data, we extract average intensity, peak intensity, and droplet duration.

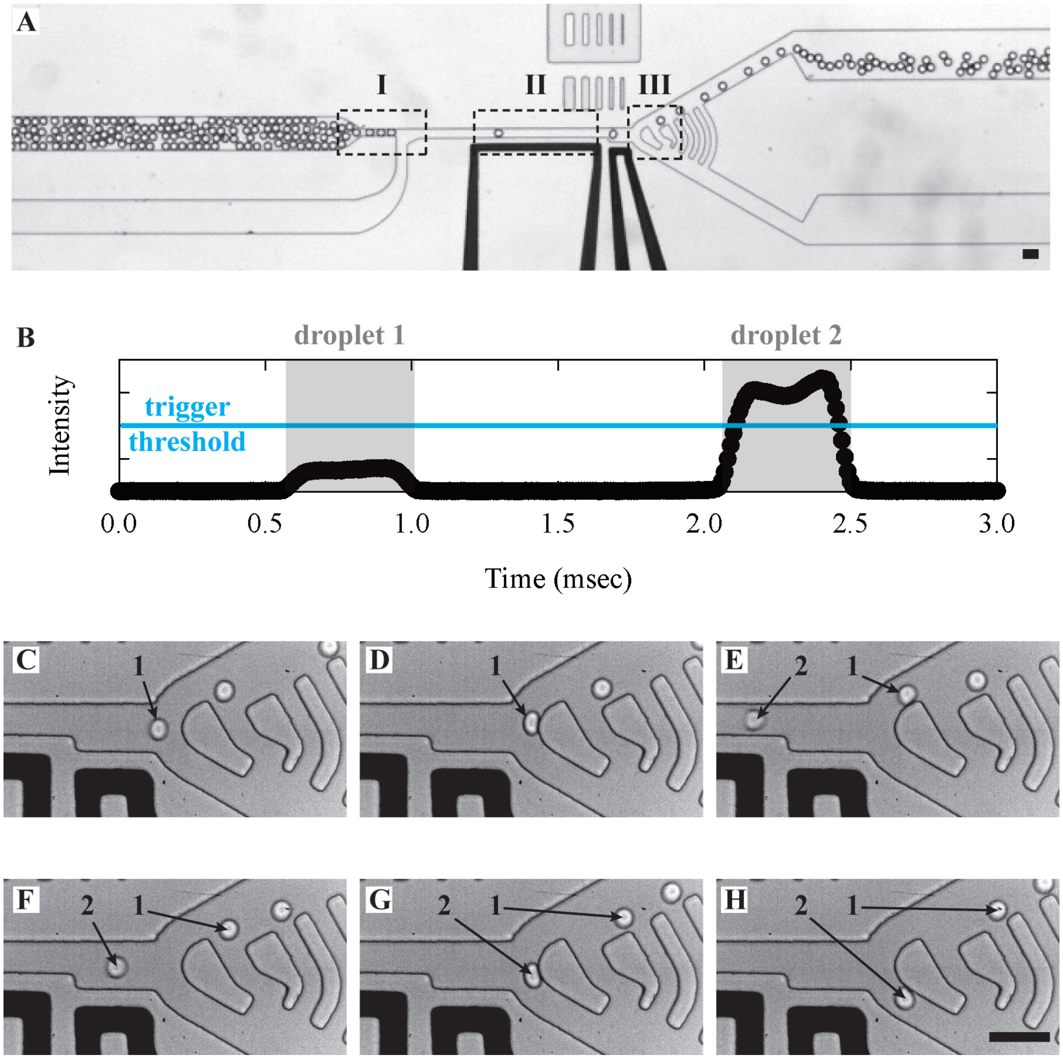

Figure 5.1: **(A)** Overview of the microfluidic droplet detection and sorting channel. Droplets flow left to right and are spaced by addition of oil in region I. Excitation and collection of fluorescence is performed in region II. In region III, the microfluidic channel splits into two legs: the upper channel is the channel that flows droplets to waste, and the lower channel is the channel that flows droplets to keep for further processing. The black objects are electrodes for steering the droplets via dielectrophoresis. **(B)** Fluorescence intensity vs time for two droplets. A triggering threshold is set between the average intensities of the two droplets. **(C)-(H)** Time series of the microfluidic droplet sorter function. Numbers denote droplets depicted in (B). Scale bars represent 50 μm.

5.2 Sorting of Droplets

While simple detection of droplet-based assays may be sufficient for some applications, often the contents of the droplets must be recovered for further processing or analysis. This requires a droplet actuator that uses the detection data to remove particular droplets from the primary population.

Since manual selection of a single droplet from the population is challenging and would decimate throughput rates of the microfluidic system, droplet sorting has evolved to be an automated process that steers a droplet of interest away from its neighbors. To maintain a processing stream with reasonable throughput, this selection process uses a flow channel with a single inlet and two outlets. After the detection zone described in Section 5.1, the channel bifurcates. Each of the bifurcation legs heads toward one of the outlets, splitting the initial population into two subpopulations. Energizing the electrodes seen in Figure 5.1(A) imparts a dielectrophoretic force to the droplets, pulling droplets to be saved into the channel nearest the electrode, while the other droplets flow down the opposite arm of the Y. This process is seen for two droplets in the image sequence of Figure 5.1(D)-(H).

After the sorting stage, droplets must be collected off-chip. Often, additional sample characterization must be performed on the sorted sample; this includes breaking the emulsion to form a single aqueous phase, DNA amplification, or sequencing [130]. The two sorting outlets can be connected to 1.5 mL microcentrifuge tubes using polyethylene (PE) or polyetheretherketone (PEEK) tubing. Short term sample collection may also be performed by sticking gel loading pipette tips into the outlet ports.

5.2.1 Sorting Channel Design

The fluidic channel is designed for a majority of the flow to pass into one of the bifurcation legs. The droplets follow this majority of the flow in the absence of external forces. The split in flow is achieved by fabricating channels with different hydraulic resistances. The hydraulic resistance of a rectangular cross section channel is [83]:

$$R_{hyd} = \frac{12\eta L}{1 - 0.63(h/w)} \frac{1}{h^3 w} \tag{5.1}$$

where η is the dynamic viscosity, L is the channel length, h is the channel height, and w is the channel width. This assumes that $h \ll w$. Should the height and width be roughly the same dimension, then it is more appropriate to use the expression for the resistance of a square cross section channel [83]:

$$R_{hyd} = \frac{28.4\eta L}{h^4} \tag{5.2}$$

To achieve the required flow splitting at the sorting bifurcation, the channels are kept constant in height and width, but one channel is designed with a length of 42 μm, while the other is 82 μm. This results in a resistance ratio of 1:1.95 and splits the flow with roughly 67% heading down the shorter, lower resistance leg and the remaining 33% flowing into the longer leg. To ensure that these channel dimensions determine the flow partitioning at the bifurcation, the two exit legs are connected to one another by a series of shunt channels. The shunts allow exchange of continuous phase between the two exit legs and prevent backflow or differences in pressure from affecting the division of fluid at the bifurcation [33]. Verification of the flow partitioning is shown in Figure 5.2.

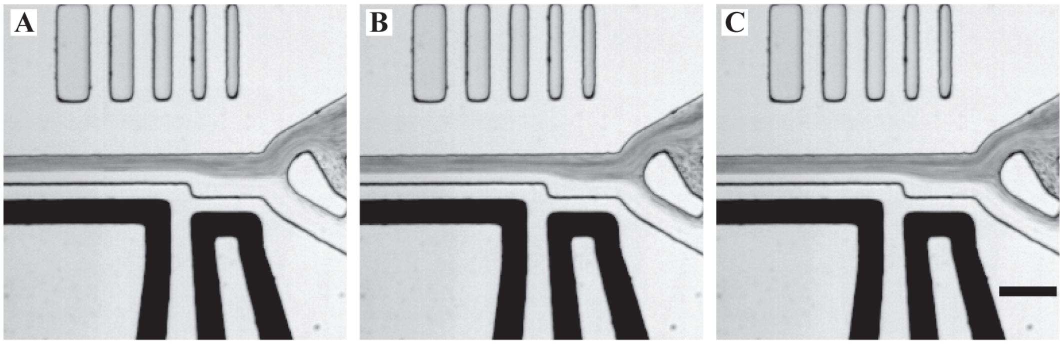

Figure 5.2: Illustration of continuous phase flow partitioning at the sorting junction. Images correspond to the following dark:light flow rate ratios: **(A)** 6:4, **(B)** 6.67:3.33, **(C)** 7:3. As expected, roughly 66% of the fluid entering the sorting junction flows into the upper leg. Scale bar represents 50 μm.

Since the droplets are carried along by the continuous phase, they follow the majority of continuous phase flow at any point in the channel. When a droplet encounters the bifurcation, it follows the majority of the flow into the shorter, lower resistance exit leg [2]. Thus, the default state of the bifurcation is to divert all incoming droplets to the low resistance exit. The higher resistance exit is used for drops of interest.

The amount of time required for one droplet to transit the bifurcation determines the minimum spacing between droplets. If one droplet does not exit this key section before the next droplet arrives, the increased resistance due to the first droplet changes the flow-splitting ratio and forces the second droplet to flow into the arm opposite the one containing the first droplet.

5.2.2 Droplet Actuation Using Dielectrophoresis

To steer a droplet into the higher resistance channel, a force must be applied to the droplet. This is accomplished via dielectrophoretic manipulation of the droplets [33, 131].

For the simple case of pure water droplets suspended in a continuous phase of oil, we consider each of the liquid components as a linear dielectric material. The application of an external electric field, $\mathbf{E}_0$, will cause these materials to become polarized with a dipole moment, $\mathbf{p}$, such that $\mathbf{p} =\propto \mathbf{E}_0$. For a spherical particle of radius a, and relative permittivity ϵ_P, the induced dipole moment is [132, 133, 134, 135]:

$$\mathbf{p} = 4\pi\epsilon_0 a^3 \left(\frac{\epsilon_P - \epsilon_M}{\epsilon_P + 2\epsilon_M}\right) \mathbf{E}_0 \tag{5.3}$$

where ϵ_0 is the permittivity of free space, and ϵ_M is the relative permittivity of the medium surrounding the particle.

For aqueous droplets in oil, the droplet is the particle and the oil is the surrounding medium. The droplet dipole experiences a force due to the external field:

$$\mathbf{F}_{DEP} = (\mathbf{p} \cdot \boldsymbol{\nabla})\, \mathbf{E}_0 \tag{5.4}$$

Combining Equations 5.3 and 5.4, we find the force on the dipole is:

$$\mathbf{F}_{DEP} = 2\pi a^3 \epsilon_M \left[\frac{\epsilon_P - \epsilon_M}{\epsilon_P + 2\epsilon_M}\right] \boldsymbol{\nabla} E_0^2 \tag{5.5}$$

This force causes motion of the dipole along the gradient, $\boldsymbol{\nabla} E_0^2$, a process known as dielectrophoresis (DEP). The dimensionless quantity enclosed in square brackets is the Classius-Mosotti factor, K. Equation 5.5 considers the force on a dipole in a static electric field. Should the applied external field be an oscillating AC field with angular frequency, ω, a few corrections must be made to the Equations 5.3-5.5. $\mathbf{E}_0$ is now $\mathbf{E}_0(\mathbf{x}, t) = \mathbf{E}_0(\mathbf{x})(\cos(\omega t) + i \sin(\omega t))$. We also introduce the complex permittivities of the droplet and medium, $\tilde{\epsilon}_P$ and $\tilde{\epsilon}_M$.

$$\tilde{\epsilon}_P = \epsilon_0\epsilon_P - \frac{i\sigma_P}{\omega} \qquad\qquad \tilde{\epsilon}_M = \epsilon_0\epsilon_M - \frac{i\sigma_M}{\omega} \tag{5.6}$$

where σ_P and σ_M are the conductivities of the droplet and medium, respectively. Substituting these values into Equation 5.4 and time-averaging the result, we find the time-average DEP force on a lossy, dielectric sphere in a an oscillating electric field to be:

$$\langle \mathbf{F}_{DEP} \rangle = 2\pi a^3 \epsilon_M \,\mathrm{Re}\left[\frac{\tilde{\epsilon_P} - \tilde{\epsilon_M}}{\tilde{\epsilon_P} + 2\tilde{\epsilon_M}}\right] \boldsymbol{\nabla} E_0^2 \tag{5.7}$$

with K^*, the complex Classius-Mosotti factor

$$K^* = \left[\frac{\tilde{\epsilon_P} - \tilde{\epsilon_M}}{\tilde{\epsilon_P} + 2\tilde{\epsilon_M}}\right] \tag{5.8}$$

For water droplets in oil and for frequencies of DC to MHz, $\mathrm{Re}\,[K^*] = 1$ [131]. Since the droplet sorting devices operate in this range, Equation 5.7 simplifies to:

$$\langle \mathbf{F}_{DEP} \rangle = 2\pi a^3 \epsilon_M \boldsymbol{\nabla} E_0^2 \tag{5.9}$$

We see that the force on a droplet is a function of its size, the permittivity of the continuous phase, and the gradient of the square of the E-field.

5.2.3 E-field Gradient Characterization

Fast, efficient droplet sorting will be achieved when a strong force is applied to the droplet volume for an extended section of channel, drawing the droplet out of the majority flow and directing it down the sorted droplet exit channel. According to Equation 5.9, the dielectrophoretic force imparted to polarized droplets can be maximized by adjusting the droplet size, the medium surrounding the droplets, or the gradient of E_0^2. Experimental constraints dictate a droplet size and fluid material properties, so to maximize F_{DEP}, we must optimize the gradient of E_0^2. In the case of droplet sorting, the geometry of the microfluidic channel and electrodes used to apply the electric field define this gradient.

We optimize droplet sorting with DEP by comparing different electrode geometries, shown in Figure 5.3. The geometries shown below are tested using identical populations of aqueous water droplets in fluorocarbon oil. By analyzing high speed image sequences, we characterize the performance of each electrode geometry for sorting.

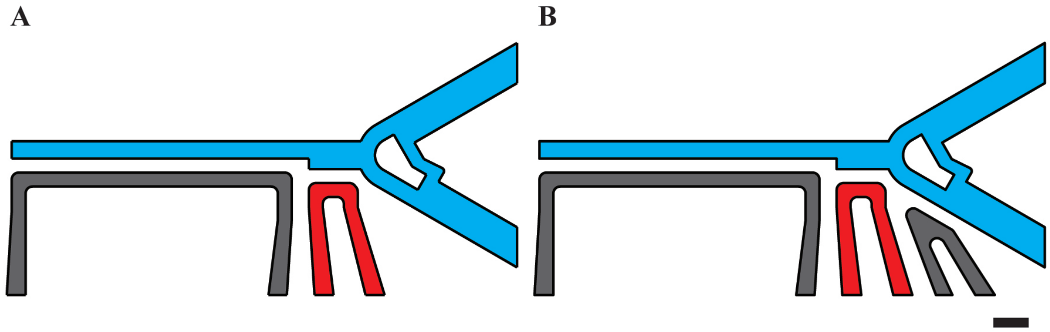

Figure 5.3: Illustrations of electrode geometries for droplet sorting: **(A)** two electrodes, and **(B)** three electrodes. For clarity, only the electrodes and bifurcation region of the designs are shown. The microfluidic channel is shown in blue, the ground electrode(s) in gray, and the positive electrode in red. Scale bar represents 50 μm.

We define a droplet sorting ratio, $S = \frac{n_S}{N}$, where n_S is the number of droplets passing into the sort exit channel and N is the total number of observed droplets. Plotting this value as a function of applied voltage allows us to determine the applied potential at which all droplets are pulled into the sort exit channel. This characterizes the potential at which F_{DEP} becomes the dominant force on droplet motion. At this value, differences in flow and fluidic resistance caused by preceding droplets no longer influence the path of a given droplet.

A device design with a better gradient shape should require a lower applied potential to achieve dominant force on the droplets. We expect the triple electrode design shown in Figure 5.3 to have a more favorable gradient than the two electrode design, and thus actuate 100% of the droplets at a lower applied voltage than the two electrode design. We also expect the triple electrode design to deform droplets from spherical when they are in the exit channel.

Figure 5.4 plots the results of the applied potential tests. We see a clear difference between the two electrode geometries, with the three electrode design beginning to pull droplets into the sort exit channel at voltages nearly 200 V less than the two electrode design. The three electrode design also achieves 100% sorting at 75 V less than the two electrode geometry. This characterization agrees with our initial expectations for device performance.

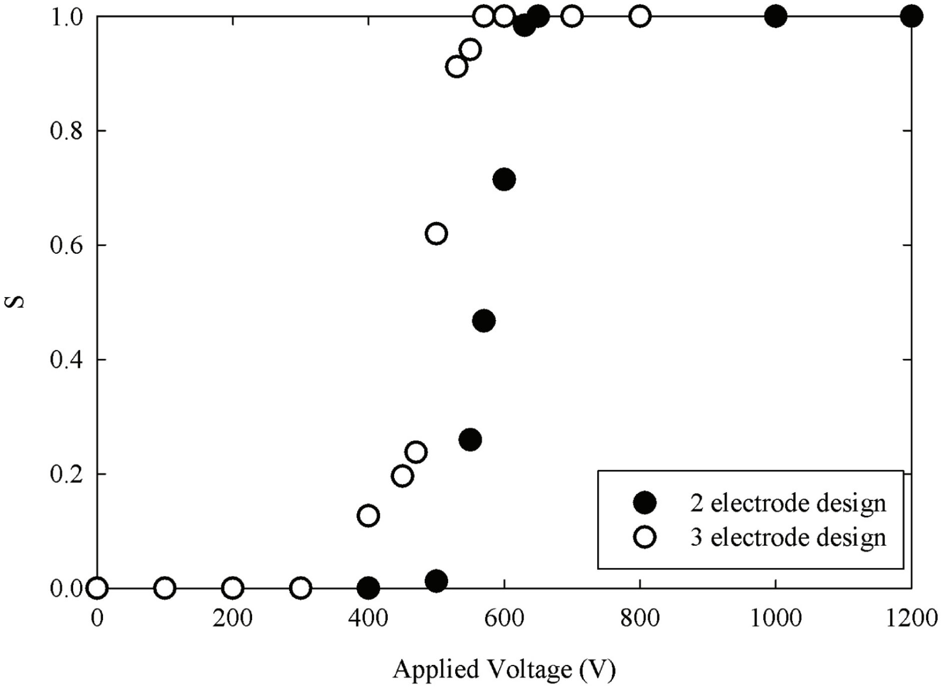

Figure 5.4: Percentage of droplets actuated as a function of applied voltage. The three electrode design is able to actuate 100% of the droplets at a lower applied voltage than the two electrode design

Looking at images of the devices in operation, shown in Figure 5.5, our second expectation is also confirmed. The three electrode device deforms incoming droplets from spherical at 600 V. At 700 V, the device deforms droplets in the exit channel, and at 1000 V, there is uncontrolled electrowetting and coalescence of droplets caused by massive droplet deformation and strong F_{DEP}. By contrast, the two electrode device begins to cause deformation of incoming droplets at 800 V, deformation of droplets in the exit channel at 1000 V, and never causes electrowetting or uncontrolled coalescence at the sorting bifurcation.

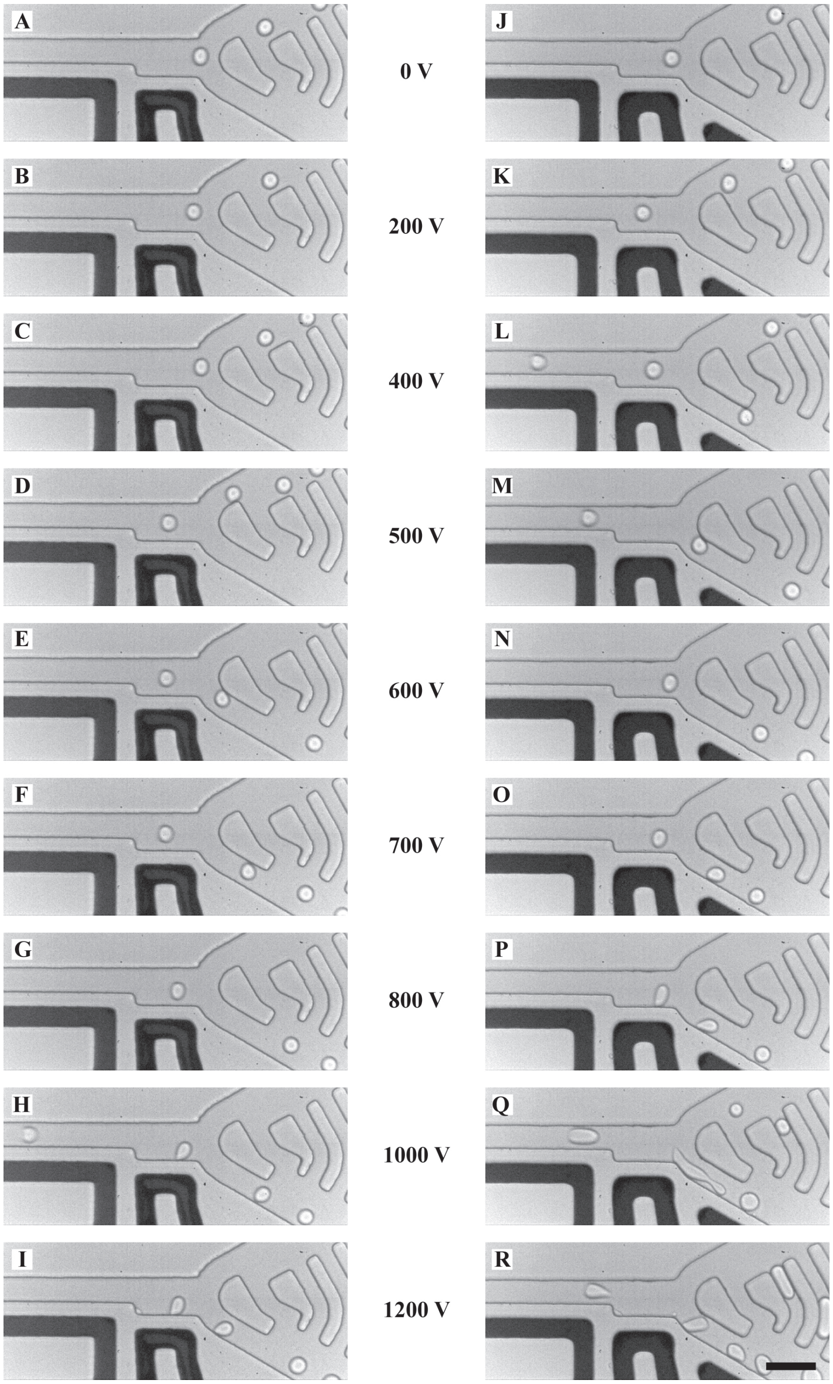

Figure 5.5: Images of droplet actuation by two and three electrode designs for a range of applied voltages. Scale bar represents 50 μm.

5.2.4 Modeling of Electrode Geometries

To better understand the performance results discussed in Section 5.2.3, we model the electric field gradients generated by the electrode designs. Three dimensional finite element simulations of the designs are performed in COMSOL. Since we are interested in understanding the basic field gradient, we simplify the model by applying an equilibrium DC field and exclude perturbations to the field caused by the presence of a droplet.

We model only the portion of the devices nearest the electrodes. The channel is given the properties of fluorocarbon oil FC-40, while the electrodes are copper, and the surrounding medium is a PDMS slab which fully encloses the fluidic channel and electrode objects. The left electrode is set to ground, while a potential of 750 V is applied to the right electrode. As noted above, the full 3D solution is calculated, but for clarity we simply plot the magnitude of $\boldsymbol{\nabla} E_0^2$ in the center plane of the fluidic channel.

The three electrode device is designed with a second ground electrode to the right of energized electrode. This new electrode is offset from the energized electrode to avoid interference with the fluidic channel. This electrode is intended to extend the region of high $\boldsymbol{\nabla} E_0^2$ into the save channel, thereby continuing to actuate the drop even after it has passed the initial portion of the expansion. We see exactly this gradient shape in the plot shown in Figure 5.7.

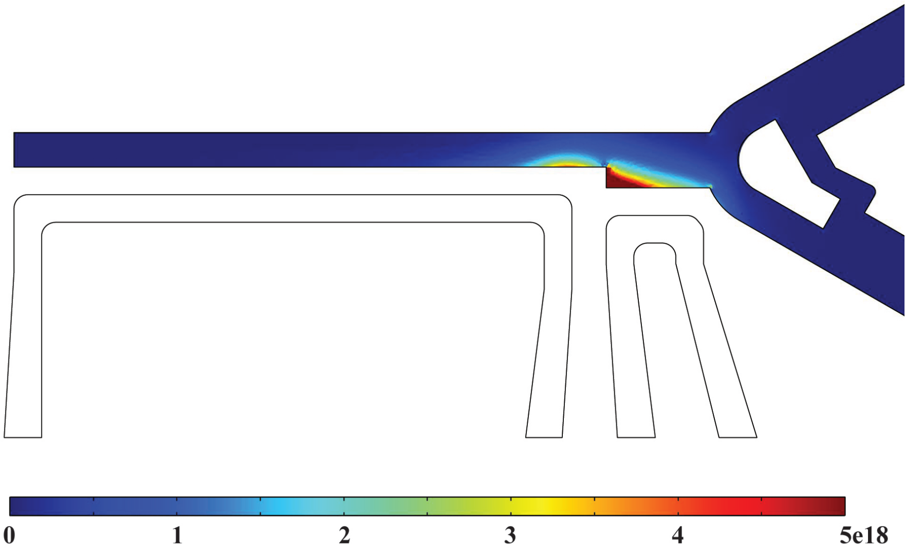

Figure 5.6: Plot of ∇E_0^2 derived from a three dimensional steady-state COMSOL simulation of the two electrode design. Results are shown only within the microfluidic channel. Units are $\mathrm{m{\cdot}kg^2/(s^6A^2)}$.

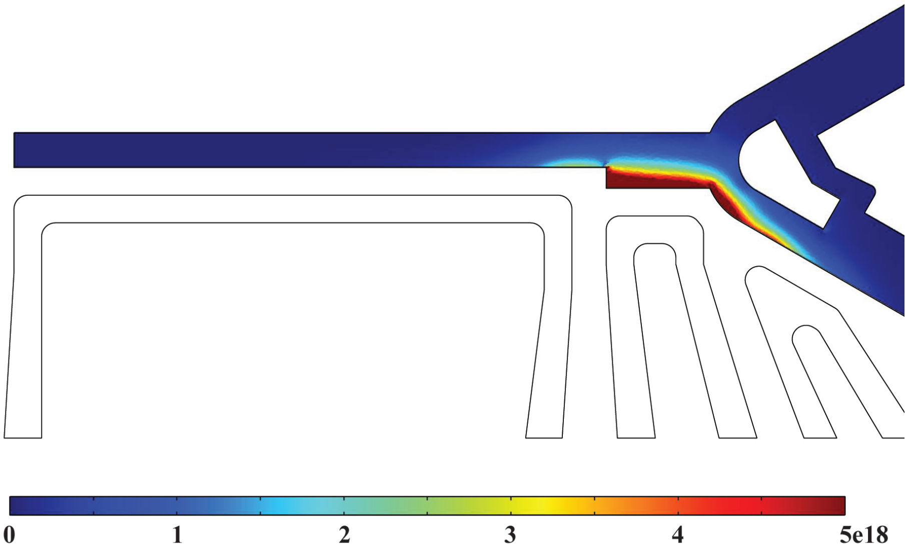

Figure 5.7: Plot of ∇E_0^2 derived from a three dimensional steady-state COMSOL simulation of the three electrode design. Results are shown only within the microfluidic channel. Units are $\mathrm{m{\cdot}kg^2/(s^6A^2)}$.

The addition of the second ground electrode extends the range of high ∇E_0^2, prolonging the exposure of passing droplets to a strong dielectrophoretic force pulling them toward the save channel. This enables sorting with lower voltages and continues to pull the droplets even after they have entered the save leg of the bifurcation.

5.2.5 Sorting Device Design Rules

The experimental and computational results lead to several design considerations for ensuring robust, efficient sorting via dielectrophoresis. First, the fluidic channel must expand wider than the diameter of a droplet, allowing the droplet to be pulled laterally into the fluid streamlines that pass into the higher resistance exit channel. This expansion must be long enough to allow sufficient time for the droplet to be pulled laterally. Second, in the expansion region of the inlet channel, the magnitude of $\boldsymbol{\nabla} E_0^2$ must be high and extend along one sidewall for the entire length of the expansion. Extension of the high gradient along the expansion ensures that a passing droplet encounters a continual force toward the electrodes. Finally, there should be little to no gradient in the inlet channel as it passes the first electrode. This ensures that only the droplet at the bifurcation will be affected by the applied electrical pulses.

We also verify that device fabrication errors do not impact ∇E_0^2. Due to the resolution limits of contact lithography with printed photomasks, channel structures are created with minimum features of $8 - 10$ μm. This means that infinitely sharp corners on electrodes are impossible to achieve with our device fabrication techniques. Sharp points and edges result in very high field gradients and to make sure this does not impact our COMSOL models, we design all electrode corners with radii of 10 μm. This is a worst case scenario, but we see from the plots in Figures 5.6 and 5.7 that results are quite favorable.

We successfully demonstrate improved droplet sorting functionality utilizing a three electrode microfluidic device. Adoption of DEP sorting of microfluidic droplets depends on the entire process being simple, robust, and reliable. The aim of many droplet microfluidic processes is to improve biological assays, meaning that the primary adopters will not be experimental physicists or engineers, but rather biologists and biochemists. Through our work, we have improved the existing droplet sorting technology with a more efficient electrode design.

Chapter 6

Conclusions

In this dissertation, we have presented an instrument and microfluidic channels that are tools for the generation, storage, manipulation, and characterization of tiny emulsion droplets. Each microfluidic device functions as the analog to a particular bench top bulk-scale operation. Connected together, these microfluidic modules become the tools that enable use of microfluidic droplets as microreaction volumes.

Microfluidic droplet production is fast and robust. The challenge is to ensure downstream modules are equally fast and robust; this maintains sample throughput and minimizes the likelihood of sample cross-contamination. We have addressed these concerns in three key areas: on-chip droplet incubation, addition of volume to droplets, and sorting of droplet populations.

In particular, the developments this dissertation covers are:

- Fast, accurate fabrication of tall micro- and millifluidic channels for the incubation of many small droplets or the production of large droplets.

- Passive merging of surfactant-stabilized droplets via controlled interaction of the droplets with perfluorinated butanol.
- Design and operation of a droplet screening instrument for fluorescence measurements.
- Dielectrophoretic droplet sorting using optimized on-chip electrodes.

These particular advancements and droplet functions are paired with an increased understanding of how to design and operate all modules. We have taken droplet microfluidics out of the realm of simple trial-and-error iteration by establishing guidelines for design and operation. This has pushed droplet microfluidics firmly into the realm of scientific tools that can be readily adapted to questions of interest.

Bibliography

[1] Shelley L. Anna, Nathalie Bontoux, and Howard A. Stone. Formation of dispersions using "flow focusing" in microchannels. *Applied Physics Letters*, 82(3):364–366, 2003.

[2] Yung-Chieh Tan, Jeffrey S. Fisher, Alan I. Lee, Vittorio Cristini, and Abraham Phillip Lee. Design of microfluidic channel geometries for the control of droplet volume, chemical concentration, and sorting. *Lab on a Chip*, 4:292–298, 2004.

[3] A. S. Utada, L.-Y. Chu, A. Fernandez-Nieves, D. R. Link, C. Holtze, and D. A. Weitz. Dripping, jetting, drops, and wetting: The magix of microfluidics. *MRS Bulletin*, 32:702–708, 2007.

[4] Adam R. Abate, Amber T. Krummel, Daeyeon Lee, Manuel Marquez, Christian Holtze, and David A. Weitz. Photoreactive coating for high-contrast spatial patterning of microfluidic device wettability. *Lab on a Chip*, 8:2157–2160, 2008.

[5] A. Manz, N. Graber, and H.M. Widmer. Miniaturized total chemical analysis systems: a novel concept for chemical sensing. *Sensors and Actuators B*, 1:244–248, 1990.

[6] Joel Voldman, Martha L. Gray, and Martin A. Schmidt. Microfabrication in biology and medicine. *Annual Review of Biomedical Engineering*, 1:401–425, 1999.

[7] Helen Song, Delai L. Chen, and Rustem F. Ismagilov. Reactions in droplets in microfluidic channels. *Angewandte Chemie International Edition*, 45(44):7336–7356, 2006.

[8] Anne Y. Fu, Hou-Pu Chou, Charles Spence, Frances H. Arnold, and Stephen R. Quake. An integrated microfabricated cell sorter. *Analytical Chemistry*, 74:2451–2457, 2002.

[9] Shia-Yen Teh, Robert Lin, Lung-Hsin Hung, and Abraham P. Lee. Droplet microfluidics. *Lab on a Chip*, 8:198–220, 2008.

[10] Yolanda Schaerli and Florian Hollfelder. The potential of microfluidic water-in-oil droplets in experimental biology. *Molecular BioSystems*, 5:1392–1404, 2009.

[11] Andrew J. deMello. Control and detection of chemical reactions in microfluidic systems. *Nature*, 442:394–402, 2006.

[12] Ho Cheung Shum, Jin-Woong Kim, and David A. Weitz. Microfluidic fabrication of monodisperse biocompatible and biodegradable polymersomes with controlled permeability. *Journal of the American Chemical Society*, 130:9543–9549, 2008.

[13] Ho Cheung Shum, Daeyeon Lee, Insun Yoon, Tom Kodger, and David A. Weitz. Double emulsion templated monodisperse phospholipid vesicles. *Langmuir*, 24(15):7651–7653, 2008-2.

[14] Jessamine Ng Lee, Cheolmin Park, and George M. Whitesides. Solvent compatibility of poly(dimethylsiloxane)-based microfluidic devices. *Analytical Chemistry*, 75:6544–6554, 2003.

[15] Adam R. Abate, Daeyeon Lee, Thao Do, Christian Holtze, and David A. Weitz. Glass coating for pdms microfluidic channels by sol-gel methods. *Lab on a Chip*, 8:516–518, 2008.

[16] Adam R. Abate, Daeyeon Lee, Christian Holtze, Amber Krummel, Thao Do, and David A. Weitz. Functionalized glass coating for pdms microfluidic devices. In Keith E. Herold and Avraham Rasooly, editors, *Lab on a Chip Technology: Fabrication and microfluidics*, volume 1. Horizon Scientific Press, 2009.

[17] Mark B. Romanowsky, Adam R. Abate, Assaf Rotem, Christian Holtze, and David A. Weitz. High throughput production of single core double emulsions in a parallelized microfluidic device. *Lab on a Chip*, 12:802–807, 2012.

[18] Darren R. Link, Erwan Grasland-Mongrain, Agnes Duri, Flavie Sarrazin, Zhengdong Cheng, Galder Cristobal, Manuel Marquez, and David A. Weitz. Electric control of droplets in microfluidic devices. *Angewandte Chemie International Edition*, 45:2556–2560, 2006.

[19] Sarah Köster, Francesco E. Angile, Honey Duan, Jeremy J. Agresti, Anton Wintner, Christian Schmitz, Amy C. Rowat, Christoph A. Merten, Dario Pisignano, Andrew D. Griffiths, and David A. Weitz. Drop-based microfluidic devices for encapsulation of single cells. *Lab on a Chip*, 8:1110–1115, 2008.

[20] Jenifer Clausell-Tormos, Diana Lieber, Jean-Christophe Baret, Abdeslam El-Harrak, Oliver J. Miller, Lucas Frenz, Joshua Blouwolff, Katherine J. Humphry, Sarah Köster, Honey Duan, Christian Holtze, D. A. Weitz, Andrew D. Griffiths, and Christoph A. Merten. Droplet-based microfluidic platforms for the encapsulation and screening of mammalian cells and multicellular organisms. *Chemistry & Biology*, 15:427–437, 2008.

[21] Ansgar Huebner, M. Srisa-Art, D. Holt, Chris Abell, Florian Hollfelder, Andrew J. DeMello, and Joshua B. Edel. Quantitative detection of protein expression in single cells using droplet microfluidics. *Chemical Communications*, 0(12):1218–1220, 2007.

[22] Dino DiCarlo, Daniel Irimia, Ronald G. Tompkins, and Mehmet Toner. Continuous inertial focusing, ordering, and separation of particles in microchannels. *Proceedings of the National Academy of Sciences*, 104(48):18892–18897, 2007.

[23] Jon F. Edd, Dino DiCarlo, Katherine J. Humphry, Sarah Köster, Daniel Irimia, David A. Weitz, and Mehmet Toner. Controlled encapsulation of single-cells into monodisperse picolitre drops. *Lab on a Chip*, 8:1262–1264, 2008.

[24] Adam R. Abate, Chia-Hung Chen, Jeremy J. Agresti, and David A. Weitz. Beating poisson encapsulation statistics using close-packed ordering. *Lab on a Chip*, 9:2628–2631, 2009.

[25] Evelien W.M. Kemna, Rogier M. Schoeman, Floor Wolbers, Istvan Vermes, David A. Weitz, and Albert van den Berg. High-yield cell ordering and deterministic cell-in-droplet encapsulation using dean flow in a curved microchannel. *Lab on a Chip*, 12:2881–2887, 2012.

[26] Keunho Ahn, Jeremy Agresti, Henry Chong, Manuel Marquez, and D. A. Weitz. Electrocoalescence of drops synchronized by size-dependent flow in microfluidic channels. *Applied Physics Letters*, 88:264105, 2006.

[27] Adam R. Abate, Tony Hung, Pascaline Mary, Jeremy J. Agresti, and David A. Weitz. High-throughput injection with microfludics using picoinjectors. *Proceedings of the National Academy of Sciences*, 107(45):19163–19166, 2010.

[28] Eric Brouzes, Martina Medkova, Neal Savenelli, Dave Marran, Mariusz Twardowski, J. Brian Hutchison, Jonathan M. Rothberg, Darren R. Link, Norbert Perrimon, and Michael L. Samuels. Droplet microfluidic technology for single-cell high-throughput screening. *Proceedings of the National Academy of Sciences*, 106(34):14195–14200, 2010.

[29] Young Shik Shin, Keunchang Cho, Sun Hee Lim, Seok Chung, Sung-Jin Park, Chanil Chung, Dong-Chul Han, and Jun Keun Chang. Pdms-based micro pcr chip with parylene coating. *Journal of Micromechanics and Microengineering*, 13:768–774, 2003.

[30] N. Reginald Beer, Benjamin J. Hindson, Elizabeth K. Wheeler, Sara B. Hall, Klint A. Rose, Ian M. Kennedy, and Bill W. Colston. On-chip, real-time, single-copy polymerase chain reaction in picoliter droplet. *Analytical Chemistry*, 79:8471–8475, 2007.

[31] N. Reginald Beer, Elizabeth K. Wheeler, Lorenna Lee-Houghton, Nicholas Watkins, Shanavaz Nasarabadi, Nicole Hebert, Patrick Leung, Don W. Amold, Christopher G. Bailey, and Bill W. Colston. On-chip single-copy real-time reverse-transcription pcr in isolated picoliter droplets. *Analytical Chemistry*, 80:1854–1858, 2008.

[32] Christian H.J. Schmitz, Amy C. Rowat, Sarah Köster, and David A. Weitz. Dropspots: a picoliter array in a microfluidic device. *Lab on a Chip*, 9(1):44–49, 2009.

[33] Jeremy J. Agresti, Eugene Antipov, Adam R. Abate, Keunho Ahn, Amy C. Rowat, Jean-Christophe Baret, Manuel Marquez, Alexander M. Klibanov, Andrew D. Griffiths, and David A. Weitz. Ultrahigh-throughput screening in drop-based microfluidics for directed evolution. *Proceedings of the National Academy of Sciences*, 107(9):4004–4009, 2010.

[34] Linas Mazutis, John Gilbert, W. Lloyd Ung, David A. Weitz, Andrew D. Griffiths, and John A. Heyman. Single-cell analysis and sorting using droplet-based microfluidics. *Nature Protocols*, 8(5):870–891, 2013.

[35] Seila Selimovic, Frederic Gobeaux, and Seth Fraden. Mapping and manipulating temperature-concentration phase diagrams using microfluidics. *Lab on a Chip*, 10:1696–1699, 2010.

[36] Younan Xia and George M. Whitesides. Soft lithography. *Angewandte Chemie International Edition*, 37:550–575, 1998.

[37] Younan Xia and George M. Whitesides. Soft lithography. *Annual Review of Materials Science*, 28:153–184, 1998.

[38] David C. Duffy, J. Cooper McDonald, Oliver J.A. Schueller, and George M. Whitesides. Rapid prototyping of microfluidic systems in poly(dimethylsiloxane). *Analytical Chemistry*, 70(23):4974–4984, 1998.

[39] J. Cooper McDonald, David C. Duffy, Janelle R. Anderson, Daniel T. Chiu, Hongkai Wu, Olivier J. A. Schueller, and George M. Whitesides. Fabrication of microfluidic systems in poly(dimethylsiloxane). *Electrophoresis*, 21:27–40, 2000.

[40] MarieClaire Blanger and Yves Marois. Hemocompatibility, biocompatibility, inflammatory and in vivo studies of primary reference materials low-density polyethylene and polydimethylsiloxane: A review. *Journal of Biomedical Materials Research*, 58(5):467–477, 2001.

[41] Troy R. Hendricks and Ilsoon Lee. Wrinkle-free nanomechanical film: Control and prevention of polymer film buckling. *NanoLetters*, 7(2):372–379, 2007.

[42] Lord Rayleigh. On the capillary phenomena of jets. *Proceedings of the Royal Society of London*, 29:71–97, 1879.

[43] Piotr Garstecki, Irina Gitlin, Willow DiLuzio, George M. Whitesides, Eugenia Kumacheva, and Howard A. Stone. Formation of monodisperse bubbles in a microfluidic flow-focusing device. *Applied Physics Letters*, 85(13):2649–2651, 2004.

[44] Piotr Garstecki, Howard A. Stone, and George M. Whitesides. Mechanism for flow-rate controlled breakup in confined geometries: A route to monodisperse emulsions. *Physical Review Letters*, 94(16):164501, 2005.

[45] Piotr Garstecki, Michael J. Fuerstman, Howard A. Stone, and George M. Whitesides. Formation of droplets and bubbles in a microfluidic t-junction - scaling and mechanism of break-up. *Lab on a Chip*, 6:437–446, 2006.

[46] Adam R. Abate, Pascaline Mary, Volkert van Steijn, and David A. Weitz. Experimental validation of plugging during drop formation in a t-junction. *Lab on a Chip*, 12:1516–1521, 2012.

[47] T. P. Hoar and J. H. Schulman. Transparent water-in-oil dispersions: the oleopathic hydro-micelle. *Nature*, 152:102–103, 1943.

[48] Tadahiro Okazawa and Jan Bron. On thermodynamically stable emulsions: I. thermodynamic background. *Journal of Colloid and Interface Science*, 69(1):86–96, 1979.

[49] Drew Myers. *Surfactant Science and Technology.* John Wiley & Sons, Inc., Hoboken, NJ, 3rd edition, 2006.

[50] Nicolas Bremond and Jérôme Bibette. Exploring emulsion science with microfluidics. *Soft Matter*, 8:10549–10559, 2012.

[51] Feng Hua, Yugang Sun, Anshu Gaur, Matthew A. Meitl, Lise Bilhaut, Lolita Rotkina, Jingfeng Wang, Phil Geil, Moonsub Shim, John A. Rogers, and Anne Shim. Polymer imprint lithography with molecular-scale resolution. *NanoLetters*, 4(12):2467–2471, 2004.

[52] Product information: Dow corning 184 silicone elastomer, 2010.

[53] Ralph A. Sperling. Droplet cannon. *(unpublished results)*.

[54] Abraham D. Stroock, Stephen K. W. Dertinger, Armand Ajdari, Igor Mezic, Howard A. Stone, and George M. Whitesides. Chaotic mixer for microchannels. *Science*, 295:647–651, 2002.

[55] K. Handique and M. A. Burns. Mathematical modeling of drop mixing in a slit-type microchannel. *Journal of Micromechanics and Microengineering*, 11:548–554, 2001.

[56] Helen Song, Joshua D. Tice, and Rustem F. Ismagilov. A microfluidic system for controlling reaction networks in time. *Angewandte Chemie International Edition*, 42:767–772, 2003.

[57] F. Sarrazin, L. Prat, N. DiMiceli, G. Christobal, D. R. Link, and D. A. Weitz. Mixing characterization inside microdroplets engineered on a microcoalescer. *Chemical Engineering Science*, 62:1042–1048, 2007.

[58] Peter Fischer and Philipp Erni. Emulsion drops in external flow fields - the role of liquid interfaces. *Current Opinion in Colloid & Interface Science*, 12:196–205, 2007.

[59] Valerie Taly, Bernard T. Kelly, and Andrew D. Griffiths. Droplets as microreactors for high-throughput biology. *ChemBioChem*, 8:263–272, 2007.

[60] Darren R. Link, S. L. Anna, D. A. Weitz, and Howard A. Stone. Geometrically mediated breakup of drops in microfluidic devices. *Physical Review Letters*, 92(5):054503, 2004.

[61] Thomas Ward, Magalie Faivre, Manouk Abkarian, and Howard A. Stone. Microfluidic flow focusing: Drop size and scaling in pressure versus flow-rate-driven pumping. *Electrophoresis*, 26:3716–3724, 2005.

[62] Zhihong Nie, MinsSeok Seo, Shengqing Xu, Patrick C. Lewis, Michelle Mok, Eugenia Kumacheva, George M. Whitesides, Piotr Garstecki, and Howard A. Stone. Emulsification in a microfluidic flow-focusing device: effect of the viscosities of the liquids. *Microfluidics and Nanofluidics*, 5:585–594, 2008.

[63] Charles N. Baroud, Francois Gallaire, and Remi Dangla. Dynamics of microfluidic droplets. *Lab on a Chip*, 10:2032–2045, 2010.

[64] Larysa Baraban, Fabien Bertholle, Merijn L. M. Salverda, Nicolas Bremond, Pascal Panizza, Jean Baudry, J. Arjan G. M. de Visser, and Jérôme Bibette. Millifluidic droplet analyser for microbiology. *Lab on a Chip*, 11:4057–4062, 2011.

[65] Lucas Frenz, Kerstin Blank, Eric Brouzes, and Andrew D. Griffiths. Reliable microfluidic on-chip incubation of droplets in delay-lines. *Lab on a Chip*, 9:1344–1348, 2009.

[66] Esther Amstad, Donald M. Aubrecht, Assaf Rotem, Christian Holtze, Michael P. Brenner, and David A. Weitz. The microfluidic nebulator: Production of sub-30 nm nanoparticles through supersonic spray drying. *(in preparation)*.

[67] A.A. Yussuf, I. Sbarski, J.P. Hayes, M. Solomon, and N. Tran. Microwave welding of polymeric-microfluidic devices. *Journal of Micromechanics and Microengineering*, 15:1692–1699, 2005.

[68] Holger Becker and Claudia Gartner. Polymer microfabrication technologies for microfluidic systems. *Analytical and Bioanalytical Chemistry*, 390:89–111, 2008.

[69] Ruchi Gupta, Sara J. Baldock, Pilar Carreras, Peter R. Fielden, Nick J. Goddard, Stephan Mohr, Behnam S. Razavi, and Bernard J. Treves Brown. A microfludic device for self-synchronized production of droplets. *Lab on a Chip*, 11:4052–4056, 2011.

[70] Mateusz L. Hupert, W. Jason Guy, Shawn D. Llopis, Hamed Shadpour, Sudheer Rani, Dimitris E. Nikitopoulos, and Steven A. Soper. Evaluation of micromilled metal mold masters for the replication of microchip electrophoresis devices. *Microfluidics and Nanofluidics*, 3:1–11, 2007.

[71] Richard Novak, Navpreet Ranu, and Richard A. Mathies. Rapid fabrication of nickel molds for prototyping embossed plastic microfluidic devices. *Lab on a Chip*, 13:1468–1471, 2013.

[72] J. Cooper McDonald, Michael L. Chabinyc, Steven J. Metallo, Janelle R. Anderson, Abraham D. Stroock, and George M. Whitesides. Prototyping of microfluidic devices in poly(dimethylsiloxane) using solid-object printing. *Analytical Chemistry*, 74:1537–1545, 2002.

[73] Julian Thiele, Adam R. Abate, Ho Cheung Shum, Simone Bachtler, Stephan Frster, and David A. Weitz. Fabrication of polymersomes using double-emulsion templates in glass-coated stamped microfluidic devices. *Small*, 6(16):1723–1727, 2010.

[74] Ho Cheung Shum, Adam R. Abate, Daeyeon Lee, Andre R. Studart, Baoguo Wang, Chia-Hung Chen, Julian Thiele, Rhutesh K. Shah, Amber Krummel, and David A. Weitz. Droplet microfluidics for fabrication of non-spherical particles. *Macromolecular Rapid Communications*, 31:108–118, 2010.

[75] Hirotaka Sasaki, Hiroaki Onoe, Toshihisa Osaki, Ryuji Kawano, and Shoji Takeuchi. Parylene-coating in pdms microfluidic channels prevents the absorption of fluorescent dyes. *Sensors and Actuators B*, 150(1):478–482, 2010.

[76] Ned Bowden, Scott Brittain, Anthony G. Evans, John W. Hutchinson, and George M. Whitesides. Spontaneous formation of ordered structures in thin films of metals supported on an elastomeric polymer. *Nature*, 393:146–149, 1998.

[77] Ned Bowden, Wilhelm T. S. Huck, Kateri E. Paul, and George M. Whitesides. The controlled formation of ordered, sinusoidal structures by plasma oxidation of an elastomeric polymer. *Applied Physics Letters*, 75(17):2557–2559, 1999.

[78] Radivoje Prodanovic, Raluca Ostafe, Milan Blanusa, and Ulrich Schwaneberg. Vanadium bromoperoxidase-coupled fluorescent assay for flow cytometry sorting of glucose oxidase gene libraries in double emulsions. *Analytical and Bioanalytical Chemistry*, 404(5):1439–1447, 2012.

[79] Kalia Bernath, Mingtan Hai, Enrico Mastrobattista, Andrew D. Griffiths, Shlomo Magdassi, and Dan S. Tawfik. In vitro compartmentalization by double emulsions: sorting and gene enrichment by fluorescence activated cell sorting. *Analytical Biochemistry*, 325:151–157, 2004.

[80] Dragana Despotovic, Ljubica Vojcic, Radivoje Prodanovic, Ronny Martinez, Karl-Heinz Maurer, and Ulrich Schwaneberg. Fluorescent assay for directed evolution of perhydrolases. *Journal of Biomolecular Screening*, 17(6):796–805, 2012.

[81] Donald M. Aubrecht, W. Lloyd Ung, Achini Opathalage, Seth Fraden, and David A. Weitz. Tutorial on screening and sorting with drop-based microfluidics. *(in preparation).*

[82] Henrik Bruus. *Theoretical Microfluidics*. Oxford University Press, Inc., New York, NY, 2008.

[83] Henrik Bruus. Acoustofluidics 1: Governing equations in microfluidics. *Lab on a Chip*, 11:3742–3751, 2011.

[84] Rajinder Pal. Effect of droplet size on the rheology of emulsions. *AIChE Journal*, 42(11):3181–3190, 1996.

[85] Rajinder Pal. Viscosity-concentration equation for emulsions of nearly spherical droplets. *Journal of Colloid and Interface Science*, 231:168–175, 2000.

[86] Mario DeMenech, Piotr Garstecki, Fabien Jousse, and Howard A. Stone. Transition from squeezing to dripping in a microfluidic t-shaped junction. *Journal of Fluid Mechanics*, 595:141–162, 2008.

[87] Adam R. Abate, A. Poitzsch, Y.Hwang, J. Lee, J. Czerwinska, and David A. Weitz. Impact of inlet channel geometry on microfluidic drop formation. *Physical Review E*, 80:026310, 2009.

[88] Manhee Lee, Jesse W. Collins, Donald M. Aubrecht, Ralph A. Sperling, Laura Solomon, Jong-wook Ha, Gi-Ra Yi, David A. Weitz, and Vinothan N. Manoharan. Synchronized reinjection and coalescence of droplets in microfluidics. *Lab on a Chip*, (submitted), 2013.

[89] Product information: Live/dead cell vitality assay kit (l34951), 2004.

[90] Michael J. Moran and Howard N. Shapiro. *Fundamentals of Engineering Thermodynamics*. John Wiley & Sons, Inc., Hoboken, NJ, 5th edition, 2004.

[91] C. Holtze, Amy C. Rowat, Jeremy J. Agresti, J. Brian Hutchison, Francesco E. Angile, Christian H.J. Schmitz, Sarah Köster, Honey Duan, Katherine J. Humphry, Randall A. Scanga, J.S. Johnson, Dario Pisignano, and David A. Weitz. Biocompatible surfactants for water-in-fluorocarbon emulsions. *Lab on a Chip*, 8:1632–1639, 2008.

[92] Jean-Christophe Baret. Surfactants in droplet-based microfluidics. *Lab on a Chip*, 12:422–433, 2012.

[93] D. Fennell Evans and Hakan Wennerstrom. *The Colloidal Domain: Where Physics, Chemistry, Biology, and Technology Meet*. Advances in Interfacial Engineering. Wiley-VCH, New York, NY, 2nd edition, 1999.

[94] Paul C. Hiemenz and Raj Rajagopalan. *Principles of Colloid and Surface Chemistry*. Marcel Dekker, Inc., New York, NY, 3rd edition, 1997.

[95] Reinhard Miller, Paul Joos, and Valentin B. Fainerman. Dynamic surface and interfacial tensions of surfactant and polylmer solutions. *Advances in Colloid and Interface Science*, 49:249–302, 1994.

[96] Bradley A. Cicciarelli, Kenneth A. Smith, and T. Alan Hatton. Dynamic surface tension behavior in a photoresponsive surfactant system. *Langmuir*, 23(9):4753–4764, 2007.

[97] Rustem F. Ismagilov, Abraham D. Stroock, Paul J. A. Kenis, George Whitesides, and Howard A. Stone. Experimental and theoretical scaling laws for transverse diffusive broadening in two-phase laminar flows in microchannels. *Applied Physics Letters*, 76(17):2376–2378, 2000.

[98] Zhihong Nie, Shengqing Xu, Minseok Seo, Patrick C. Lewis, and Eugenia Kumacheva. Polymer particles with various shapes and morphologies produced in continuous microfluidic reactors. *Journal of the American Chemical Society*, 127:8058–8063, 2005.

[99] Alison M. Skelley, Oktay Kirak, Heikyung Suh, Rudolf Jaenisch, and Joel Voldman. Microfluidic control of cell pairing and fusion. *Nature Methods*, 6(2):147–152, 2009.

[100] Nicolas Bremond, Abdou R. Thiam, and Jérôme Bibette. Decompressing emulsion droplets favors coalescence. *Physical Review Letters*, 100(2):024501, 2008.

[101] James C. Bird, William D. Ristenpart, Andrew Belmonte, and Howard A. Stone. Critical angle for electrically driven coalescence of two conical droplets. *Physical Review Letters*, 103(16):164502, 2009.

[102] Max Chabert, Kevin D. Dorfman, and Jean-Louis Viovy. Droplet fusion by alternating current (ac) field electrocoalescence in microchannels. *Electrophoresis*, 26:3706–3715, 2005.

[103] Craig Priest, Stephan Herminghaus, and Ralf Seemann. Controlled electrocoalescence in microfluidics: Targeting a single lamella. *Applied Physics Letters*, 89(13):134101, 2006.

[104] Abdou R. Thiam, Nicolas Bremond, and Jérôme Bibette. Breaking of an emulsion under an ac electric field. *Physical Review Letters*, 102(18):188304, 2009.

[105] Abdou R. Thiam, Nicolas Bremond, and Jérôme Bibette. Adhesive emulsion bilayers under an electric field: From unzipping to fusion. *Physical Review Letters*, 107(6):068301, 2011.

[106] Michele Zagnoni, Guillaume Le Lain, and Jonathan M. Cooper. Electrocoalescence mechanisms of microdroplets using localized electric fields in microfluidic channels. *Langmuir*, 26(18):14443–14449, 2010.

[107] Laura Solomon, Donald M. Aubrecht, Jesse W. Collins, Vinothan N. Manoharan, and David A. Weitz. Microfluidic droplet combiner for use in self-assembling colloidal systems, 2010.

[108] S. Protiere, M.Z. Bazant, D.A. Weitz, and H.A. Stone. Droplet breakup in flow past an obstacle: A capillary instability due to permeability variations. *Europhysics Letters*, 92:54002, 2010.

[109] Michele Zagnoni and Jonathan M. Cooper. A microdroplet-based shift register. *Lab on a Chip*, 10:3069–3073, 2010.

[110] Paul Abbyad, Remi Dangla, Antigoni Alexandrou, and Charles N. Baroud. Rails and anchors: guiding and trapping droplet microreactors in two dimensions. *Lab on a Chip*, 11:813–821, 2011.

[111] Charles N. Baroud, Jean-Pierre Delville, Francois Gallaire, and Regis Wunenburger. Thermocapillary valve for droplet production and sorting. *Physical Review E*, 75(4):046302, 2007.

[112] Xize Niu, Shelly Gulati, Joshua B. Edel, and Andrew J. deMello. Pillar-induced droplete merging in microfluidic circuits. *Lab on a Chip*, 8:1837–1841, 2008.

[113] Manu Prakash and Neil Gershenfeld. Microfluidic bubble logic. *Science*, 315:832–835, 2007.

[114] Michael Schindler and Armand Ajdari. Droplet traffic in microfluidic networks: A simple model for understanding and designing. *Physical Review Letters*, 100:044501, 2008.

[115] Bo Zheng, Joshua D. Tice, and Rustem F. Ismagilov. Formation of droplets of alternating composition in microfluidic channels and applications to indexing of concentrations in droplet-based assays. *Analytical Chemistry*, 76(17):4977–4982, 2004.

[116] Hakim Boukellal, Seila Selimovic, Yanwei Jia, Galder Cristobal, and Seth Fraden. Simple, robust storage of drops and fluids in a microfluidic device. *Lab on a Chip*, 9:331–338, 2009.

[117] D. T. Wasan, J. J. McNamara, S. M. Shah, K. Sampath, and N. Aderangi. The role of coalescence phenomena and interfacial rheological properties in enhanced oil recovery: An overview. *Journal of Rheology*, 23(2):181–207, 1979.

[118] Ashleigh B. Theberge, Estelle Mayot, Abdeslam El Harrak, Felix Kleinschmidt, Wilhelm T.S. Huck, and Andrew D. Griffiths. Microfluidic platform for combinatorial synthesis in picolitre droplets. *Lab on a Chip*, 12:1320–1326, 2012.

[119] L. Gary Leal. Flow induced coalescence of drops in a viscous fluid. *Physics of Fluids*, 16(6):1833, 2004.

[120] Joshua Lederberg. A simple method for isolating individual microbes. *Journal of Bacteriology*, 68:258–259, 1954.

[121] G. J. V. Nossal and Joshua Lederberg. Antibody production by single cells. *Nature*, 181:1419–1420, 1958.

[122] Boris Rotman. Measurement of activity of single molecules of b-galactosidase. *Proceedings of the National Academy of Sciences*, 47:1981–1991, 1961.

[123] Ilke Akartuna. Comparison of electrocoalescence to passive coalescence using perfluorobutanol. *(private communication)*, 2013.

[124] Emily R. Russell, Joris Sprakel, Thomas E. Kodger, and David A. Weitz. Colloidal gelation of oppositely charged particles. *Soft Matter*, 8:8697–8703, 2012.

[125] P. Poulin and Jérôme Bibette. Adhesion of water droplets in organic solvent. *Langmuir*, 14:6341–6343, 1998.

[126] H.M. Princen. Geometry of clusters of strongly coagulated fluid drops and the occurrence of collapsed plateau borders. *Colloids and Surfaces*, 9(1):47–66, 1984.

[127] Fernando Leal-Calderon, Jérôme Bibette, and Veronique Schmitt. Force measurements. In *Emulsion Science*, pages 52–104. Springer, New York, NY, 2007.

[128] Xize Niu, Mengying Zhang, Suili Peng, Weijia Wen, and Ping Sheng. Real-time detection, control, and sorting of microfluidic droplets. *Biomicrofluidics*, 1:044101, 2007.

[129] Ilke Akartuna, Donald M. Aubrecht, Thomas E. Kodger, and David A. Weitz. Controlled destabilization of a water-in-oil emulsion via addition of fluorinated alcohol using droplet microfluidic techniques. *(in preparation)*.

[130] Mira T. Guo, Assaf Rotem, John A. Heyman, and David A. Weitz. Droplet microfluidics for high-throughput biological assays. *Lab on a Chip*, 12:2146–2155, 2012.

[131] Keunho Ahn, Charles Kerbage, Tom P. Hunt, R. M. Westervelt, Darren R. Link, and D. A. Weitz. Dielectrophoretic manipulation of drops for high-speed microfluidic sorting devices. *Applied Physics Letters*, 88:024104, 2006.

[132] David J. Griffiths. *Introduction to Electrodynamics*. Prentice-Hall, Inc, Upper Saddle River, NJ, 3rd edition, 1999.

[133] A. Castellanos, A. Ramos, A. Gonzalez, N. G. Green, and H. Morgan. Electrohydrodynamics and dielectrophoresis in microsystems: scaling laws. *Journal of Physics D: Applied Physics*, 36:2584–2597, 2003.

[134] Ronald Pethig. Review article - dielectrophoresis: Status of the theory, technology, and applications. *Biomicrofluidics*, 4:022811, 2010.

[135] Keith Andrew Brown. *Imaging and Manipulation of Nanoscale Materials with Coaxial and Triaxial AFM Probes*. Ph.d. dissertation, Harvard University, 2011.

[136] Manoj K. Chaudhury and George M. Whitesides. Direct measurement of interfacial interactions between semispherical lenses and flat sheets of poly(dimethylsiloxane) and their chemical derivatives. *Langmuir*, 7(5):1013–1025, 1991.

[137] Y. Rotenberg, L. Boruvka, and A. W. Neumann. Determination of surface tension and contact angle from the shapes of axisymmetric fluid interfaces. *Journal of Colloid and Interface Science*, 93(1):169–183, 1983.

[138] Youssef Touhami, Graham H. Neale, Vladimir Hornof, and Habib Khalfalah. A modified pendant drop method for transient and dynamic interfacial tension measurement. *Colloids and Surfaces A: Physicochemical and Engineering Aspects*, 112:31–41, 1996.

[139] Rafael C. Gonzalez, Richard E. Woods, and Steven L. Eddins. *Digital Image Processing Using MATLAB*. Pearson Education, Inc., Upper Saddle River, NJ, 2004.

Appendix A

Experimental Notes

A.1 Soft Lithography Protocol

Soft lithography takes advantage of microscale fabrication tools initially designed to pattern and create structures, and repurposes them to fabricate relief structures for molding microfluidic channels. SU-8, a photocurable epoxy, is patterned into a series of connected, raised features atop a hard substrate, typically glass or silicon. A liquid polymer such as poly-dimethylsiloxane (PDMS) is then poured over the features and cured. The cured polymer block is pealed off the mold and adhered to a flat, supportive substrate, typically a glass microscope slide [36, 39]. In this manner, the original epoxy features have now become air-filled cavities between the polymer walls and ceiling, and the glass floor. Via holes punched through the cured polymer allow connections between the cavity features and the external world. Through these connections, fluids can be flowed into the chip, turning the cavities into fluidic channels. Figure A.1 shows this process.

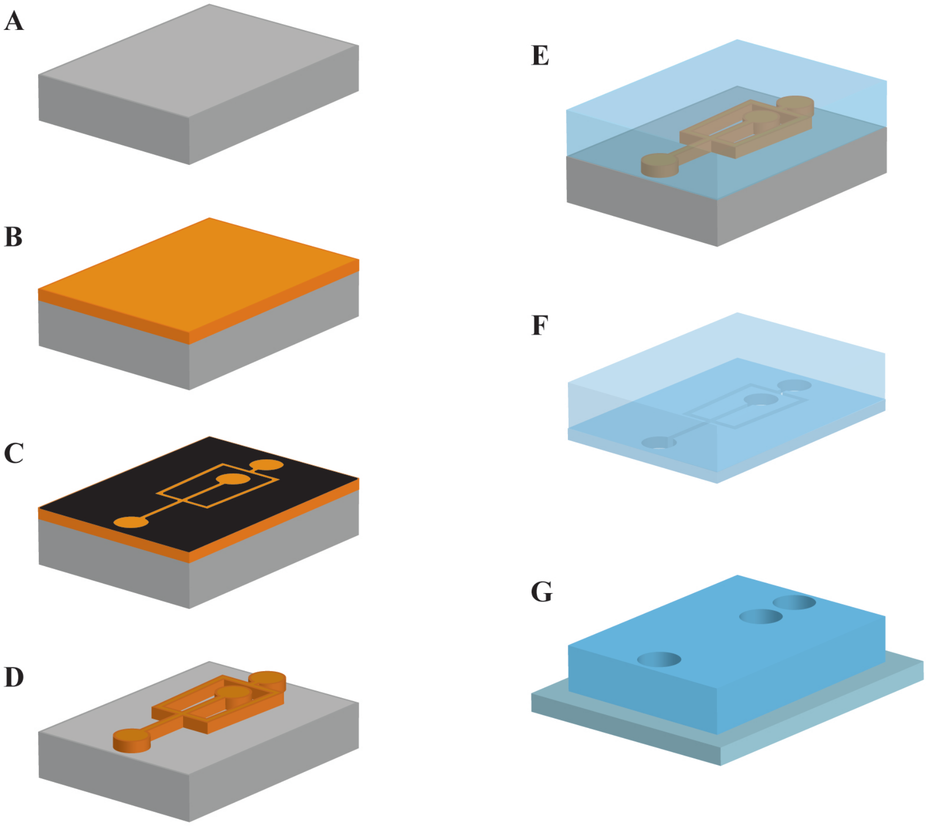

Figure A.1: Illustration of soft lithography processing steps. **(A)** The substrate is cleaned. **(B)** SU-8 photoresist is spun onto the substrate and baked to remove solvent. **(C)** A photomask is placed over the photoresist and the sandwich is exposed to 365 nm UV light, transferring the patter from the photomask to the resist. **(D)** The photomask is removed, the substrate and resist are baked again, and then submerged in a solvent to remove unexposed photoresist. This creates the relief mold that will be cast into PDMS. **(E)** Two-part PDMS is mixed, poured over the mold, and cured by baking at 65°C. **(F)** The cured PDMS is pealed from the mold. **(G)** Holes are punched through the PDMS and the channel is created by sealing the PDMS to a glass slide substrate via treatment with oxygen plasma.

Microfabrication of master molds is performed in the Harvard University Center for Nanoscale Systems Soft Materials Cleanroom (SMCR). SU-8 photoresists from the 2000 and 3000 series (Microchem Corp.) are coated onto research grade silicon wafers (University

Wafer) using an SCS G3 spin coater (Specialty Coating Systems). Spin speeds for coating are 1000-4000 rpm and are determined from the standard Microchem spin curves. Baking temperatures and all processing times are also determined from the standard Microchem SU-8 data sheet. UV exposure is performed using a flood illuminator or contact aligner (OAI). Following the necessary baking and exposure processes, SU-8 photoresist is developed by submersion in propylene glycol methyl ether acetate (PGMEA) (Sigma-Aldrich), with a final rinse in isopropyl alcohol (Sigma-Aldrich). The completed structure is dried with compressed air and baked at 200°C for 5 minutes to remove all solvent residues.

For most microfluidic applications, the liquid polymer used to create the channels is PDMS. It is purchased as a two-part system, requiring the base polymer be mixed with the cross-linking agent prior to baking. PDMS cures translucent, is easily bonded to glass, can have its surface chemistry modified in manners similar to glass, and is biocompatible [36, 38, 40, 41]. For these reasons, it is ideally suited to use in microfluidic systems, particularly those used for biological experiments.

For all experiments, Sylgard 184 (Dow Corning) PDMS is mixed 10:1 base:curing agents and cured over the finished molds at 65°C for 18 hours. After curing, the PDMS is removed from the mold, fluid tubing via holes are punched with a biopsy punch, the channels are cleaned with Scotch tape, and and the PDMS bonded to glass using oxygen plasma treatment [136].

A.2 Machined Millifluidic Molds

Millifluidic channel designs are drafted in 2D using AutoCAD (Autodesk, Inc.) or DraftSight (Dassault Systems), and imported to Mastercam x6 (CNC Software, Inc.) for conversion to CNC g-code. Mastercam x6 is used to define mill bit parameters, material parameters, and verify tool paths by backplot simulation. The finished g-code is transferred to a TRAK K2 mill equipped with a ProtoTRAK CAM controller (Southwestern Industries, Inc). The millifluidic channels features are milled into Delrin (McMaster-Carr) resulting in a negative master of the millifluidic device.

Standard small mill bits are used. Diameters of the bits range from 0.254-3.175 mm (McMaster-Carr). The rotation rate of the bit is set within the range of 1600-2600 rpm and the table translation rate is in the range of 1-6 inches per minute, depending on the feature size and mill bit being used. Smaller bits and tight corners require high rotation rate and slow translation.

Once completed, the mold is washed in a 1:1 solution of Simple Green in water, rinsed in clean water, and dried with compressed air.

The surface roughness of finished molds is measured using a KLA-Tencor P16+ stylus profilometer. Scans are performed at 50 μm/sec with a z range of 1048 μm and z resolution of 0.0625 nm.

Electron micrographs of finished molds are acquired on a Supra55 scanning electron microscope (Zeiss) with an accelerating voltage of 5 kV. Images are generated used the secondary electron detector. Molds are sputtered with a thin coating of Pt/Pd prior to SEM imaging to avoid charging.

Fluidic channels are created by curing Sylgard 184 PDMS (Dow-Corning) in the mold. Methods for sealing of the channels and production of droplets are described in Section A.3.

To measure the channel cross sections plotted in Figure 2.6(D), PDMS is cast over the molds shown in Figures 2.6(A)-(C). A razor blade is used to section a thin slice of PDMS perpendicular to the channels. This section is placed on a glass slide and imaged on a Nikon Eclipse Ti-S inverted microscope. Image thresholding and edge determination is performed in MATLAB, resulting in the data plotted in Figure 2.6(D).

A.3 Microfluidic Materials and Methods

Fluidic channel molds are fabricated via photolithography of SU-8 photoresist on a silicon wafer, as described in Section A.1. Microfluidic channels are then cast from these molds in PDMS, cured, and bonded to a glass substrate To render the sealed microfluidic channels fluorophillic, Aquapel (Ryder Fleet Products) is flowed through the channels for 30 seconds, then flushed with Novec HFE-7500 (3M).

Microfluidic experiments are imaged on a Nikon Eclipse Ti-S inverted microscope using either a Fastec HiSpec 1 (Fastec Imaging) or Phantom v7.3 (Vision Research) fast camera. Fluid control is provided by KDS 910 OEM syringe pumps (KD Scientific) driving 1 mL and 3 mL syringes. Full field fluorescence images are collected on a Leica SP5 inverted fluorescence confocal microscope.

Unless otherwise noted, the dispersed phase for all experiments is DI water. No surfactant is present in the aqueous phase. Unless noted, the continuous phase is Novec HFE-7500 containing 2wt% PFPE-PEG-PFPE triblock copolymer surfactant [91].

Droplet production is typically performed in a channel with a thickness of 10-50 μm and a width of 10-50 μm. Geometry is tailored to yield droplets of particular size for a specific application. Flow rates for droplet production are typically 50-500 μL/hr for the dispersed phase, and 100-1500 μL/hr for the continuous phase. Reinjection or processing of pre-made droplet populations is performed at lower throughput, typically pumping the dense droplet phase at 10-100 μL/hr and a spacing oil phase at 300-1000 μL/hr.

Imaging of droplet populations is accomplished in one of three manners: 1) the droplets are imaged by fast camera as they flow toward the channel outlet; 2) the droplets are flowed into a large serpentine channel or other on-chip volume and flow is stopped so the droplets may be imaged with a standard frame rate camera; 3) the droplets are collected off-chip and then pipetted into sample viewing chambers for imaging on a microscope. Viewing chambers are created by sandwiching two standard No. 1.5 coverslips between a standard microscope slide and a third coverslip. The coverslips are arranged such that the third coverslip is suspended over the microscope slide, forming a gap of thickness equal to the thickness of the other two coverslips. NOA81 (Norland Products) is used to glue the coverslips and slide together. Prior to gluing, the suspended coverslip and the microscope slide are treated with Aquapel.

For fluoroalcohol-induced coalescence experiments, the microfluidic channels are fabricated 25 μm high with an additional 8 μm high guiding attic. 2,2,3,3,4,4,4-Heptafluoro-1-butanol (Oakwood Products) is used as the perfused fluoroalcohol phase to induce coalescence. 1H,1H,2H,2H-Perfluoro-1-octanol (Sigma Aldrich) and Novec HFE-7500 (3M) are used as perfusion phase negative controls. Prior to performing droplet coalescence, the reinjected droplet population is formed in a flow-focusing geometry microfluidic channel with droplet nozzle cross section 15 μm x 15 μm. Flow rates for droplet production are 180 μL/hr and 100 μL/hr for the continuous and dispersed phases, respectively. Droplets are collected into a 1 mL plastic syringe. Droplet coalescence experiments are performed with the following flow rates: 15 μL/hr reinjected droplets, 150 μL/hr reinjected droplet spacing oil, 40

μL/hr droplet-forming phase, 300 μL/hr continuous phase, 10 μL/hr perfused destabilizing phase, 500 μL/hr restabilizing oil.

Experiment startup for the fluoroalcohol-induced droplet coalescing device is performed in the following sequence: 1) install syringes in pumps and bleed all droplet and fluid tubing lines; 2) connect all HFE-7500-based oil phases and flow at 100 μL/hr for 5 minutes to expel all air and any contaminants from the microfluidic channels; 3) set oil flows to their proper values for the experiment and allow to equilibrate for 3 minutes; 4) connect reinjection droplets and ensure droplets are flowing into the microfluidic channels at the proper rate; 5) connect dispersed phase to form second droplet population on-chip, tune the flow rates, and check that droplets are formed correctly; 6) connect destabilizing and restabilizing fluids, set the flow rates, and check for proper flow.

Surface tension measurements are performed on three instruments: equilibrium measurements are measured on a KSV Sigma 701 tensiometer (Biolin Scientific) with a perfluorosilanized platinum DuNouy ring; dynamic and equilibrium measurements are taken using a custom pendant drop instrument; equilibrium measurements are checked with a custom spinning drop tensiometer. The custom pendant drop setup captures digital images using a Sony XCD-V60 Firewire camera and determines surface tension values using a curve fitting route in MATLAB [137, 138]. Values from this pendant drop instrument are verified against values calculated by a KSV CAM 200 pendant drop surface tension meter (Biolin Scientific).

Fluorescence data for the two color assay characterization of droplet coalescence are recorded on a Leica SP5 inverted fluorescence confocal microscope. Images are recorded with a resolution of 512 x 512 pixels and 8-bit depth. Eight linescans are averaged to produce each line of pixels in the final image, and pixels are scanned at 8 kHz. The green band extends from 500-535 nm, while the red band encompasses 559-709 nm.

Adhesion measurements are performed in droplet imaging chambers fabricated in the following manner: No. 1 glass coverslips are spin-coated with PDMS and cured as noted above for PDMS molds. 1 mm thick glass spacers are inserted between a standard microscope slide and the inverted coverslip. After assembly, the device is coated with Aquapel, dried with compressed air, and then soaked for 5 minutes in a solution of 2wt% PFPE-PEG-PFPE in HFE-7500. The chamber is removed from the surfactant solution, dried with compressed air, and all but one side sealed using 5 minute epoxy. Once the epoxy is cured, the chamber is filled with the appropriate test solution and droplets are pipetted into the test solution using a gel-loading pipette tip. Adhesion is quantified using simultaneous fluorescence and reflection upright confocal microscopy. At the PDMS coverslip interface, a circular adhesive patch appears dark in reflection confocal microscopy due to physical contact between the droplet and the PDMS. Fluorescence confocal microscopy is used to determine the radius of the droplet. Using the contact angle is calculated from these measurements along with measured bulk surface tensions, the energy of adhesion as a function of alcohol concentration is determined, as detailed in Section 4.2.4.

Droplet sorting experiments are performed with 18 MΩ deionized water droplets in a continuous phase of Fluorinert FC-40 (3M) containing 1.8wt% PFPE-PEG-PFPE surfactant. Droplets are flowed onto the sorting chip and continuous phase added to space droplets apart before they encounter the electrodes and bifurcation. Flow rates are tuned to ensure that in the absence of an applied electric field, all droplets pass into the low resistance exit channel, the so-called "waste" channel. Final flow rates for the experiment are as follows: 18 μL/hr aqueous phase, 20 μL/hr droplet formation oil, 300 μL/hr spacing oil. Once this flow is stable, the electrodes are energized with increasing voltages and the droplet response is recorded with a Phantom v5 high speed camera. The electrodes are energized with a continuous 10 kHz square wave ranging from 0 to 1200 V_{P-P} with a DC offset of $0.5V_{P-P}$, such that the waveform contains no negative values.

A.4 Laser Illumination Alignment Procedure

To achieve the improvements in illumination described in Section 3.1, the following alignment procedure was used. Refer to Figure 3.2 for references to mirror mounts.

1. Secure microscope body to optical table and lock laser-line dichroic at 45° to the centerline of the optical port.
2. Measure vertical distance between table surface and center of the optical port. Use a lab jack or spacers to set the emission port of the laser head to the same elevation. Ensure that the laser beam is parallel to the table surface.
3. Set the center point of all mirrors to the same elevation as the optical port and laser head.
4. Tape a piece of paper over the microscope's optical port. Using a Sharpie marker, draw the intended laser path on the optical table.
5. Turn the laser on and decrease its intensity with a neutral density filter at the laser head. Roughly align all mirrors so that the laser beam appears on the piece of paper. Start with the mirror closest to the laser head and work in sequence toward the mi-

croscope. Rotate and translate mirrors so the laser beam remains near the center of all mirrors. Lock all mirror translation.

6. Check laser beam elevation at all mirrors. Adjust mirrors as necessary to ensure the beam remains parallel to the table.
7. Iterate steps 5 and 6 until the laser beam is near the center of the optical port. Lock all coarse adjustments.
8. Use the fine rotation knobs on gimbal mount G2 to center the laser beam on the optical port.
9. Remove the paper from the optical port and remove the microscope objective. Place a thin sheet of paper or a Kimwipe over the open port on the objective turret.
10. Using the fine rotation knobs on gimbal mount G3 center the laser beam in the objective turret port.
11. Replace the paper on the optical port and check the position of the beam. Iterate steps 8 - 10 until the beam is centered on both the optical port and objective turret.
12. Remove the paper, replace the objective, and place a microfluidic device on the sample holder. Focus on the fluidic channels and check the beam shape. Further adjustment may be necessary. Attempt to make the necessary corrections using only the mirrors from steps 8 and 10. If this is unsuccessful, return to step 9 or 5 and repeat.
13. Once the laser is successfuly aligned, remove the neutral density filter.

Appendix B

MATLAB Image Processing for Droplet Size Calculations

Two of the greatest strengths of using microfluidics to generate emulsions are the monodispersity of produced droplets and precise control of droplet size. To characterize device performance and repeatibility, droplets must be measured after production. This is easily accomplished using a fast camera to image the droplets flowing on-chip. The digital images are then analyzed and drop sizes determined.

The challenges for digital image processing of the droplets are threefold:

1. Due to index mismatch with the continuous phase, droplets appear with a dark edge and light center. As droplets contact one another or features in the channel, the dark edges combine and make thresholding difficult.

2. Defocusing the image to enhance the droplets' dark edges and bright centers results in an artificial enlargement of the droplet diameters.

3. Droplets may not be perfectly spherical in the plane of view, requiring some interpolation of their equivalent diameters.

B.1 MATLAB Code

The following MATLAB code performs analysis on digital images of droplets. The code requires a reference image containing the field of view with no droplets present. For fast camera image sequences of moving droplets, this reference is best obtained by generating a z-projection of the entire image sequence using an average or median intensity projection. The analysis code has been optimized to process images containing sparse droplets, such as those flowing in a microchannel or sufficiently diluted in an imaging chamber.

The code first performs a background subtraction, thus removing objects that are static in all frames and highlighting the droplets. The droplet features are processed to form complete annuli, are thresholded, and then are eroded. These smaller regions are used to find the droplet centers. Droplet size is determined from a distance transform on the thresholded image. For each image, the code overlays the located droplet centers and circumferences on the image. Following analysis of all images, the code produces a histogram of the drop sizes with a Gaussian fit, saves the center positions and radii, and can plot all center positions on the background reference image.

Digital Image Processing Using MATLAB, by Gonzalez, et al. was an immensely useful reference during development of this code [139].

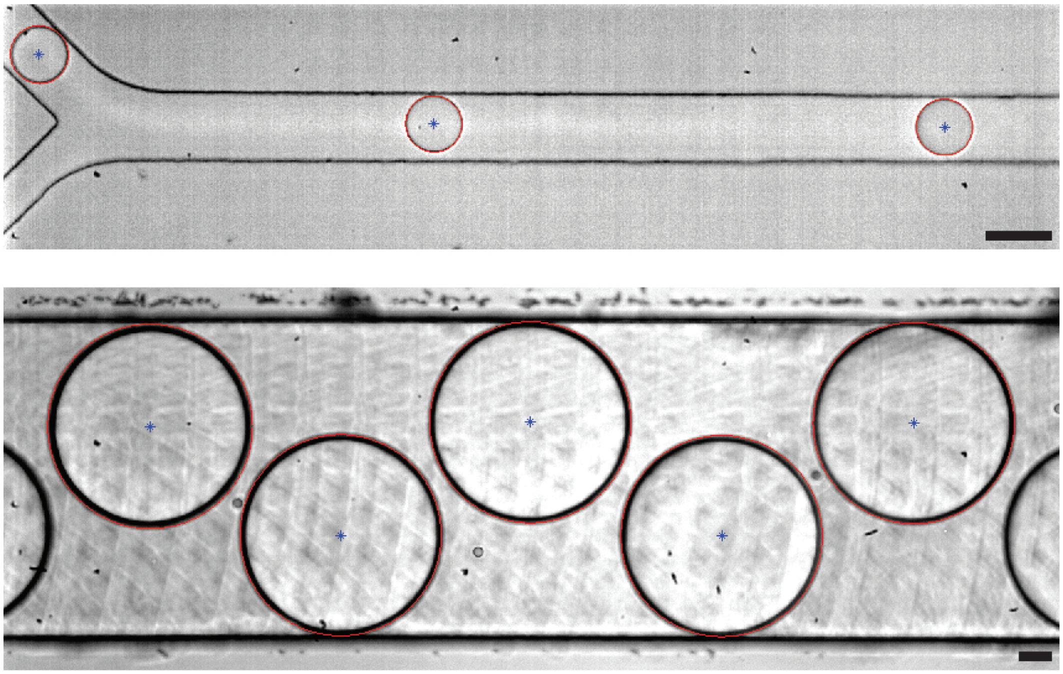

Figure B.1: Images showing output droplet centers (blue) and radii (red) overlaid on input image frame. Scale bar in each image represents 50 μm.

B.1.1 Main Processing Script

```
% UPDATE EXPECTED NUMBER DROPS PER FRAME AND DROP SIZE HERE
%-----------------------------------------------------------------
mDrops = 20; %maximum drops per frame
minSize = 20; %minimum size filter for drop area, in pixels
%-----------------------------------------------------------------

warning(’off’,’Images:initSize:adjustingMag’);

startFolder = uigetdir(pwd,’Select topmost directory’);
[upperPath,deepFolder,~] = fileparts(startFolder);
listing = dir(strcat(startFolder,’\*.tif’));
numFiles = length(listing);
imgOne = imread(strcat(startFolder,’\’,listing(1).name));
[I rect] = imcrop(imgOne);
close(gcf);
```

```
rect = round(rect);

[refName,refPath,~] = uigetfile(strcat(upperPath,...
'\',deepFolder,'\','*.tif'));
ref = imread(strcat(refPath,refName));
refCrop = ref(rect(2):rect(2)+rect(4)-1,rect(1):rect(1)+rect(3)-1);
% refCrop = zeros(rect(4),rect(3));

dropsPerFrame = mDrops;
radii = zeros(numFiles,dropsPerFrame);
centerPos = zeros(numFiles,dropsPerFrame,2);

for ii=1:numFiles;
    try
        tempRads = zeros(20,1);
        tempCents = zeros(20,2);
        loopRect = rect;
        img = imread(strcat(startFolder,'\',listing(ii).name));
        imgCrop = img(loopRect(2):loopRect(2)+loopRect(4)-1,...
         loopRect(1):loopRect(1)+loopRect(3)-1);

        [imgBW,centers,rads] = dropSeparate(imgCrop,refCrop,minSize);

        imshow(imgCrop); hold on;
        set(gcf,'Name',strcat('Frame #',num2str(ii)),...
         'NumberTitle','off');
        plot(centers(:,1),centers(:,2),'b*');
        for jj = 1:size(centers,1)
            [xp,yp] = circlePts(centers(jj,1),centers(jj,2),rads(jj));
            plot(xp,yp,'r');
        end
        hold off
        pause(0.01)

        if length(rads) < dropsPerFrame;
            maxDrops = length(rads);
        else
            maxDrops = dropsPerFrame;
        end

        for jj = 1:maxDrops;
            tempRads(jj) = rads(jj);
```

```
            tempCents(jj,:) = centers(jj,:);
        end
        radii(ii,:) = tempRads;
        centerPos(ii,:,:) = tempCents;

    catch err
        if ~isempty(err)
            err
            listing(ii).name
        end
    end
end
allRadii = reshape(radii,numFiles*dropsPerFrame,1);
allCenters = reshape(centerPos,numFiles*dropsPerFrame,2);
yy = 1;
for zz = 1:length(allRadii)
    if radii(zz) > 2
        finalRad(yy) = allRadii(zz);
        finalCenters(yy,:) = allCenters(zz,:);
        yy = yy + 1;
    end
end

minX = min(allCenters(:,1));
maxX = max(allCenters(:,1));
xPlot = minX:maxX;
yPlot = zeros(1,length(xPlot));
ePlot = zeros(1,length(xPlot));
x = allCenters(:,1);
y = allCenters(:,2);
yy = 1;
for zz = 1:length(xPlot)
    xIndex = find(x == xPlot(zz));
    yTemp = y(xIndex);
    yPlot(zz) = mean(yTemp);
    ePlot(zz) = std(yTemp);
end

save(strcat(startFolder,'\',deepFolder,'_feb01.mat'),...
'finalRad','finalCenters','-mat');

figure; imshow(refCrop); hold on;
```

```
plot(allCenters(:,1),allCenters(:,2),'bo','MarkerSize',1);
hold off;

figure; errorbar(xPlot,yPlot,ePlot,'mo'); axis tight;

summary = [xPlot' yPlot' ePlot'];
xlswrite(strcat(startFolder,'\',deepFolder,'dropPosition.xls'),...
summary);
```

B.1.2 Supporting Functions

```
function [D3,centers,radii] = dropSeparate(img,ref,minSize)
%DROPSEPARATE Droplet centers and radii.
%   [D3,CENTERS,RADII]=DROPSEPARATE(IMG,REF) takes an input and
%   background image reference to determine the size of drops
%   within the input image.  After background subtraction and
%   filtering, a distance transform is used to determine drop radius
%   and regionprops is used to determine the center.  These values
%   are output as arrays, along with the final binary image used to
%   determine droplet centers.  Drops in contact with device walls
%   or passing through strong shadows will not be detected.
%   Following background subtraction, the droplet must appear as
%   a complete white ring with a dark center, otherwise it will not
%   be found by this program.  To check, output or show the variables
%   "imgSub" and "imgBW".
%-----------------------------------------------------------------
% Created By: Donald M. Aubrecht
% Date Modified: 31 January 2012
% Version: 1.0
%-----------------------------------------------------------------

se = strel('disk',4); %struct element of opening connected regions

imgSub = ref - img; %get white droplet edges on black background
imgBW = im2bw(imgSub,0.5*graythresh(imgSub));
imgThick = bwmorph(imgBW,'thicken',1);
imgBridge = bwmorph(imgThick,'bridge');
imgThin = bwmorph(imgBridge,'thin',1);
imgFill = imfill(imgThin,'holes'); %fill in droplet centers
```

```
imgOpen = bwareaopen(imgFill,minSize); %adjust for droplet size

D = double(bwdist(~imgOpen)); %distance transform; use for radius
D2 = D >(0.8*max(D(:))); %threshold to separate touching droplets
D3 = imclearborder(D2); %get rid of anything touching the edge

[L,num] = bwlabel(D3); %find all drop regions
S = regionprops(L,'Centroid','Eccentricity');
propSize = size(S);

if propSize(1) ~= 0 %only analyze if droplets/regions in frame
    dropNum = 1;

    for jj = 1:num
        center = round(S(jj).Centroid);
        if (S(jj).Eccentricity <= 0.9) %analyze mostly spherical obj
            radii(dropNum) = round(D(center(2),center(1)));
            centers(dropNum,:) = center;
            dropNum = dropNum + 1;
        else %ignore things that are far from spherical
            radii(dropNum) = 0;
            centers(dropNum,:) = [0,0];
            dropNum = dropNum + 1;
        end

    end

else %output zeros if no droplets to analyze
    radii(1) = 0;
    centers(1,:) = [0,0];
end

end

%-----------------------------------------------------------------

function [xpts,ypts] = circlePts(x,y,rad)
%CIRCLEPTS determine points on a circle
%    [XPTS,YPTS]=CIRCLEPTS(X,Y,RAD) accepts the x and y
%    coordinates for the circle center and its radius for
%    inputs.  The function returns two arrays with the x and y
%    coordinates of all points that lie on the circumference.  The
```

```
%    function is set to use an angular step size of 0.01 radians.
%    This can be changed using variable ASTEP.
%-----------------------------------------------------------------
% Created By: Donald M. Aubrecht
% Date Modified: 31 January 2012
% Version: 1.0
%-----------------------------------------------------------------

aStep = 0.01;
a=[0:aStep:2*pi];
xp=rad*cos(a);
yp=rad*sin(a);
xpts = x+xp;
ypts = y+yp;
end
```

Appendix C

Custom Reflection Microscope and Thermal Stage

Providing thermal control of microfluidic devices is conceptually simple, but difficult to implement. Most microfluidic operations require optical imaging of flows on the device. This is commonly achieved using a transmission microscope, as the devices and reagents are translucent. High quality optical images at high magnification and frame rate are achieved, providing excellent image sequences of short timescale processes at length scales of 1-100 μm.

Incorporating thermal control of microfluidic devices requires placing a heat exchanger and temperature sensor in contact with the microfluidic device. For PDMS-glass devices, the simplest orientation is to thermally-couple a stage to the glass portion of the device, as this is the smallest distance for heat diffusion to and from the fluidic channels. The thermal stage prevents imaging via transmission microscopy unless an imaging port is provided in the stage, as discussed in Section 3.2. However, use of a port through the thermal stage increases the temperature gradients on the microfluidic device and limits the observable field. If these two effects must be mitigated, the thermal stage must be solid and imaging therefore can only be accomplished via reflection microscopy with illumination through the objective.

The construction of this custom experimental microscope is described in two parts: the reflection microscope coupled to a fast camera above the microfluidic device, and the thermal XYZ stage below the device. Each of the two parts can be separately modified and adapted to particular experiments.

C.1 Reflection Microscope

Imaging of droplets in microfluidic devices is straightforward, but has several key requirements. The droplets are large enough to be imaged by most standard air objectives, but the short timescale of on-chip processes necessitates short exposures and high frame rates to capture crisp image sequences of processes such as droplet creation, droplet coalescence, and fluid flows in the microchannels. Short exposure times require intense illumination: the largest challenge for reflection microscopy. High frame rates are achieved using a fast camera, in this case a Phantom v7.3. Small vibrations can cause noticeable frame-to-frame motion in images shot at high frame rates, thus necessitating a microscope free of vibration.

We initially use an InfiniTube (Infinity Photo-Optical Company) attached to the C-mount adapter on the Phantom v7.3 for imaging. A 10x Mitutoyo infinity-corrected objective (Edmund Optics Inc.) images the microfluidic device, and an OSL1 high intensity fiber coupled light source (Thorlabs Inc.) provides bright field illumination. The InfiniTube is connected to a 1.5” diameter Thorlabs optical post, which is fixed to a floating optical table. Though this setup is functional, it suffers from substantial vibrations and does not provide images of sufficient quality. The magnitude of frame-to-frame image center-of-mass motions are plotted in Figure C.1 as black data points.

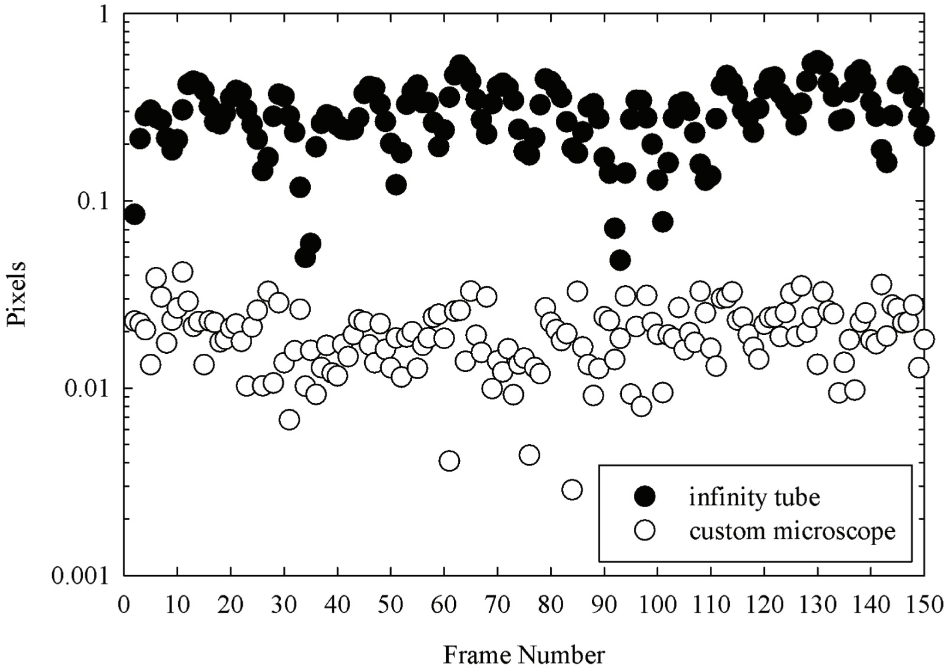

Figure C.1: Plots show motion of the image frame's center-of-mass relative to the first frame of each movie. Image sequences were taken with the same 5x Mitutoyo objective and Phantom v5 camera for both experiments. Though the center of mass moves less than a pixel in images taken with the InfiniTube, motion of individual objects within images is visible by eye and too severe for image analysis. Vibration and motion of objects within images taken with the final custom microscope is not visible by eye.

To minimize motion of objects in the images, three sources of vibration are addressed. First, since the camera weighs 6 lbs. and is sitting unsupported on top of the InfiniTube, the base support is changed from a 1.5" optical post to a 95mm construction rail (XT95, Thorlabs Inc.) connected directly to the camera body via a custom mounting plate. The XT95 extrusion and the floated optical table damp out any mechanical vibrations that couple into the camera from surroundings.

The large, heavy Mitutoyo objective hanging on the end of the InfiniTube couples vibration from air handlers and other mechanical equipment in the room. Despite adjusting and tightening all sections of the InfiniTube, these vibrations could not be eliminated. Trading the InfiniTube for a standard 4 rail 30 mm optical cage system (Thorlabs Inc.) minimizes this source of vibration. To attach the cage system to the Phantom v7.3, a custom adapter is designed for the front of the Phantom camera. Replacing the camera's C-mount, this adapter provides attachment points for the optical cage. Dimensions and drawings of this plate are shown in Figure C.2.

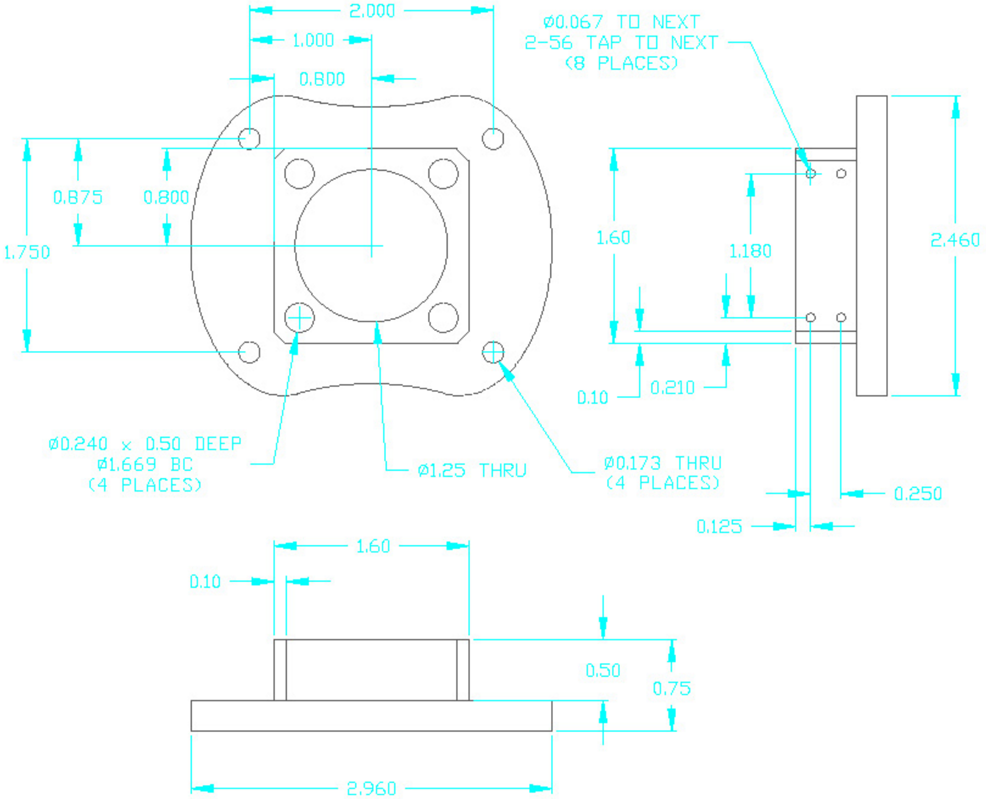

Figure C.2: Dimensioned drawing of adapter plate for Phantom camera to Thorlabs 30mm optical cage. Dimensions are in inches.

Finally, the illumination source is changed. The fiber light's cooling fan couples vibration through the optical fiber into the imaging optics. The light and fiber are replaced with a heat sinked Vollong 5W high power white LED (superbrightleds.com) driven by a Buckplus 7023, 1000 mA LED driver with external 5kΩ potentiometer control (Digikey). The LED gives better illumination and eliminates all vibration from the optics. An image of the final microscope assembly is shown in Figure C.3.

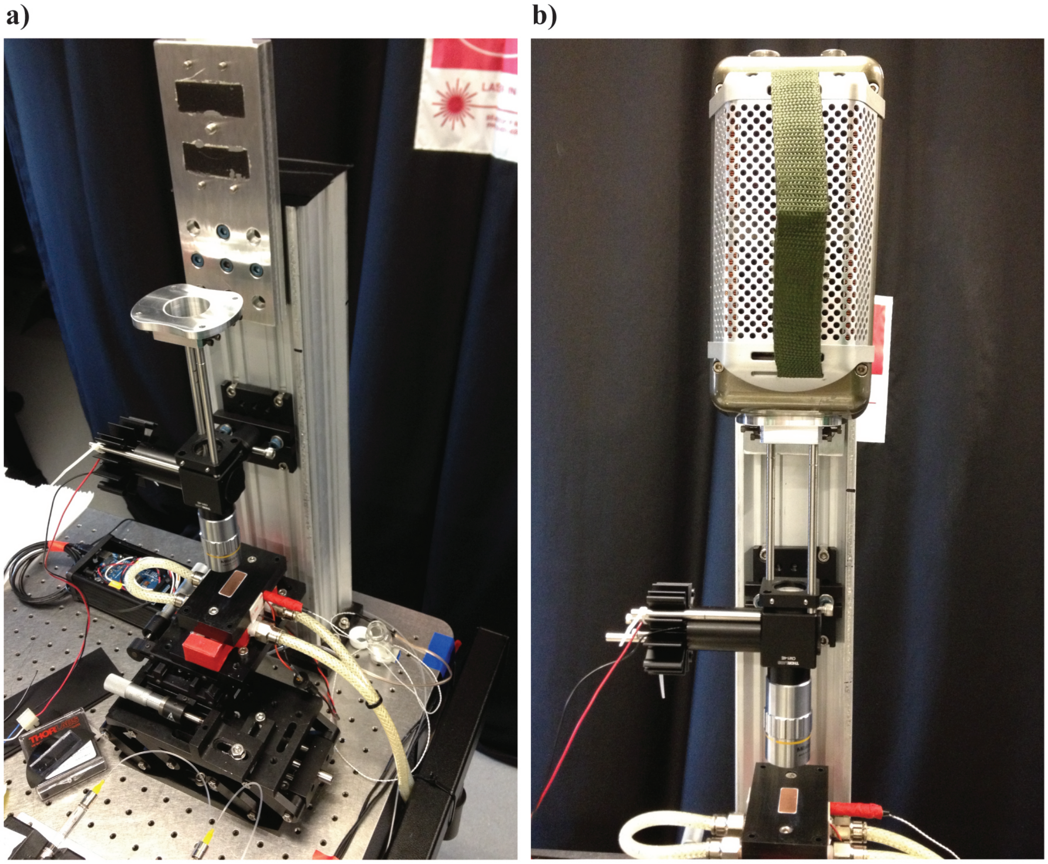

Figure C.3: Final assembly of the reflection microscope. **(A)** Microscope without fast camera attached. The plate adapting the camera mounts to the 95mm rail can be seen at the top of the image. **(B)** Microscope with Phantom fast camera attached. The thermal XYZ stage is seen below the objective in both images.

C.2 Thermal Stage

To provide precise temperature control of the stage and microfluidic device, a Peltier-cooled copper stage is constructed. The stage is insulated, allowing only the surfaces in contact with the microfluidic device and the Peltier to be exposed copper. Additional exposed copper surfaces serve as condensation sites for water vapor, leading to icing of the stage and loss of temperature control.

Figure C.4 is an exploded view of the thermal stage assembly. An upper copper block sits encased by a rectangular Delrin piece. The top surface of these pieces are where the microfluidic device will sit. The exposed copper surface is sized to engulf a full microfluidic channel. In this case, the exposed surface measures 0.5 inches by 1.25 inches. The underside of this copper block contacts the top surface, or cold side, of the Peltier device. The bottom, or hot side, of the Peltier sits in contact with the other copper block. Flipping the Peltier allows for heating of the microfluidic channel. The bottom copper block includes fluid channels and quick connect fittings through which cooling or heating water is flowed. The entire assembly is held together by bolts that pass through the Delrin block into tapped holes in the bottom copper block, thus sandwiching the upper copper block and Peltier in place. Silicone heat sink compound (Chemplex 1381) is applied at both Peltier/copper interfaces as well as the microfluidic device/copper interface.

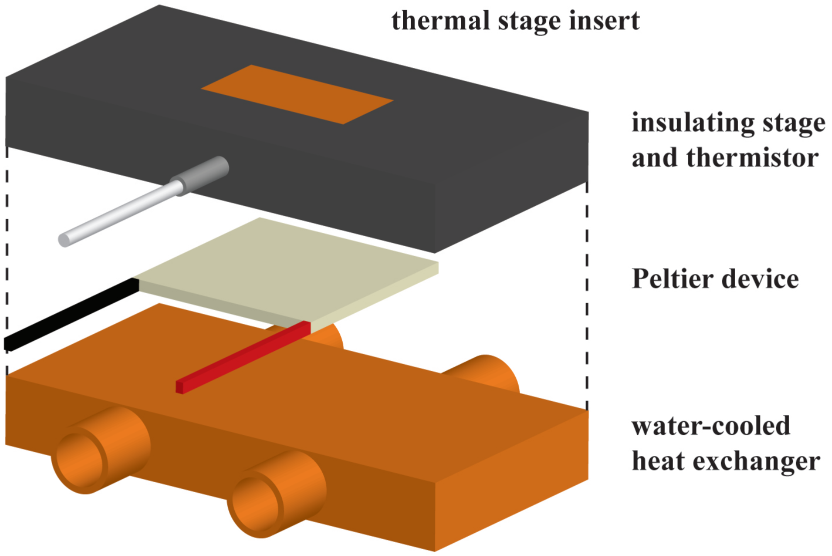

Figure C.4: Exploded assembly schematic of Peltier-cooled thermal stage.

The entire thermal stage assembly shown in Figure C.4 is affixed to a XY translation stage. The XY stage is mounted on a Thorlabs L490 lab jack for Z positioning. The complete thermal and translation stage assembly is aligned beneath the imaging system detailed in Section C.1 and mounted to the floated optical table. The complete assembly is shown in Figure C.3.

Control of the Peltier is achieved through a MATLAB GUI to Arduino microcontroller. The custom GUI provides user input for gains, set points values, and data logging. MATLAB-Arduino communication is achieved through the Arduino's USB-to-serial port converter. Temperature control is provided by thermistor feedback of the stage temperature to a PID routine on the microcontroller. The Arduino PID Library v1.0.1 in combination with the Arduino MATLAB class are used for control and communication. The on-board Arduino ADC provides insufficient temperature resolution for precise control, so a 24-bit ADC circuit with a dedicated precision voltage reference is included on the custom circuit board containing the Peltier power circuit. This circuit is described in Section C.2.1.

Figure C.5 shows the response and thermal stability of the stage and control circuit. Provided with an adequate flow of cooling water, the Peltier is capable of supporting a 20-25°C temperature difference below ambient. Decreasing the cooling water temperature allows for an even great ΔT. Stability of 0.1°C is maintained for several hours.

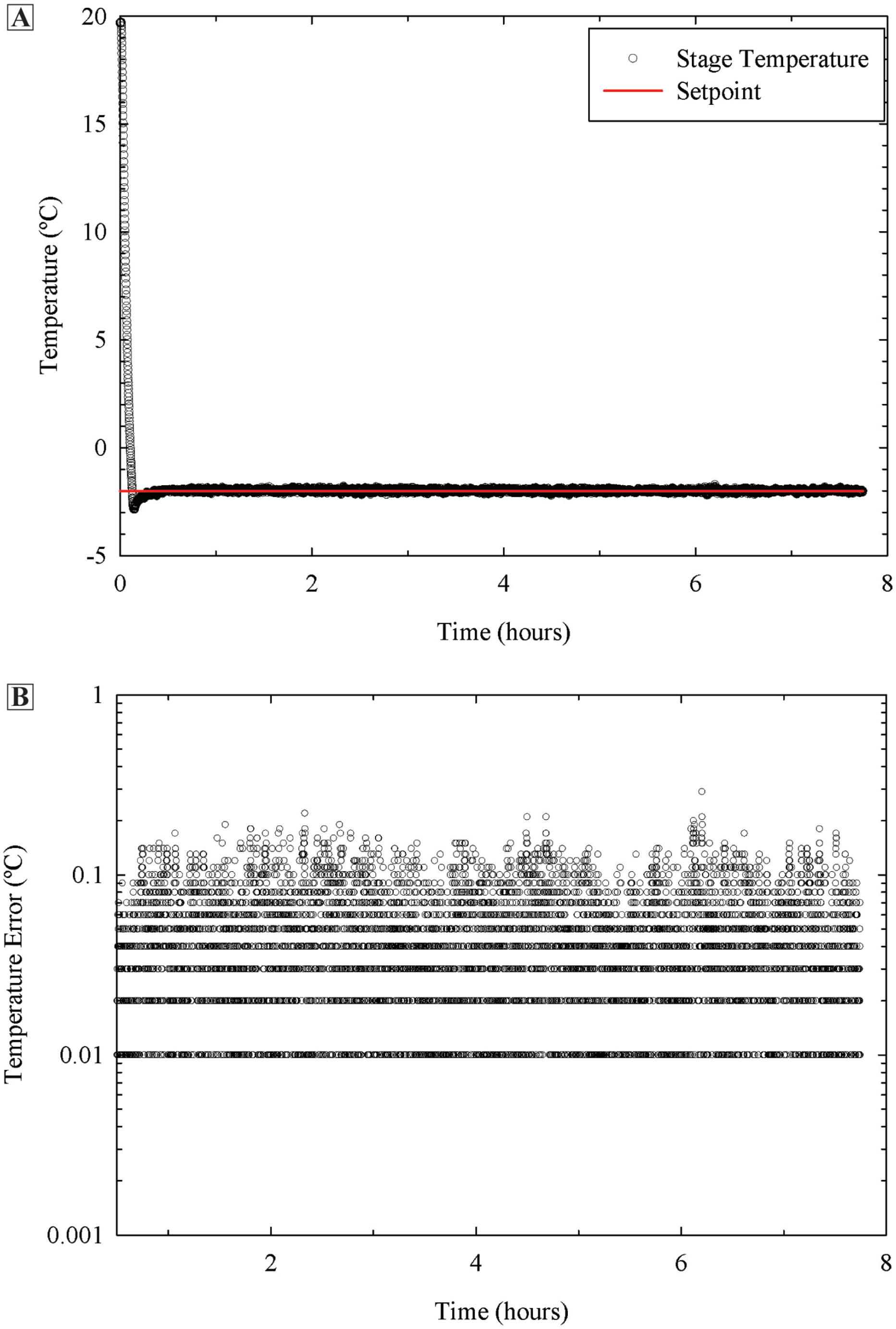

Figure C.5: **(A)** Stage temperature set point and measured temperature over nearly eight hours. **(B)** Magnitude of stage temperature error once set point has been reached. The time axis begins at 0.5 hour to avoid the time required to initially cool the stage to the set point.

C.2.1 Circuit Board Design

After determining that the onboard ADC and power circuits of the Arduino Mega 2560 provide insufficient temperature resolution and power to the Peltier, we design a custom circuit board to interface between the stage thermistor, the Arduino, and the Peltier device. The two-layer board is designed using the ExpressSCH and ExpressPCB software packages (ExpressPCB). Circuit schematics are showing in Figure C.6 and the board layout is shown in Figure C.7. Table C.1 lists the parts required for construction of these circuits.

The Arduino Mega 2560 contains a 10-bit ADC circuit for each of it's analog inputs. Utilizing the 5 V range of the analog inputs yields a voltage resolution of roughly 5 mV. With the original temperature sensing circuit using an RTD and voltage amplification circuit, a temperature resolution of 0.5°C is expected. However, this level of resolution is limited by the discretization limit of the Arduino's 10-bit ADC. To improve the discretization and eliminate the need for an amplification circuit, a custom ADC circuit is designed. The circuit utilizes a precision 1.25 V reference supply and a 24-bit ADC chip communicating via SPI protocol with the Arduino Mega 2560. This circuit reads the midpoint voltage from a 10 kΩ thermistor (GE) in a voltage divider arrangement with a 0.01% precision 10 kΩ resistor. When triggered via SPI, the voltage reference and ADC are enabled, allowed to stabilize for 1 microsecond, and then the voltage value is read by the 24-bit ADC and sent to the Arduino. The Arduino records the value, disables the external circuit, and returns the value to the MATLAB GUI. The PID controller utilizes the same protocol for reading the input temperature. This circuit has a theoretical temperature resolution of 0.000005°C, though a more practical limit of 0.01°C is observed during experiments.

Following the temperature measurement, the Arduino PID library calculates an 8-bit

PWM value that is output to the Peltier power circuit. The PWM value is limited to a maximum of 245 to prevent saturation of the Peltier and loss of temperature control. Power to the Peltier is provided by a 12 V, 6.3 A power supply switched by a logic-driven FET, whose gate is connected to the output PWM signal.

With this control arrangement, we are able to take temperature readings and calculate control outputs at a maximum rate of roughly 1 Hz. The primary limiting component is execution speed of the Arduino Mega 2560 and data transfer over the SPI interface from the external ADC. However, we do not experience any adverse effects on temperature regulation, as demonstrated in Figure C.5.

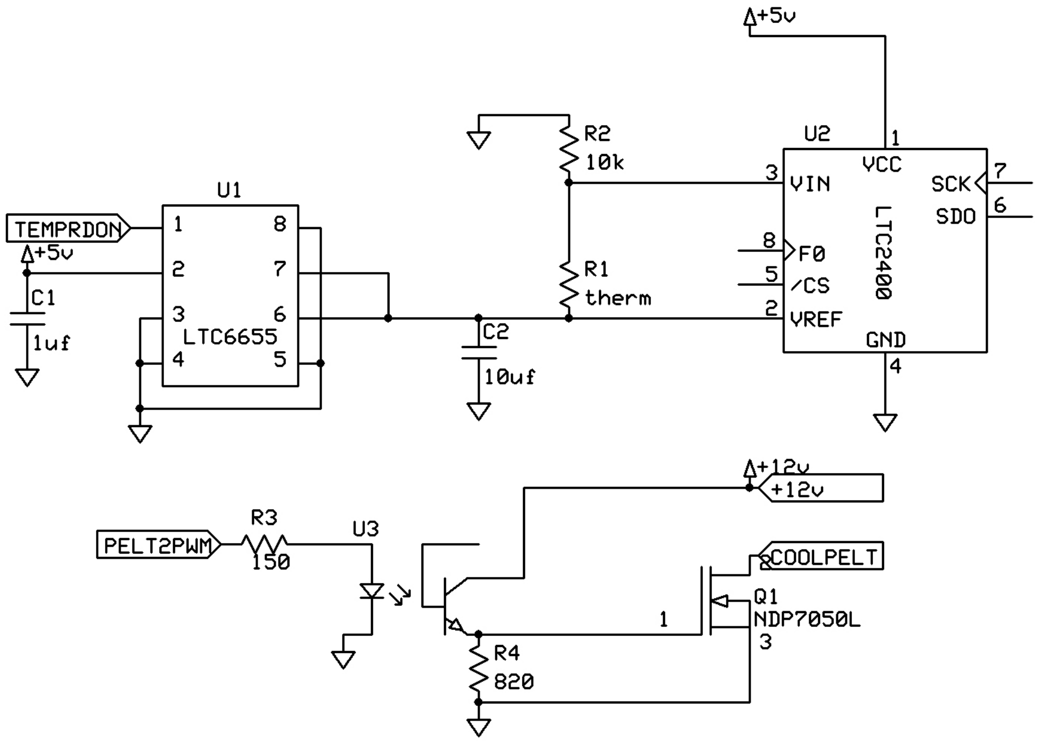

Figure C.6: Circuit design for temperature control. Upper circuit is controlled by the Arduino microcontroller for reading resistance of the precision thermistor. Lower circuit provides power to the Peltier and is driven by a PWM signal from the Arduino.

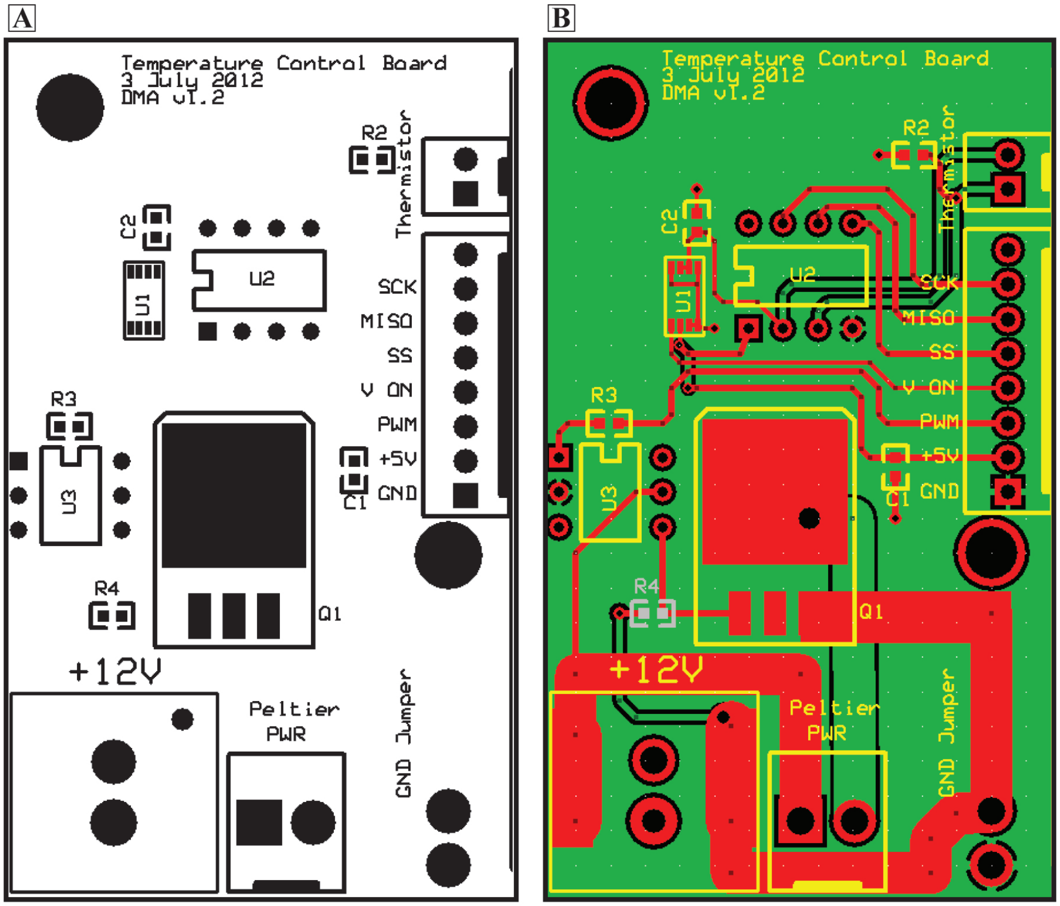

Figure C.7: **(A)** Labels printed on top of circuit board. **(B)** Electrical trace layout for the two layer board. Green traces and planes are on the bottom of the circuit board. Red traces are on the top of the circuit board. Yellow lines correspond to the labels shown in panel (A).

Table C.1: List of parts required for Peltier controller circuit. Reference labels on the circuit board and part numbers for Digikey are included.

Reference	Quantity	Digikey P/N	Description
U1	1	LTC6655BHMS8-1.25#PBF	1.25V reference
U2	1	LTC2400CS8#PBF	24-bit ADC
U3	1	CNY173M	70V, 50mA optocoupler
Q1	1	NDB7060LCT	logic driven FET
R1	1	235-1060	10k thermistor
R2	1	RNCF0603TKY10K0CT	10kΩ 0.01%, SMT-0603
R3	1	P150GCT	150Ω, SMT-0603
R4	1	P820GCT	820Ω, SMT-0603
C1	1	587-1248-1	1μF, SMT-0603
C2	1	587-2248-1	10μF, SMT-0603
	1	WM4620	2 pin header, 0.156”
	1	WM4400	2 pin header, 0.156”
	2	WM2122	2 pin housing, 0.156”
	1	WM2613	2 pin housing, 0.100”
	1	WM2618	8 pin housing, 0.100”
	1	WM2706	8 pin header, 0.100”
	1	WM4200	2 pin header, 0.100”
	10	WM2302	0.156” crimp terminal
	20	WM1114	0.100” crimp terminal
	1	CP-002BHPJCT	2.5mm power jack
	1	A9406	IC socket for 6pos DIP
	1	A32361	IC socket for 8pos DIP
	1	309-1098	adapter 8-SOIC to 8-DIP

C.2.2 Temperature Control GUI and Arduino script

The graphical user interface is developed using MATLAB’s GUIDE helper application. A screenshot of the interface at initialization is shown in Figure C.8. The interface includes controls for setting gains and the temperature set point, and plotting and logging data. Control of syringe pumps for fluid flow is also integrated with this interface. The code relies on a modified version of the Arduino class for MATLAB, containing added functionality for updating gains and set points.

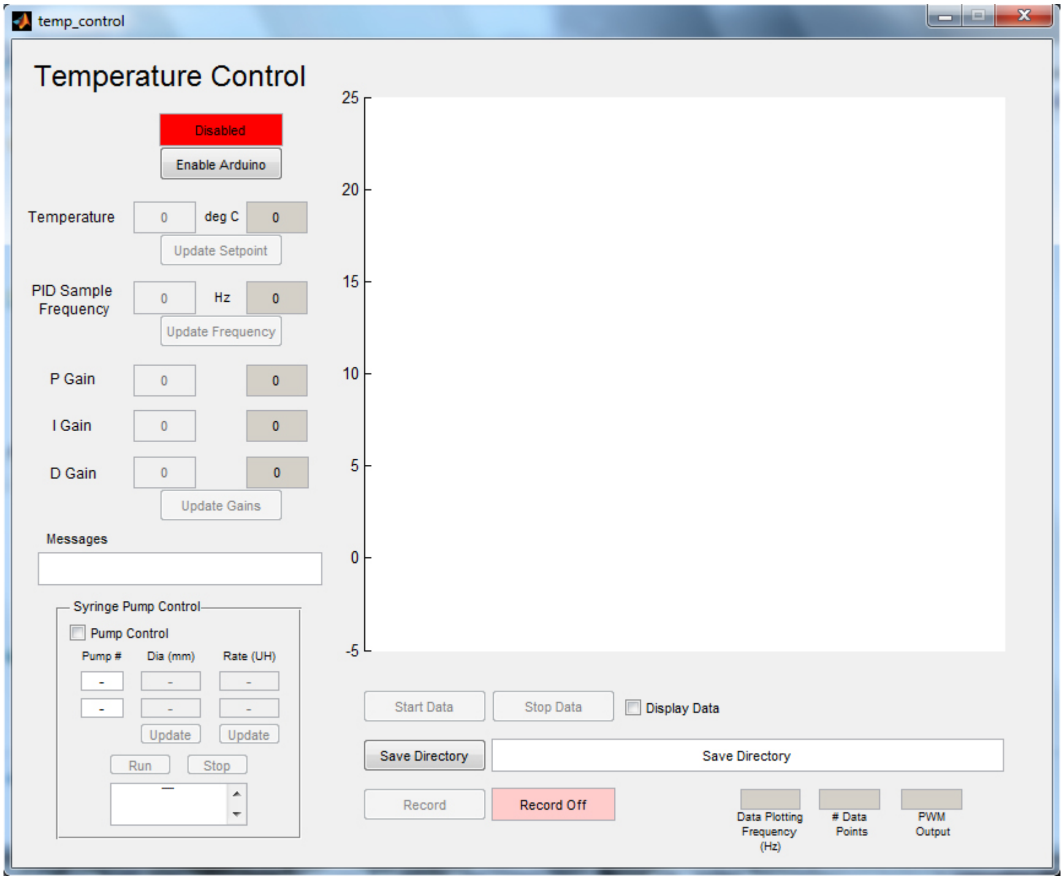

Figure C.8: Screenshot of MATLAB GUI for control of thermal stage and syringe pumps. The interface provides controls for setting gains and set points, visualizing data, and recording data.

The following code is the script for the Arduino Mega 2560 microcontroller, providing temperature control and communication with a MATLAB interface. The script is a modified combination of the MATLAB Arduino server program, Arduino PID library, and SPI communication.

```
/*
 Temperature Control

 This program is designed to monitor a thermistor and provide a PWM
 signal to power a Peltier device.  The program can output
 temperature to MATLAB.
```

```
 Created 27 August 2011
 By Donald Aubrecht
 Modified 25 Sept 2012 (v4.58)
 for use with thermistor temperature sensor

 */

#include <PID_v1.h>
#include <SPI.h>
#define peltierPin 9  //output pin for the Peltier driver

/* define the two pins used for the SPI slave select function
controlling each LTC2400 ADC  */
const int Vrefon = 46;  //pin to enable thermistor ref. voltage
const int slaveSelectT1 = 48;
const int slaveSelectT2 = 49;
const int slaveSelectPin = 53;  //default SS pin in Mega
const int MISOpin = 50;  //default MISO pin in Mega

double SetpointT = 24;  /*temperature setpoint (-99 to +99
 with 0.1 degC resolution limited by serial code below)*/
int sampleT = 1000;  //iteration time of PID calculation in msec
/*R-T const  (T = 1/(a+b*ln(R)+c*ln(R)^3)) */
double a = 0.001124495;
double b = 0.000234835;
double c = 0.000000085;

double discreteVoltage;  //value read from external ADC
double Vratio;  //converted value from external ADC
double R2 = 10000;  //value of R2 in voltage divider
double R;  //resistance value calculated from ADC reading
double Input, Output;  //output from PID control loop
double P = 90;  //proportional gain
double I = 0.25;  //integral gain
double D = 10;  //derivative gain
String strSP, strPID;
double Setpoint = SetpointT;  //assign PID pass-through variable
int sign = 0;  //initialize setpoint change sign value
int digit = 0;  //initialize setpoint change digit value
double newSP = 0;  //initialize setpoint change value
int gChange = 0;  //initialize gain to change holder
```

```
double newG = 0;  //initialize gain change value
double newT = 0;  //initialize sample time change value
unsigned long time;  //initialize time variable for benchmarking

//specify links and initial tuning parameters
PID tempPID(&Input, &Output, &Setpoint, P, I, D, REVERSE);



void setup()  {
  /* initialize serial communication */
  Serial.begin(115200);

  /*slow down the PWM clock on pins 45 and 46 see
  http://www.arduino.cc/cgi-bin/yabb2/YaBB.pl?num=1235060559/15
  and http://www.arduino.cc/playground/Main/TimerPWMCheatsheet
  for reference */
  TCCR5B = TCCR5B & 0b11111000 | 0x05;

  /* Make sure all pins are put in high impedence state and
    that their registers are set as low before doing anything.
    This puts the board in a known (and harmless) state     */
  int i;
  for (i=0;i<20;i++) {
    pinMode(i,INPUT);
    digitalWrite(i,0);
  }

  /* set the slaveSelect pins as outputs */
  pinMode (slaveSelectPin, OUTPUT);
  pinMode (slaveSelectT1, OUTPUT);
  pinMode (slaveSelectT2, OUTPUT);

  /* initialize SPI */
  SPI.begin();
  /* Turn off both ADCs */
  digitalWrite(slaveSelectT1,HIGH);
  digitalWrite(slaveSelectT2,HIGH);

  /* declare the peltierPin as an OUTPUT */
  pinMode(peltierPin, OUTPUT);
  tempPID.SetSampleTime(sampleT);  //set the sampling time
```

```
  tempPID.SetMode(AUTOMATIC); //turn on PID control
}


void loop()  {
  /* variables declaration and initialization                */
  static int s = -1;  //initialize state variable
  static int pin = 1;  //initialize pin variable

  int val = 0;  //initialize serial read value variable

  static int  ADCn = 1;  // ADC input number
  long int  ADCval = 0;  // placeholder for ADC return
  byte b0;
  byte sig;  // sign bit flag



  //handle serial port commands
  if (Serial.available() > 0 ) {
    val = Serial.read();
    switch (s) {
      case -1:
      if (val>47 && val<95) {
        /* the first received value indicates the mode
          49 is ascii for 1, ... 90 is ascii for _
          s=90 is query script type
          s=350 is setpoint read; s=360 is setpoint write;
          s=370 is PID gains read;   s=380 is PID gains write
          s=390 is sample time read; s=400 is sample time write
          s=410 is PID output read; s=420 is ADC read
          s=430 is PID temp input read;
          */
        s=10*(val-48);
      }
      else {
        s=-1;  // keep switch in initial state unless command given
      }
      break;  // s=-1 (initial state) taken care of
```

```
/* s=90 means Query Script Type
(4 temperature)   */
case 90:
if (val==57) {  // send script type via serial
  Serial.println(4);
}
else if (val==58) {  // send script ver number
  Serial.println(4.58);
}
s=-1;  // we are done so next state is -1
break;  // query script type finished



// s=350 means SETPOINT READ
case 350:
if (val==57) {
  if (Setpoint < 0) {
    Serial.println(Setpoint);
  }
  else {
    Serial.println(Setpoint);
  }
}
s=-1;  // we are done so next state is -1
break;  // setpoint read finished



// s=360-363 means SETPOINT WRITE
case 360:
/* the second received value indicates the sign of the
  new setpoint value                                   */
if (val>42 && val <46) {  // determine sign
  if (val==45) {
    sign = -1;
  }
  else if (val==43) {
    sign = 1;
  }
  s=361;  // next we will need to get 10's digit from serial
}
```

```
      else {
        s=-1;  // if value is not a sign then return to -1
      }
      break;  // s=360 taken care of
      case 361:
      /* get 10's digit */
      if (val>47 && val <58) {
        digit=val-48;
newSP = digit*10;
        s = 362;  // get 1's digit from serial
      }
      else {
        s=-1;  // if value is not a number then return to -1
      }
      break;  // s=361 taken care of
      case 362:
      /* get 1's digit */
      if (val>47 && val <58) {
        digit=val-48;
newSP += digit;
        s = 363;  // get 1/10's digit from serial
      }
      else {
        s=-1;  // if value is not a number then return to -1
      }
      break;  // s=362 taken care of
      case 363:
      /* get 1/10's digit */
      if (val>47 && val <58) {
        digit=val-48;
newSP += digit*0.1;
        s=364;  // we are done so next state is -1
      }
      else {
        s=-1;  // if value is not a number then return to -1
      }
      break;  // s=363 taken care of
      case 364:
      /* get 1/100's digit */
      if (val>47 && val <58) {
        digit=val-48;
Setpoint = (newSP + digit*0.01)*sign;
```

```
        s=-1;  // we are done so next state is -1
      }
      else {
        s=-1;  // if value is not a number then return to -1
      }
      break;  // setpoint write finished



      // s=370 means PID GAINS READ
      case 370:
      if (val==57) {
        Serial.print("Pgain=");
        Serial.print(tempPID.GetKp());
        Serial.print("Igain=");
        Serial.print(tempPID.GetKi());
        Serial.print("Dgain=");
        Serial.println(tempPID.GetKd());  // send values via serial
      }
      s=-1;  // we are done so next state is -1
      break;  // PID gains read finished

      // s=380-384 means PID GAINS WRITE
      case 380:
      /* the second received value indicates which gain to
        change p(val=112), i(val=105), d(val=100)          */
      if (val==100 || val==105 || val==112) {
        gChange=val;  // calculate gain to change
        s=381;  // get first digit of gain
      }
      else {
        s=-1;  // if value is not a pin then return to -1
      }
      break;  // s=380 taken care of
      case 381:
      /* get 100's digit */
      if (val>47 && val <58) {
        digit=val-48;
newG = digit*100;
        s = 382;  // get 10's digit from serial
      }
      else {
```

```
        s=-1;  // if value is not a number then return to -1
      }
      break;  // s=381 taken care of
      case 382:
      /* get 10's digit */
      if (val>47 && val <58) {
        digit=val-48;
newG += digit*10;
        s = 383;  // get 1's digit from serial
      }
      else {
        s=-1;  // if value is not a number then return to -1
      }
      break;  // s=381 taken care of
      case 383:
      /* get 1's digit */
      if (val>47 && val <58) {
        digit=val-48;
newG += digit;
        s = 384;  // get 1/10's digit from serial
      }
      else {
        s=-1;  // if value is not a number then return to -1
      }
      break;  // s=382 taken care of
      case 384:
      /* get 1/10's digit */
      if (val>47 && val <58) {
        digit=val-48;
newG += digit*0.1;
        s = 385;  // get 1/100's digit from serial
      }
      else {
        s=-1;  // if value is not a number then return to -1
      }
      break;  // s=383 taken care of
      case 385:
      /* get 1/100's digit */
      if (val>47 && val <58) {
        digit=val-48;
newG += digit*0.01;
        if (gChange==112) {
```

```
          P = newG;
        }
        else if (gChange==105) {
          I = newG;
        }
        else if (gChange==100) {
          D = newG;
        }
        tempPID.SetTunings(P,I,D);
        s=-1;  // we are done so next state is -1
      }
      else {
        s=-1;  // if value is not a number then return to -1
      }
      break;  // PID gains write finished



      // s=390 means SAMPLE TIME READ
      case 390:
      if (val==57) {
        Serial.println(sampleT);
      }
      s=-1;  // we are done so next state is -1
      break;  // sample time read finished



      // s=400-403 means SAMPLE TIME WRITE
      case 400:
      /* get 10000's digit */
      if (val>47 && val <58) {
        digit=val-48;
newT = digit*10000;
        s = 401;  // get 1000's digit from serial
      }
      else {
        s=-1;  // if value is not a sign then return to -1
      }
      break;  // s=400 taken care of
      case 401:
      /* get 1000's digit */
```

```
      if (val>47 && val <58) {
        digit=val-48;
newT = digit*1000;
        s = 402;  // get 100’s digit from serial
      }
      else {
        s=-1;  // if value is not a sign then return to -1
      }
      break;  // s=401 taken care of
      case 402:
      /* get 100’s digit */
      if (val>47 && val <58) {
        digit=val-48;
newT += digit*100;
        s = 403;  // get 10’s digit from serial
      }
      else {
        s=-1;  // if value is not a number then return to -1
      }
      break;  // s=402 taken care of
      case 403:
      /* get 10’s digit */
      if (val>47 && val <58) {
        digit=val-48;
newT += digit*10;
        s = 404;  // get 1’s digit from serial
      }
      else {
        s=-1;  // if value is not a number then return to -1
      }
      break;  // s=403 taken care of
      case 404:
      /* get 1’s digit */
      if (val>47 && val <58) {
        digit=val-48;
newT += digit;
        sampleT = newT;
        tempPID.SetSampleTime(sampleT);  // set new sampling time
        s = -1;  // we are done so next state is -1
      }
      else {
        s=-1;  // if value is not a number then return to -1
```

```
}
break;  // sample time write finished



// s=410 means PID OUTPUT READ
case 410:
if (val==57) {
  Serial.println(floor(Output));
}
s=-1;  // we are done so next state is -1
break;  // PID output read finished



// s=420 means 24bit ADC READ
case 420:
/* the second received value indicates ADC number  */
switch (val) {
  case 49:
  digitalWrite(slaveSelectPin, HIGH); // make sure SS is high
  digitalWrite(slaveSelectT2, HIGH); // turn off second ADC
  digitalWrite(slaveSelectT1, LOW); // select the first ADC
  delayMicroseconds(1);

  while (digitalRead(MISOpin) == HIGH) {
    //if data is not ready, turn device off and wait
    digitalWrite(slaveSelectT1, HIGH); // turn the device off
    delay(100); // wait
    digitalWrite(slaveSelectT1, LOW); // turn device back on
  }

  // reset input parameters
  ADCval=0;
  sig=0;

  b0 = SPI_read(); // read 4 bytes adc raw data with SPI
  if ((b0 & 0x20) ==0) sig=1;  // is input negative?
  b0 &=0x1F; // discard bit 25..31
  ADCval |= b0;
  ADCval <<= 8;
  b0 = SPI_read();
```

```
        ADCval |= b0;
        ADCval <<= 8;
        b0 = SPI_read();
        ADCval |= b0;
        ADCval <<= 8;
        b0 = SPI_read();
        ADCval |= b0;

        delayMicroseconds(1);

        digitalWrite(slaveSelectT1, HIGH); // turn the device off
        delay(100);

        if (sig) ADCval |= 0xf0000000; // if neg, insert sign bit
        ADCval=ADCval/16; //scale result down , last 4 bits empty
Serial.println(ADCval);       /* send value via serial  */
        break;

        case 50:
        digitalWrite(slaveSelectPin, HIGH); // make sure SS is high
        digitalWrite(slaveSelectT1, HIGH); // turn off first ADC
        digitalWrite(slaveSelectT2, LOW); // select the second ADC
        delayMicroseconds(1);

        while (digitalRead(MISOpin) == HIGH) {
          //if data is not ready, turn device off and wait
          digitalWrite(slaveSelectT2, HIGH); // turn the device off
          delay(100);
          digitalWrite(slaveSelectT2, LOW); // turn device back on
        }

        // reset the input parameters
        ADCval=0;
        sig=0;

        b0 = SPI_read(); // read 4 bytes adc raw data with SPI
        if ((b0 & 0x20) ==0) sig=1;  // is input negative ?
        b0 &=0x1F; // discard bit 25..31
        ADCval |= b0;
        ADCval <<= 8;
        b0 = SPI_read();
        ADCval |= b0;
```

```
        ADCval <<= 8;
        b0 = SPI_read();
        ADCval |= b0;
        ADCval <<= 8;
        b0 = SPI_read();
        ADCval |= b0;

        delayMicroseconds(1);

        digitalWrite(slaveSelectT2, HIGH); // turn device off
        delay(100);

        if (sig) ADCval |= 0xf0000000; // if neg, insert sign bit
        ADCval=ADCval/16; // scale result down, last 4 bits empty
Serial.println(ADCval);       /* send value via serial  */
        break;

        default:  /* unrecognized, no action  */
        break;
      }
      s=-1;  /* routine is done, so return to val -1 */
      break; /* s=420 taken care of          */



      // s=430 means PID TEMPERATURE INPUT READ
      case 430:
      if (val==57) {
        Serial.println(Input);
      }
      s=-1;  // we are done so next state is -1
      break;  // PID temperature input read finished

    }  // end switch on state s statement
  } // end if serial available statement


  //read in temp, compute control, output temp reading
  digitalWrite(Vrefon,HIGH);  //turn on reference voltage
  discreteVoltage = ADCread();
  digitalWrite(Vrefon,LOW);  //turn off reference voltage
  Vratio = discreteVoltage/16777215;  //convert ADC to (V1/Vcc)
```

```
  R = R2*((1-Vratio)/Vratio);  //convert V to R
  Input = tempConvert(R,a,b,c);  //convert R to T
  tempPID.Compute();  //call PID control
  // limit PID output to avoid overdriving Peltier
  if (Output > 245) {
    Output = 245;
  }

  analogWrite(peltierPin,Output);  //output ranges from 0 to 255

}  // end loop statement







/*********** Begin support functions ***********/


/***********/
// convert resistance to temperature
double tempConvert(double R, double a, double b, double c) {
  return (1/(a+b*log(R)+c*pow(log(R),3)))-273.15;
}


/***********/
// read from the LTC2400 ADC
long int ADCread() {
  /* initialize variables */
  long int  ADCval = 0;  // placeholder for ADC return
  byte b0;
  byte sig;  // sign bit flag

  digitalWrite(slaveSelectPin, HIGH); // make sure SS is high
  digitalWrite(slaveSelectT2, HIGH); // turn off second ADC
  digitalWrite(slaveSelectT1, LOW); // select the first ADC
  delayMicroseconds(1);

  while (digitalRead(MISOpin) == HIGH) {
```

```
    //if data is not ready, turn device off and wait
    digitalWrite(slaveSelectT1, HIGH); // turn the device off
    delay(100);
    digitalWrite(slaveSelectT1, LOW); // turn it back on
  }

  // reset the input parameters
  ADCval=0;
  sig=0;

  b0 = SPI_read(); // read 4 bytes adc raw data with SPI
  if ((b0 & 0x20) ==0) sig=1;  // is input negative ?
  b0 &=0x1F; // discard bit 25..31
  ADCval |= b0;
  ADCval <<= 8;
  b0 = SPI_read();
  ADCval |= b0;
  ADCval <<= 8;
  b0 = SPI_read();
  ADCval |= b0;
  ADCval <<= 8;
  b0 = SPI_read();
  ADCval |= b0;

  delayMicroseconds(1);

  digitalWrite(slaveSelectT1, HIGH); // done reading, turn device off
  delay(100);

  if (sig) ADCval |= 0xf0000000; // if negative insert sign bit
  ADCval=ADCval/16; // scale result down , last 4 bits empty
  return ADCval;
}


/***********/
/* SPI data reading function from
http://interface.khm.de/index.php/lab/experiments/connect-a-
ltc2400-high-precision-24-bit-analog-to-digital-converter/
*/
byte SPI_read() {
 SPDR = 0;
```

```
  while (!(SPSR & (1 << SPIF))) ; /* Wait for SPI shift out done */
  return SPDR;
}
```